Cell-related influences on the degradation of magnesium-based materials for neural applications

Dissertation

zur Erlangung des akademischen Grades

Doktor der Ingenieurwissenschaften

(Dr.-Ing.)

der Technischen Fakultät

der Christian-Albrechts-Universität zu Kiel

vorgelegt von

Reneé Unbehau

Kiel 2020

Erstgutachterin:	Prof. Dr. Regine Willumeit-Römer
Zweitgutachterin:	Prof. Dr. Christine Selhuber-Unkel
Tag der mündlichen Prüfung:	12.03.2021

Eidesstattliche Erklärung

Hiermit erkläre ich, dass die beigefügte Dissertation, abgesehen von der Beratung durch die Betreuer, nach Inhalt und Form meine eigene Arbeit ist.

Die Arbeit, ganz oder zum Teil, wurde nie schon einer anderen Stelle im Rahmen eines Prüfungsverfahrens vorgelegt und ist, abgesehen von den im Anhang angegebenen Veröffentlichungen, nicht anderweitig zur Veröffentlichung vorgelegt worden.

Außerdem ist die Arbeit unter Einhaltung der Regeln guter wissenschaftlicher Praxis der Deutschen Forschungsgemeinschaft entstanden.

Geesthacht, den 14.12.2020

Table of contents

Abstract

The use of magnesium (Mg)-based materials for medical devices has been promoted over the past years, owing to their excellent biocompatibility and degradability under physiological conditions. Apart from the widely discussed applications in orthopedics, Mg and its alloys are also promising materials to be applied in local strategies for the treatment of severe neurological disorders. Considering the functional importance and sensitivity of the human brain, the evaluation of Mg-based materials for neural applications requires careful *in vitro* assessment. Such an analysis includes cytocompatibility tests, as well as the elucidation of cell-induced degradation mechanisms to predict the *in vivo* material performance.

In the present thesis, the impact of different neural cell types (tumor cells, astrocytes and microglial cells) and densities on the degradation of Mg discs and magnetron sputtered Mg-based thin films was investigated in a direct contact *in vitro* model (i.e., cells directly cultured onto the material surface). In the first part of the thesis, the specific cell-induced degradation mechanisms were analyzed for the cell contact on pure Mg discs. The cell impact on Mg degradation was quantified using immersion tests for weight loss measurement, scanning electron microscopy (SEM) and infrared (IR) spectroscopy methods. Cell distribution, cell metabolic activity, extracellular matrix (ECM) composition and distribution, and the chemical interaction of selected ECM molecules with Mg were investigated to shed light on the underlying cell-related degradation mechanisms. The degradation analysis revealed cell type- as well as cell-density dependent degradation behavior. Degradation inhibition was observed for none-proliferating neural cells and was related to the presence of a passivating layer of cells and ECM and to the formation of stable carbonate-rich degradation layers. Cell metabolic activity, and as a consequence thereof the local pH decrease, was identified to play a crucial role in degradation promotion. Moreover, the ECM glycosaminoglycan (GAG) compounds chondroitin sulfate (CS) and hyaluronic acid (HA) were shown to affect degradation by the complexation of either Mg^{2+} or Ca^{2+} and PO_4^{3-}. Finally, the results obtained in this thesis indicated a cell-induced time dependence of the degradation outcome for Mg materials in contact with neural cells. In the second part of the thesis, Mg-based thin films were analyzed regarding their stability under *in vitro* testing conditions and hence suitability for neural applications. Thin film stability was assessed in immersion tests. A preliminary thin film cytotoxicity analysis was conducted employing a cell viability and cytoskeleton staining in contact with Mg-6Ag thin films with different degradation rates. Pure Mg as well as Mg-6Ag thin films proved to be sufficiently stable under *in vitro* conditions for a time span of four days and therefore qualified for further in-depth *in vitro* analysis. The preliminary cytotoxicity screening showed that degradation rate tailoring of Mg-based thin films may be a promising tool for customized approaches to the treatment of different neurological disorders.

Zusammenfassung

Aufgrund ihrer Biokompatibilität und Degradierbarkeit unter physiologischen Bedingungen wurde die Verwendung von Magnesium (Mg) und seinen Legierungen für medizinische Anwendungen in den letzten Jahren weiter vorangetrieben. Neben orthopädischen Anwendungen, zeigen Mg-basierte Materialien großes Potential für den Einsatz in lokalen Therapien schwerer neurologischer Erkrankungen. Die zentrale Funktion des menschlichen Gehirns erfordert eine besonders sorgfältige *in vitro* Beurteilung solcher Materialien, die sowohl Zytokompatibilitätstests als auch eine detaillierte Analyse zellbedingter Degradationsmechanismen umfassen muss, um das *in vivo* Materialverhalten vorherzusagen. In der vorliegenden Arbeit wurde der Einfluss verschiedener neuraler Zelltypen (Tumorzellen, Astrozyten und Mikroglia) und -dichten auf die Degradation von Mg-Discs und Magnetron gesputterten Mg-Dünnfilmen im direkten Material-Zell-Kontakt in einem *in vitro* Model untersucht. Zunächst wurden die spezifischen zellbedingten Degradationsmechanismen im Kontakt mit reinen Mg-Discs analysiert. Der Zelleinfluss wurde mittels Immersionstests, Rasterelektronenmikroskopie und Infrarotspektroskopie quantifiziert. Die Untersuchungen der Zellverteilung, der metabolischen Aktivität, der Zusammensetzung und Verteilung der extrazellulären Matrix (EZM) sowie der chemischen Interaktion ausgewählter EZM Moleküle mit Mg wurden herangezogen, um die zugrundeliegenden Degradationsmechanismen aufzuklären. Die Degradationsanalyse zeigte zelltyp- und zelldichteabhängiges Degradationsverhalten. Degradationshemmung wurde für nichtproliferierende Zellen beobachtet und war durch das Vorkommen einer passivierenden Lage aus Zellen und EZM sowie durch die Ausbildung einer stabilen, sauerstoff- und kohlenstoffreichen Degradationsschicht bedingt. Der metabolischen Aktivität und der dadurch bedingten lokalen pH-Absenkung konnte eine wichtige degradationsfördernde Rolle zugeschrieben werden. Darüber hinaus konnte gezeigt werden, dass die EZM-Glykosaminoglykane Chondroitinsulfat und Hyaluronsäure die Degradation durch die Komplexierung von Mg^{2+}, Ca^{2+} und PO_4^{3-} beeinflussen. Abschließend deuteten die Ergebnisse auf eine zellinduzierte Zeitabhängigkeit der Degradation hin. Im zweiten Teil der Arbeit wurden Mg-Dünnfilme hinsichtlich ihrer Stabilität unter *in vitro* Bedingungen in Immersionsversuchen und hinsichtlich ihrer Eignung für neurale Anwendungen getestet. Vorläufige Zytotoxizitätsuntersuchungen wurden mittels Viabilitäts- und Zytoskelettfärbungen im Kontakt mit unterschiedlich stark degradierenden Mg-6Ag Filmen durchgeführt. Sowohl reine Mg- als auch Mg-6Ag-Dünnfilme waren über einen Zeitraum von vier Tagen ausreichend stabil und bestätigten damit ihre Eignung für weitere Analysen. Vorläufige Zytotoxizitätsanalysen zeigten, dass ein gezieltes Einstellen der Degradationsraten von Mg-Dünnfilmen anwendungsspezifische Lösungen für die Behandlung verschiedener neurologischer Erkrankungen schaffen könnte.

1 Introduction

1.1 Mg-based materials for biomedical applications

1.1.1 State of the art

The use of Mg-based materials in different biomedical applications has attracted increasing attention, owing to their excellent biocompatibility and degradability. One reason for the high biocompatibility of Mg relates to the fact that Mg is an essential element in the human organism, participating in a considerable number of physiologically relevant processes [1]. The Mg content in an adult human body is ca. 24 g [2] and is normally obtained by dietary intake. Excess Mg (e.g., obtained from degrading Mg-based implant materials) is promptly filtered via the kidneys [3]. Thus, hypermagnesemia is rare and temporarily elevated Mg serum levels are prevailingly uncritical in healthy humans with normal renal functions [4]. The degradability of Mg even in physiological media is related to its low standard potential of -2.37 V and its limited ability to form stable, passivating oxide layers (Pilling–Bedworth ratio 0.81) [5, 6]. This biodegradability facilitates the temporary use of Mg-based implants in orthopedic [7, 8] and cardiovascular [9] applications.

In terms of orthopedic applications, the biodegradability is favorable as it enables tissue regrowth unlike permanent implant materials (e.g., titanium and stainless steel). Furthermore, Mg exhibits favorable mechanical properties which are closer to the mechanical properties of bone than those of conventionally used bone implant materials such as titanium and stainless steel [10]. As a consequence thereof, Mg-based implant materials can reduce the risk of stress shielding and subsequent premature implant loosening evoked by the mismatch of the mechanical properties of bone and implant [11]. Additionally, Mg can be considered to be somewhat bioactive (e.g., osteopromotive) in this particular application [12]. For cardiovascular applications, biodegradability is advantageous as it can diminish the likelihood of platelet aggregation and late stent thrombosis at times observed for permanent stents [13]. Moreover, the full degradability of Mg-based stents allows to perform subsequent stenting or a second surgical intervention at the same implantation site if needed [14].

In fact, the concept of using Mg in biomedical applications is not new and dates back to as early as 1878, when E. Huse reported the use of Mg wires as ligature materials [15]. Although Mg-based materials were continued to be suggested and tested for a number of biomedical applications in subsequent years, a limited understanding of Mg degradation as well as technical constraints (e.g., difficulty to produce high purity Mg) impeded their successful use in medicine [4]. Since then significant advances have been made in Mg degradation research eventually leading to the approval for clinical use and commercial availability of several Mg-

based implants over the past years. This includes a number of Mg-based bone screws and pins, Mg-based stents and Mg clips [16].

Apart from the aforementioned applications, Mg-based nanoparticles and flakes have been suggested to be used as a base material for drug delivery applications in a number of studies recently [17-20]. As Mg degradation is highly pH-dependent [21, 22], the material qualifies for targeted drug release especially in organs and tissues with low pH (e.g., stomach and tumor environment) [17]. Moreover, this highlights the great diversity and high potential of Mg for future alternative applications.

1.1.2 Mg in neural applications

Recently, Mg-based materials have also been suggested for the use in neural applications [23-27]. Zhang et al. [28], for instance, proposed the application of Mg-based wires as a scaffold material to ensure mechanical integrity in temporary electrodes for neural recordings. Since Mg is involved in multiple cellular processes within the central nervous system (CNS), and Mg^{2+} homeostasis imbalance is associated with a wide range of neurological disorders [1-3], Mg-based materials might also be potential candidates to serve specific biological functions within the brain.

Physiologically, Mg is among the two most abundant intracellular cations in the human body and takes part in a large number of cellular processes, such as cell proliferation, deoxyribonucleic acid (DNA) stabilization, enzymatic reactions and protein synthesis [1, 2]. The majority of the body Mg is stored in bone, which serves as a reservoir to compensate temporary changes in serum Mg levels [4]. Generally, Mg is absorbed in the intestine after dietary intake [3]. From there it is distributed to other tissues and organs including the brain via the blood [29]. Due to the functional importance of the brain and to prevent uncontrolled diffusion of pathogens and large molecules, such as nutrients, from the blood into the extracellular fluid (ECF) of the brain, the transport of solutes is highly regulated [30]. Entry sites of Mg (Figure 1) to the brain are therefore either the blood-brain barrier (BBB) or the *choroid plexus* (essentially the blood-cerebrospinal fluid barrier (BCSFB)), i.e., a network of small vessels within the ventricles [29]. Interestingly, Mg^{2+} contents in cerebrospinal fluid (CSF) and ECF are higher than the Mg^{2+} content in blood, suggesting that there is a directed and active transport of Mg from the blood into these compartments [29]. Furthermore, this gradient in Mg^{2+} concentration underlines the importance of Mg in fundamental neurological processes [31].

In addition to its central role in numerous cellular processes mentioned above, Mg is involved in neurotransmission within the brain and plays a major role in synaptic connectivity and

plasticity [32]. One essential function of Mg in neural tissue is the interaction with the *N*-methyl-D-aspartate (NMDA) receptor [29]. The NMDA receptor is a subtype of ionotropic glutamate receptors which is involved in synaptic signaling [33]. Physiologically, Mg is responsible for blocking the calcium ion (Ca^{2+}) channel of the NMDA receptor to prevent exitotoxicity [34]. Exitotoxicity describes the excess influx of Ca^{2+} into neurons which results in the degradation of vital cellular compounds due to enzyme activation and essentially leads to neuronal death [35]. The dysfunction of the NMDA receptor in combination with low levels of Mg has been associated with a wide range of neurological disorders including migraine, chronic pain, Alzheimer's disease (AD), Parkinson's disease, stroke, and epilepsy [29, 34].

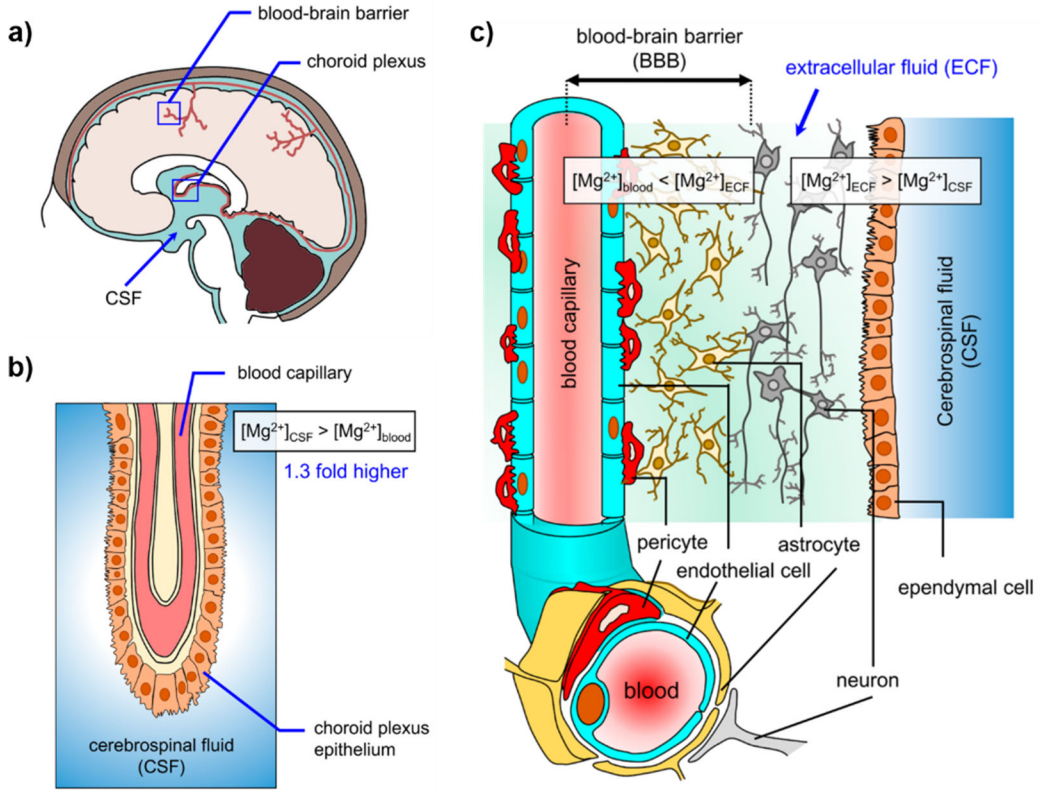

Figure 1 | Mg homeostasis in the human brain. a) Location of the Mg entry sites (BBB, *choroid plexus*) in the human brain. **b)** Schematic structure of the BCSFB in the *choroid plexus* and Mg^{2+} concentration gradient between blood and CSF. **c)** Schematic structure of the BBB and Mg^{2+} concentration gradient between blood and ECF, as well as between ECF and CSF. Adapted with permission from [29].

Hence, the administration of Mg may be a potential therapeutic approach to the treatment of these brain-related disorders. In fact, first promising results have been reported for the use of Mg in traumatic brain injury and AD in rat and mouse models [36, 37]. Nevertheless, the systemic administration of Mg still faces the challenge of Mg passing through the BBB in required doses, as observed in a number of studies [38, 39].

The BBB imposes not only a challenge on novel systemic Mg therapy approaches in the aforementioned pathologies, but also hampers the systemic drug administration in other severe brain-related diseases, such as *glioblastoma multiforme* (GBM) [40]. For the therapy of these neurological disorders, local treatment strategies might therefore be of particular interest. Although local treatment requires surgical intervention, it could increase therapy success and reduce side effects of systemic treatment, especially in GBM [41]. Mg-based materials hold a great potential for the use in local therapy of the aforementioned neurological disorders. Owing to its degradability in physiological environments, Mg-based materials are a source for a constant and controllable release of Mg^{2+}. Moreover, Mg degradation is accompanied by surface-near effects such as hydrogen gas (H_2) release, the elevation of surface pH, or the additional release of therapeutically active alloying element ions (e.g., silver (Ag) or lithium (Li)) [42, 43]. These effects may be particularly relevant in cancer therapy [44-46]. In addition to that, Mg-based materials could be coated with drug eluting hydrogels or polymers (Figure 2).

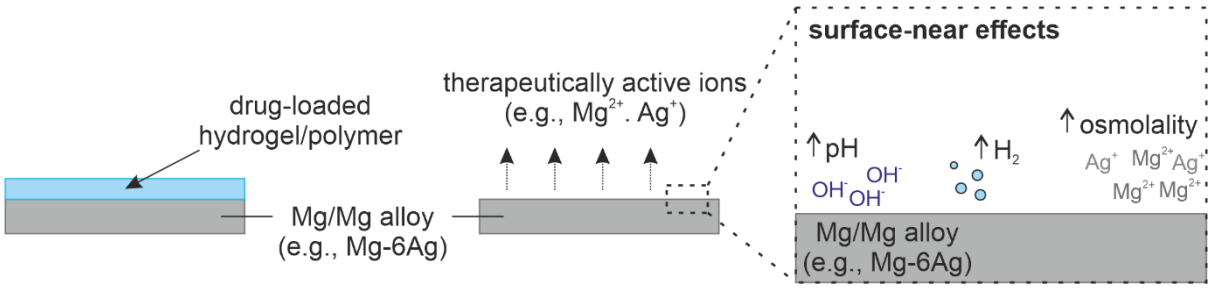

Figure 2 | **Mg-based neural implant design.** Mg-based materials (e.g., Mg-6Ag) could serve as a scaffold material for the coating with drug-loaded hydrogels/polymers. Additionally, bare Mg-based materials can release therapeutically active ions during degradation and degradation-induced surface-near effects (pH increase, H_2 evolution, osmolality increase) can be exploited for disorder treatment.

Not only would such a coating contribute to an enhanced treatment efficacy, but it would also be a measure to control Mg degradation [47, 48]. Rapid degradation of Mg-based implants remains a major challenge in biomedical applications [11, 49]. Single-phase Mg materials with superior degradation resistance for the use as neural implants can be obtained by thin film fabrication via UV lithography and magnetron sputtering [50]. Besides, this material processing route facilitates the fabrication of miniaturized, customized and clinically relevant implant geometries. In light of the sensitivity and functional importance of neural tissue, it is pivotal to reliably predict and control the Mg degradation rate. For this purpose, an in-depth understanding of the underlying cell-material interactions, including the material impact on the

cells as well as the impact of the biological system on the material degradation, is crucial. Accordingly, adequate *in vitro* models are required to anticipate *in vivo* material performance.

1.2 Mg degradation under physiological conditions

It is a well-accepted fact that Mg degradation is influenced by the material properties itself, including composition (alloy and impurities) and microstructure [51]. Apart from this, the specific constitution of the degradation environment has a major influence on Mg degradation. Thus, Mg corrosion under atmospheric conditions in technical applications largely differs from Mg degradation under physiological conditions in biomedical applications. Over the last years, substantial advances have been made in analyzing the degradation processes and mechanisms involved in Mg degradation under physiological conditions to understand, predict, and improve the degradation performance of Mg-based implants in clinical applications. Nevertheless, there is still a significant discrepancy between *in vitro* and *in vivo* degradation results [52]. The influence of physiological salt solutions, such as Hank's balanced salt solution (HBSS) or simulated body fluids (SBF), and more complex cell culture media (CCM) on Mg degradation is more and more understood [53-56]. Yet, the influence of single factors in environments with increasing complexity, i.e., CCM with serum supplementation (*e.g.*, containing proteins and hormones), *in vitro* environments (CCM with serum supplementation and cells) and finally *in vivo* environments, still remains somewhat ambiguous.

Upon exposure to air, Mg is rapidly oxidized leading to the formation of a thin Mg oxide (MgO) layer on top of the bulk material [51]. Generally, Mg undergoes surface hydroxylation in aqueous solutions, which causes the formation of a Mg hydroxide ($Mg(OH)_2$) layer and the evolution of H_2 as shown in equations 1-3.

anodic reaction: $$Mg \rightarrow Mg^{2+} + 2e^- \quad (1)$$

cathodic reaction: $$2H_2O + 2e^- \rightarrow 2H_2 + 2OH^- \quad (2)$$

$$Mg + 2H_2O \rightarrow Mg(OH)_2 + 2H_2 \quad (3)$$

The $Mg(OH)_2$ layer is thermodynamically stable under alkaline conditions (pH>8.5) only [57]. Thus, $Mg(OH)_2$ initially dissolves during further contact with water. The dissolution of $Mg(OH)_2$ leads to an increase in pH, which in turn facilitates the formation of a stable $Mg(OH)_2$ layer [51]. In complex biological degradation environments, inorganic salts, organic molecules, temperature, oxygen (O_2), carbon dioxide (CO_2), degradation medium flow, as well as living organisms (cells or tissue) additionally influence Mg degradation. Some of these factors are described in more detail below.

Inorganic ions

Chlorine ions (Cl^-), hydrogen carbonate ions (HCO_3^-), Ca^{2+}, and phosphate ions (PO_4^{3-}) are abundantly present inorganic ions in physiological environments and are known to affect Mg degradation. Cl^- was reported to react with Mg to form soluble magnesium chlorides ($MgCl_2$) inducing pitting corrosion and hence degradation acceleration [51]. In physiological environments, HCO_3^- is part of the bicarbonate buffering system which also exists naturally in blood and is responsible for maintaining solution pH via the CO_2/HCO_3^- equilibrium (equation 4) [58, 59]. HCO_3^- occurs either due to the reaction of CO_2 with H_2O (equation 4), or due to the addition of sodium bicarbonate in some CCM, as CCMs are CO_2/HCO_3^- equilibrated for a CO_2 content of 5 - 10 %. The presence of HCO_3^- in combination with adequate CO_2 contents was shown to lead to the formation of stable Mg carbonates ($MgCO_3$) and can thereby be a factor for degradation reduction [53].

$$H_2O + CO_2 \leftrightarrow H_2CO_3 \leftrightarrow HCO_3^- + H^+ \quad (4)$$

Ca^{2+}, and PO_4^{3-} were reported to promote the precipitation of magnesium and calcium phosphates phases which are linked to degradation retardation [60]. Moreover, Ahmad Agha et al. [61] previously suggested that the combination of Ca^{2+}, PO_4^{3-} and HCO_3^- can enhance this effect due to the mediating role of carbonates in Ca/P-phase formation. Comparative studies for HBSS and SBF showed that already variations in salt composition in a physiological medium can alter degradation rate and degradation product formation [53], underlining the necessity for a careful evaluation of suitable *in vitro* testing media.

Organic compounds

Relevant organic compounds in physiological media include proteins, amino acids, vitamins, glucose, growth factors, hormones, and immunoglobulins. Under *in vitro* testing conditions, these compounds are either ingredients of a CCM, such as Dulbecco's Modified Eagle Medium (DMEM), part of a serum supplement (e.g., fetal bovine serum (FBS)), or expressed by cells. It is generally acknowledged that organic compounds are majorly involved in the Mg degradation process under physiological conditions [51, 62, 63]. Therefore, the addition of organic molecules to physiological salt solutions is well-recognized to be indispensable to approach *in vivo* conditions. However, the detailed interaction mechanisms of organic molecules and Mg in complex environments are far from being fully understood and require further intensive research.

A growing number of studies was recently dedicated to analyzing the influence of different proteins on Mg degradation, reporting degradation inhibiting as well as degradation promoting effects [64-66]. In addition to that, proteins were observed to alter the degradation product

formation [67]. The effect of single proteins was shown to be highly dependent on the overall medium composition, the protein type and protein concentration [68]. Nevertheless, these studies propose two main mechanisms of protein-Mg interaction, namely adsorption and chelating/binding of ions. The adsorption of proteins has commonly been suggested to be a factor in degradation inhibition [63, 66, 69], while the effect of ion chelation/binding strongly depends on the type of interacting ion. The binding of Mg^{2+}, for instance, has been associated with increased degradation owing to a shift in the chemical equilibrium of the Mg dissolution reaction [66, 69]. In contrast to this, the binding of Ca^{2+} by proteins is discussed to be a major factor of significantly decreased degradation by facilitating the precipitation and nucleation of Ca/P-phases [68]. The importance of Ca^{2+} interaction with other organic molecules was likewise demonstrated by Zeng et al. [70] in their study dealing with the impact of glucose on Mg degradation in Ca^{2+}-containing HBSS and sodium chloride (0.9 % NaCl). The authors suggested that similarly to proteins, glucose can complex Ca^{2+} and thereby induce the formation of Ca/P-phases in HBSS leading a decrease in degradation rate.

Protein adsorption and ion binding by organic molecules in general are influenced by a vast number of factors, including surface properties of the material, surrounding conditions (temperature, pH, protein concentration, salt composition etc.), and the molecule properties (binding affinity for ions, charge, structural conformation etc.) [71], which highlights the immense complexity of the interactions once more. Moreover, Hou et al. [68] compared the impact of protein mixtures and single proteins on Mg degradation, attempting to approach *in vivo* conditions even further. Their findings indicated that single proteins may interact with one another in protein mixtures, which can impact the degradation outcome further. Comparable interactions between other organic molecules, which ultimately influence Mg degradation, are likely to happen in complex biological environments.

Cells

A next step to approach *in vivo* conditions even further, is to analyze the impact of cells in CCM with serum supplementation on Mg degradation to create a complex *in vitro* testing system. Although the influence of cells on Mg degradation received increasing interest over the last years, detailed material-cell interactions remain mostly unknown. Available publications on the cellular influence highlight a high dependence of the degradation outcome on the cell type and the material used [72-78]. As cells are living organisms, they can actively and passively alter a degrading material surface either due to a response to an external stimulus (e.g., inflammatory response) [74], or as a result of normal cellular processes (metabolism, cell growth, proliferation, secretion of extracellular matrix (ECM) etc.) [72, 75-78], or through a combination of both [73]. Moreover, cells can be a factor in time-dependent

degradation development, as similarly observed for the influence of proteins [67]. Since different cell types vary in their function and phenotype, each cell type can create a unique chemical environment of cell-released ions and organic molecules, which can then in turn determine the continuing degradation. Hence, it is of utmost importance to utilize appropriate *in vitro* models based on the material application and implantation site when attempting the prediction of *in vivo* implant performance. Most cell types studied regarding their influence on Mg degradation so far are relevant in orthopedic and cardiovascular applications, which underlines the need of an adequate *in vitro* system for neural applications.

1.3 Factors in brain physiology and pathology influencing Mg degradation

1.3.1 pH regulation

pH regulation is essential in all living organisms to maintain fundamental cellular functions [79]. As a result of cellular respiration cells produce metabolic acids which cause an intracellular pH decrease and impose the need for active pH regulation mechanisms. The physiological intracellular pH varies between 6.8 and 7.2 for most cells, while different cellular compartments and organelles can differ in pH [80]. In terms of Mg material-cell interaction, however, the transport mechanisms of acids and bases through the cellular membrane between intra- and extracellular space are of particular interest, as the degradation of Mg is highly pH-dependent. Two major metabolic products involved in pH regulation are CO_2 and lactate/H^+ [81]. Lactate is a by-product of glycolysis, which is the metabolic process to convert glucose to energy (adenosine triphosphate, ATP) [82]. During this conversion, as well as during the subsequent ATP-hydrolysis, proportional amounts of lactate and H^+ are generated [81]. Lactate/H^+ is extruded from cells via a cotransport mechanism utilizing monocarboxylate transporters (MCT) [83]. CO_2 is generated during the tricarboxylic acid (TCA) cycle and the pentose phosphate pathway, i.e., a metabolic pathway linked to glycolysis [84]. In aqueous solutions (e.g., in the cytosol), CO_2 is hydrated und dissociates in H^+/HCO_3^-. H^+/HCO_3^- is the main pH buffer in cells and ECF and hence plays a vital role in biological pH homeostasis [79, 85]. Directed transport of H^+/HCO_3^- is mediated by HCO_3^--dependent transporters such as Cl^--HCO_3^- exchangers, (Na^++HCO_3^-)-Cl^- exchangers and Na^++HCO_3^- co-transporters [80]. However, the process of CO_2 hydration is relatively slow (time constant ca. 5-20 s, pK_a=6.1), wherefore a part of the generated CO_2 diffuses through the cell membrane into the extracellular space [81]. There, carbonic anhydrases (CAs) can catalyze the reversible hydration of CO_2 [86]. Besides the mentioned mechanisms, pH regulation is obtained by multiple other transport mechanisms, including H^+ pumps and cation-H^+ exchangers [79, 80, 85].

In cancer (e.g., GBM), cellular respiration is significantly altered known as the Warburg effect [87], which essentially leads to a high metabolic acid load in cancer cells. To circumvent apoptosis, resulting from inadequate intracellular pH levels, the expression of some pH-regulating transporters (e.g., HCO_3^--dependent transporters and MCTs) is increased in cancer cells to bear with the acid load [88]. Moreover, the expression of transmembrane CAs (e.g., carbonic anhydrase IX or CAIX), has been reported to be upregulated in cancer cells, contributing to the severe extracellular acidification observed in the tumor microenvironment [89]. This acidification can be a major impact factor for cell-induced degradation of Mg-based materials.

pH regulation is not a one-way process during which molecules and ions are only extruded from cells. Instead, the extracellular pH can actively influence the intracellular pH via directed transport of compounds into cells [81]. These processes need to be considered, especially when using Mg-based materials, as these materials alter pH during degradation. A material-determined pH change may be a potential treatment target in disorders associated with impaired pH mechanisms (e.g., in GBM) [90], but might also pose a risk of adverse effects in healthy neural cells, as pH is crucially involved in neuronal signaling processes [79, 85]. That is to say, on one hand pH can influence the neuronal activity/signaling, while on the other hand pH also changes as a consequence of neuronal activity.

1.3.2 Extracellular matrix composition

The ECM is a network composed of proteins, proteoglycans (PGs) and glycosaminoglycans (GAGs) which are synthesized by cells and fill the space between cells [91]. Alongside its role in structural support, the ECM plays a vital role in cell adhesion, cell migration, cell proliferation and cell-cell communication [92]. The detailed ECM composition is highly dependent on individual cell types and is adapted to meet tissue-specific requirements. Unlike the ECM of connective tissues, healthy brain ECM is comparably low in fibrous protein content [93], representing a unique biological environment in the human body. Only minor amounts of adhesion proteins, such as fibronectin and laminin, as well as collagen type IV are found in brain [94]. Instead, physiological neural ECM is rich in PGs, mainly chondroitin sulfate PGs (CSPGs) and lesser amounts of heparan sulfate PGs (HSPGs) including brevican, neurocan aggrecan and versican to name some brain-related PGs [95]. Moreover, brain ECM comprises large amounts of hyaluronic acid (HA), the only GAG that occurs unbound to a core protein. Another compound of healthy brain ECM are tenascins, primarily tenascin-R, which belong to the glycoproteins. In the CNS, the ECM can be divided in three major compartments as shown in Figure 3.

Neuropathologies, such as GBM, are associated with a drastic change in ECM composition [96]. In brain tumor ECM, for instance, the expression of laminin, fibronectin, collagen type IV, HA, and tenascin-C is upregulated, which contributes to the formation of a denser and stiffer matrix [97, 98] that aids tumor cell migration and invasion [99].

In pathologies, as well as in physiology, the ECM undergoes enzyme-driven remodeling [100]. However, the extent of matrix turnover differs largely in both conditions (especially in the CNS) and increased remodeling activity is often linked to abnormal alterations [101]. Important regulators in matrix remodeling are matrix metalloproteinases (MMPs) and A disintegrin and metalloproteinases (ADAMs) [102]. The upregulation of MMP2, -9, -12 and ADAM-10 has been identified to play a critical role in neurological disorders, such as neuroinflammation, GBM and stroke [103, 104].

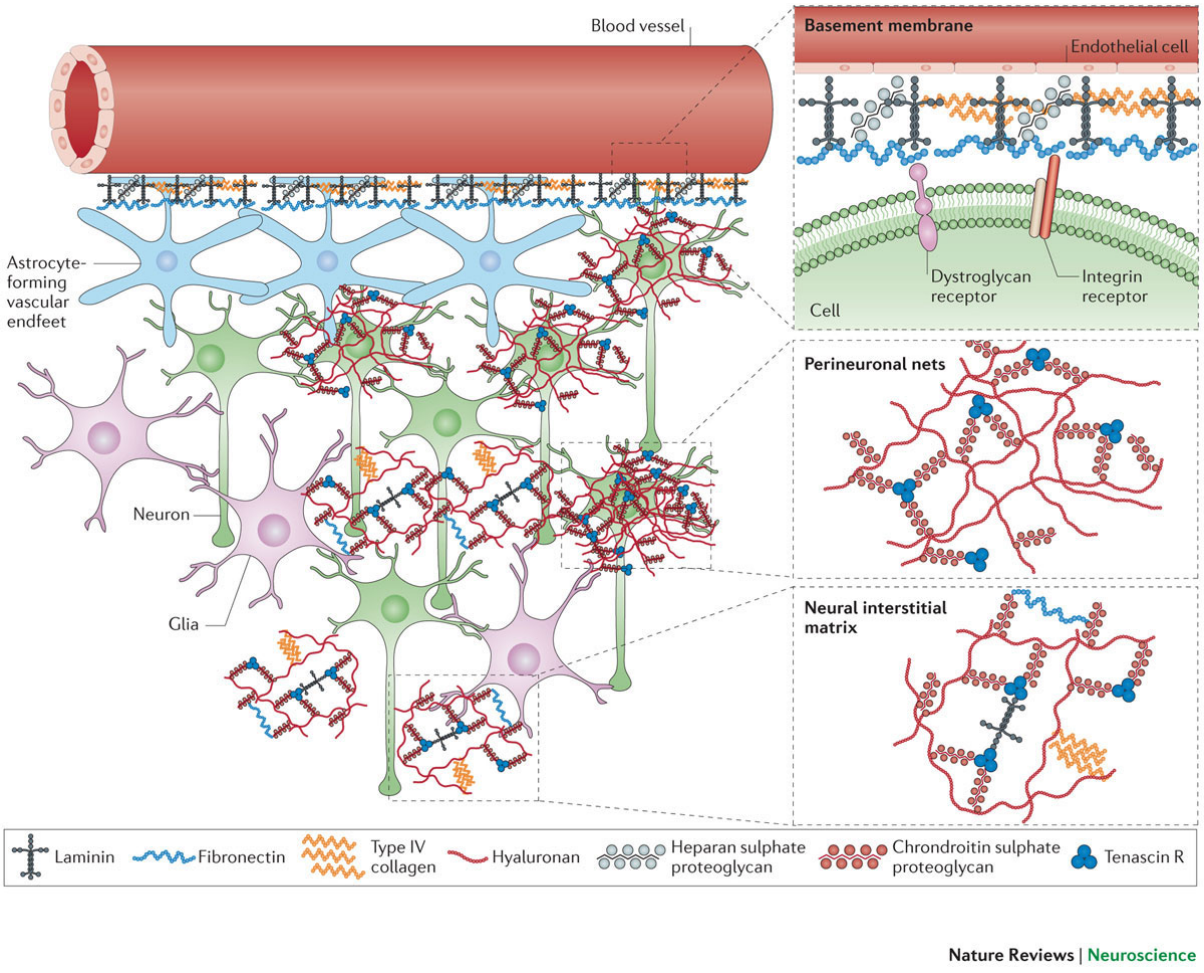

Figure 3 | Schematic illustration of the brain ECM. The brain ECM divides into three compartments: the basement membrane in the proximity of blood vessels, perineuronal nets (i.e., condensed ECM area around cell bodies) and the neural interstitial matrix occupying the space between cells [95] (reproduced with permission from Springer Nature).

As ECM is actively secreted by neural cells, Mg-based neural implants will be in contact with the ECM molecules. Given that Mg materials and ECM molecules chemically interact molecule-dependently, cell type-dependent Mg degradation can be expected. Moreover, ECM remodeling might prompt a certain time dependence of ECM-Mg interactions, which in turn may impact Mg degradation in a time-dependent manner. Thus, ECM-related factors require attention when analyzing the *in vitro* Mg degradation for neural applications.

2 Motivation and objectives

Mg-based materials hold a great potential as base material for drug delivery systems owing to their degradability and high pH sensitivity. Thus, they are promising materials to be applied in novel local treatment strategies for the therapy of neurological disorders including GBM and epilepsy.

Before neural *in vivo* applications, the suitability and the safety of Mg-based biomaterials have to be evaluated. Initial steps of this process include the confirmation of an appropriate degradation rate and cytocompatibility analysis, to provide direct feedback relevant for the material development. Subsequent material evaluation then needs to address detailed cell-material interactions for *in vivo* implant behavior prediction.

Therefore, this thesis investigates the influence of selected neural cells on the degradation of Mg-based materials and aims to elucidate the underlying degradation mechanisms. The thesis thereby focuses on the following objectives:

(1) Investigate the impact of different brain cells and cell densities on Mg degradation rate, degradation layer thickness, and degradation layer composition (direct culture on Mg discs).
(2) Identify if and how the effects observed in (1) relate to cell metabolism and local pH alteration.
(3) Determine the role of brain ECM distribution and composition in Mg disc degradation.
(4) Perform preliminary degradation analysis on pure Mg and Mg-6Ag thin films (in collaboration with Lea Jessen (CAU Kiel) in the frame of the Graduate School “Materials4Brain” (GRK2154)) with and without cells to identify the suitability of thin films for further *in vitro* and *in vivo* testing.

3 Materials and methods

3.1 Mg materials

In this thesis, pure Mg discs, as well as pure Mg and Mg-6Ag thin films were used to study material-cell interactions focusing on different objectives. For the in-depth investigation of cell-induced degradation mechanisms, pure Mg discs were used to ensure (i) a physiologically suitable and constant (reproducibility between single samples) degradation rate for *in vitro* analysis, (ii) material stability over a minimum period of seven days, and (iii) to avoid the impact of alloying elements on cell-material interactions. Mg-based thin films represent materials exhibiting clinically relevant implant geometries. Owing to their miniaturized geometries and fabrication route via UV lithography and magnetron sputtering (as described below), a sufficient stability and availability of Mg-based thin films for long-term *in vitro* analysis could not be guaranteed. Hence, this type of material was only tested in preliminary *in vitro* tests to identify their suitability for further analysis. Pure Mg thin films were studied for a direct comparison with the degradation of pure Mg discs, while Mg-6Ag thin films were examined to approach clinically relevant alloy systems. Table 1 lists the detailed experiments performed with each type of material.

Table 1 | Overview of analyses performed for each type of material.

Method	Mg discs	Mg thin films	Mg-6Ag thin films
***In vitro* degradation**	+	+	+
Degradation product analysis	+	-	-
Biological material evaluation			
Cell viability staining	+	+	+
Cell morphology staining	+	-	+
DNA content	+	-	-
Cell metabolism analysis	+	-	-
ECM analysis	+	-	-
Interaction analysis of ECM and Mg	+	-	-

The Mg-based materials were fabricated as follows:

Mg discs

Pure Mg discs were used for degradation mechanism studies and were fabricated at Helmholtz-Zentrum Geesthacht (Helmholtz-Zentrum Geesthacht, Geesthacht, Germany) via casting, extrusion and cutting. High purity Mg (HP, 99.98 %, MAGNOTEC GmbH, Bottrop, Deutschland) was processed by permanent mold gravity casting (K10/S; Nabertherm GmbH, Lilienthal, Germany). The cast ingots were T4 heat treated and subsequently extruded in rods of 10 mm diameter at an extrusion ratio of 1:25, at a temperature of 350 °C, and with a ram

speed of 2.4 mm/s. The extruded rods were machined into discs with a diameter of 9 mm and a height of 1.5 mm (Henschel KG, Munich, Germany). The chemical composition of the Mg disc batches used in this study was analyzed via optical emission spectrometry (EmiCon; PLASUS GmbH, Mering, Germany) and is shown in Table 2.

Table 2 | Chemical composition of pure Mg discs.

Element	Mg	Fe	Cu	Ni	Al	Be
Wt.%	99.93	0.001-0.005	0.0002-0.0003	<0.0002	0.017-0.027	0.00004-0.00005

Mg thin films

Freestanding pure Mg and Mg-6Ag thin films for preliminary *in vitro* testing were provided by Lea Jessen (GRK2154-P1a, CAU Kiel) and were fabricated by UV lithography and magnetron sputtering.

Sputtering is a material fabrication process which belongs to the category of physical vapor deposition techniques. The bombardment of a target material with energetic particles is used to eject atoms from the target, which then condense on top of a substrate (e.g., silicon wafer) and form a thin film (Figure 4).

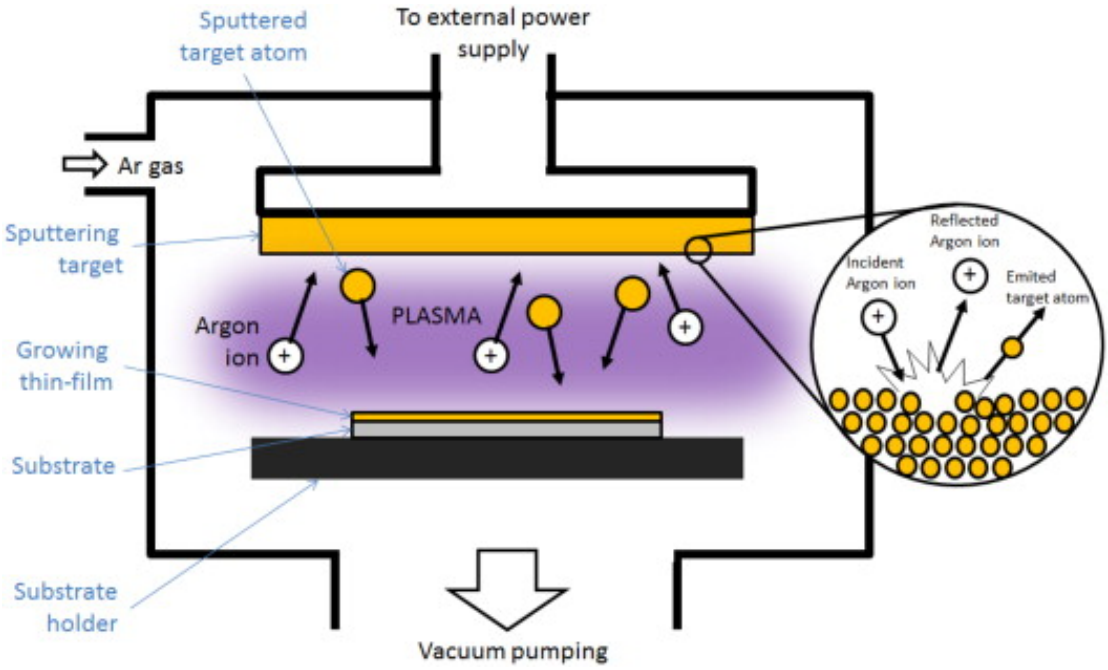

Figure 4 | **Schematic illustration of the sputtering process.** Thin film deposition is achieved by the condensation of atoms emitted from a target material on a substrate due to the target bombardment with energetic particles (e.g., argon ions). Reproduced from [105] with permission from Elsevier.

Unlike other processes/fabrication routes, such as casting, sputtering facilitates the fabrication of some metastable supersaturated (single-phase) materials without the need of a subsequent heat treatment [105]. UV lithography is a method to structure surfaces, commonly used in semiconductor fabrication. A light-sensitive material (photoresist), a photomask and a developer are used to transfer a mask pattern to a substrate (e.g., silicon wafer) in a multi-step process [106]. The combination of UV lithography and magnetron sputtering allows to customize a wide range of different geometries and compositions of thin films.

Silicon wafers were structured by UV lithography using a MA6-8 mask aligner (Süss MicroTec SE, Garching, Germany) and a soda-lime glass mask (ROSE FOTOMASKEN, Bergisch Gladbach, Germany). The structured wafers were then sputtered with aluminum (FHR Anlagenbau GmbH, Ottendorf-Okrilla, Germany) and deep dry etched in a Bosch process (ICP-RIE plasma etcher SI 500, SENTECH Instruments GmbH, Berlin, Germany). Afterwards, a sacrificial layer of aluminum nitride (AlN, FHR Anlagenbau GmbH, Ottendorf-Okrilla, Germany) was deposited on the prepared wafers. Mg and Mg-6Ag sputtering on the prepared wafers was performed using a Von Ardenne CS730S (VON ARDENNE GmbH, Dresden, Germany) cluster magnetron sputtering machine with a power of 200 W for Mg, or 50 W for Mg-6Ag under argon gas flow at 25 sccm and 2.6 x 10^{-3} mbar. Pure Mg and pre-alloyed Mg-6Ag targets for sputtering were purchased from FHR (FHR Anlagenbau GmbH, Ottendorf-Okrilla, Germany). Mg and Mg-6Ag thin films were released from the wafer by the selective etching of the sacrificial AlN layer with 20 % potassium hydroxide (KOH, Carl Roth GmbH + Co. KG, Karlsruhe, Germany). Further details on the fabrication process, as well as an extensive material characterization were recently published by Jessen et al. [50, 107]. Table 3 gives an overview of the dimensions and microstructure of the thin films used in this thesis. The microstructure analysis via x-ray diffraction (XRD) was conducted and kindly provided by Lea Jessen (CAU Kiel) in the frame of the Graduate School “Materials4Brain” (GRK2154).

Table 3 | Material properties of Mg-based thin films.

Batch-ID	19-08/20-**02**		20-01/20-**05**		20-01/20-**05**		20-05/20-**06**		20-05/20-**06**	
Material	Mg-6Ag		Mg-6Ag		Mg		Mg-6Ag		Mg	
Dimensions in cm	1 x 1 x 0.002		1 x 1 x 0.002		1 x 1 x 0.004		1 x 1 x 0.002		1 x 1 x 0.004	
	(hkil)	**2θ (°)**	**(hkil)**	**2θ (°)**	**(hkil)**	**2θ (°)**	**(hkil)**	**2θ (°)**	**(hkil)**	**2θ (°)**
Microstructure (Miller indices and corresponding diffraction angle)	0002	34.4	0002	34.4	0002	34.4	0002	34.4	0002	34.4
	$10\bar{1}1$	36.5	0004	72.5	$10\bar{1}1$	36.6	0004	72.5	$10\bar{1}1$	36.6
	0004	72.6	MgAg	24.9	$10\bar{1}2$	47.8	MgAg	24.9	$10\bar{1}2$	47.8
	MgAg	30.3	MgAg	30.9	$10\bar{1}3$	63.1	MgAg	30.9	$10\bar{1}3$	63.1
	MgAg	37.7	MgAg	33.2	0004	72.5	MgAg	37.8	0004	72.5
	MgAg	80.5	MgAg	37.9	$10\bar{1}4$	81.5	MgAg	65.5	$10\bar{1}4$	81.5
			MgAg	80.9			MgAg	80.9		

3.2 Cell types, cell culture, and mitomycin C treatment

Table 4 lists all immortalized cell lines and primary cells used in this study.

Table 4 | Cell lines and primary cells.

Name	Species & cell type	Supplier/provider
LN229	human GBM	kindly provided by Prof. Dr. Dr. Janka Held-Feindt University Medical Center Schleswig-Holstein, Campus Kiel
A172	human GBM	
HMC3	human microglia	kindly provided by PD Dr. Kirsten Hattermann-Koch Anatomical Institute, Kiel University
L929	murine fibroblast	Sigma-Aldrich Chemie GmbH, Munich, Germany
Astrocytes	human astrocytes	Life Technologies GmbH, Darmstadt, Germany

L929 cells were cultured in Nunclon™ Delta surface-treated T75 flasks (Life Technologies GmbH, Darmstadt, Germany); all other cell types were cultured in T75 flasks for adherent cells (Greiner Bio-One GmbH, Frickenhausen, Germany). All cells were grown in Dulbecco's Modified Eagle's Medium (DMEM, Life Technologies GmbH, Darmstadt, Germany) supplemented with 10 % fetal bovine serum (FBS, Biochrom GmbH, Berlin, Germany) or 15 % FBS (astrocytes) at 37 °C in a humidified atmosphere (5 % CO_2, 20 % O_2, 95 % relative humidity (rH)) in a Heraeus BB 6220 incubator (Life Technologies GmbH, Darmstadt, Germany). Passaging was performed at 70-90 % confluence dependent on the cell type. Primary astrocytes were used up to passage 13, HMC3 and L929 up to passage 30 and GBM cells up to passage 50. For passaging, the old culture medium was aspirated from the flask, and the cells were washed with phosphate-buffered saline (PBS, Life Technologies GmbH, Darmstadt, Germany). Subsequently, the cells were incubated with 0.05 % trypsin-ethylenediaminetetraacetic acid (EDTA; Life Technologies GmbH, Darmstadt, Germany) for 5 min at 37 °C. After incubation, the cells were resuspended in culture medium and transferred into a new flask.

A proliferation-inhibited sample group was introduced to facilitate the comparison of different cell types with different proliferative activity. The proliferation of the cell lines LN229, A172, and L929 was inhibited using mitomycin C from *Streptomyces caespitosus* (MMC, Sigma-Aldrich Chemie GmbH, Munich, Germany). Before MMC treatment, the cells were serum-starved in serum-free DMEM overnight at 37 °C in an incubator. MMC was dissolved in distilled water at a concentration of 0.5 mg/mL, sterile filtered (0.2 µm pore size, Life Technologies GmbH, Darmstadt, Germany) and diluted to a final concentration of 10 µg/mL in serum-free DMEM. Following serum-starvation, the serum-free medium was aspirated, and the cells were

incubated for 2 h with the MMC solution in T75 flasks under physiological conditions. Finally, the cells were washed three times with PBS and detached for subsequent seeding.

To characterize the proliferation of the different cell types on tissue culture plastic (TCP) and in contact with Mg-based materials, as well as to evaluate the efficacy and non-toxicity of the MMC treatment, DNA contents of 10^5 and 10^5 MMC-treated cells on Mg discs and TCP were measured at day zero, three and six. The cell proliferation was assessed by DNA quantification via Hoechst 33342 fluorescence intensity. For DNA isolation and quantification, lysis buffer, neutralization buffer, dilution buffer, and working buffer were prepared as follows:

(1) **Lysis buffer:**
Sodium hydroxide (NaOH, Sigma-Aldrich Chemie GmbH, Munich, Germany) and EDTA (Sigma-Aldrich Chemie GmbH, Munich, Germany) were diluted in distilled water at a concentration of 25 mM and 0.2 mM, respectively.

(2) **Neutralization buffer:**
Tris(hydroxymethyl)aminomethane (Tris, Sigma-Aldrich Chemie GmbH, Munich, Germany) was diluted in distilled water at a concentration of 40 mM. pH was adjusted to 5.5, using 10 % hydrochloric acid (HCl, Merck KGaA, Darmstadt, Germany).

(3) **Dilution buffer:**
NaCl (Merck KGaA, Darmstadt, Germany) and sodium citrate (Merck KGaA, Darmstadt, Germany) were diluted in distilled water at 2.5 M and 19 mM, respectively. pH was adjusted to 7.0 using 1 M HCl.

(4) **Working buffer:**
NaCl and sodium citrate were diluted in distilled water at 2 M and 15 mM, respectively. pH was adjusted to 7.0 using 1 M HCl.

Cells were lysed with lysis buffer for 5 min at 37 °C. The lysate was then boiled at 98 °C for 1 h in a thermoshaker (Thermomixer comfort, Eppendorf Vertrieb Deutschland GmbH, Hamburg, Germany) with 1000 rpm and subsequently cooled down to 15 °C at 700 rpm. Afterwards, an equal volume of neutralization buffer was added to the lysate, and the mixture was centrifuged (Heraeus Biofuge Pico, Kendro Laboratory Products GmbH, Osterode, Germany) at 13 000 rpm for 1 min. Human genomic DNA (Sigma-Aldrich Chemie GmbH, Munich, Germany) was selected to prepare the DNA standard curve ranging from 0 µg/mL to 3 µg/mL (obtained from serial dilution with DNA dilution buffer). Samples were diluted 1:5 before measurement using dilution buffer, if necessary. Standards and samples (50 µL each) were pipetted into a 96-well plate (Greiner Bio-One GmbH, Frickenhausen, Germany) in triplicates and incubated with 50 µL of working buffer and 50 µL of 2 µg/mL Hoechst 33342 per well for 15 min at room temperature in the dark. A VICTOR3 multilabel plate reader

(PerkinElmer Cellular Technologies Germany GmbH, Hamburg, Germany) was used to measure Hoechst 33342 fluorescence at an excitation wavelength of 355 nm and an emission wavelength of 460 nm.

3.3 Immersion test

The *in vitro* degradation rate of Mg discs and Mg-based thin films, was determined by measuring the weight loss of the cell-seeded materials over a period of time during immersion in a degradation medium. Such immersion tests were conducted for Mg discs, as well as for Mg-based thin films as follows:

Mg discs

The cell influence on Mg disc degradation was analyzed in a semi-static immersion test (i.e., replacement of entire medium by fresh medium every two to three days to prevent medium saturation). Mg specimens were wet-ground with silicon carbide (SiC) paper (1200 grit size, Hermes Schleifmittel GmbH, Hamburg, Germany) and subsequently cleaned in an ultrasonic bath (Branson 1210, Branson Ultrasonics Corp., Danbury, USA) for 20 min in n-hexane, 20 min in acetone, and 3 min in ethanol (Merck KGaA, Darmstadt, Germany). After cleaning, the Mg discs were dried, individually weighed (SBA 32, Scaletec Mechatronics Pvt. Ltd., Vadodara, India), and finally sterilized in 70 % ethanol (Merck KGaA, Darmstadt, Germany) for 20 min. The sterile and dried Mg discs were transferred into 12-well plates coated with 1 % agarose (AppliChem GmbH, Darmstadt, Germany). Agarose coating was used to prevent preferential cell attachment on the inert TCP. To simulate the initial body fluid/blood interaction with the biomaterial directly after implantation, the Mg discs were pre-incubated in DMEM with 10 % FBS overnight at 37 °C in an incubator. Subsequently, cells were seeded with the initial cell numbers shown in Table 5 in a volume of 40 µL cell suspension/sample. Mg discs were incubated with 40 µL cell suspension for 30 min at 37 °C in an incubator to allow cell adhesion. Finally, the discs were immersed in an additional 2 mL DMEM with 10 % FBS for a further six days. Medium exchange was performed after pre-incubation and at day three after cell seeding.

Table 5 | Cell seeding densities and cell treatment for degradation analysis of Mg discs.

Cell type	10^4 cells	5 x 10^4 cells	10^5 cells	10^5 cells + MMC
LN229	+	+	+	+
A172	-	-	+	+
Astrocytes	+	+	+	-
L929	+	+	+	+
HMC3	+	+	+	-

After immersion, samples were treated with chromic acid (CrA, 180 g/L chromium (VI) oxide in distilled water, VWR International, Darmstadt, Germany) to remove the degradation layer for 20 min, cleaned with water and ethanol, and weighed. The degradation rate DR was calculated using the following equation [108]:

$$\mathrm{DR} = \frac{\mathrm{K} \cdot \mathrm{W}}{\mathrm{A} \cdot \mathrm{T} \cdot \mathrm{D}} \tag{5}$$

Where K is a constant ($\mathrm{K} = 8.76 \cdot 10^4$ for degradation rate in mm/a); W is the mass loss in g; A is the exposed surface area in cm^2; T is the immersion time in h, and D is the density in g/cm^3.

Osmolality (Osmomat 030, Gonotec Meß- und Regeltechnik GmbH, Berlin, Germany) was determined at each medium exchange and after six days for cells seeded on Mg and on TCP. Cell-induced osmolality changes were observed by calculating Δosmolality using the following equation:

$$\Delta\mathrm{osmolality} = \mathrm{osmolality}_{\mathrm{Mg+cells}} - \mathrm{osmolality}_{\mathrm{Mg}} \tag{6}$$

With $\mathrm{osmolality}_{\mathrm{Mg+cells}}$ representing the osmolality measured for Mg seeded with cells and $\mathrm{osmolality}_{\mathrm{Mg}}$ representing the osmolality determined for the material control (without cells).

Mg thin films

Pure Mg and Mg-6Ag thin films were analyzed under semi-static immersion conditions to test their stability under physiological conditions and suitability for further *in vitro* and *in vivo* analysis. The thin films were cleaned, weighed (MYA 2.4Y microbalance, Radwag Balances and Scales, Radom, Poland) and sterilized following the procedure described above for Mg disc. After cleaning, the thin films were sterilized in 70 % ethanol in a 24-well plate (Greiner Bio-One GmbH, Frickenhausen, Germany) for 20 min. Sterile and dried specimens were transferred into a fresh 24-well plate coated with 1 % agarose and pre-incubated in DMEM with 10 % FBS overnight at 37 °C in an incubator. Pure Mg thin films were fixed at the well plate bottom using membrane-free inserts (Life Technologies GmbH, Darmstadt, Germany) as shown in Figure 5, to reduce film bending. After pre-incubation, 10^5 LN229, HMC3 cells and astrocytes were seeded on top of the thin films in a volume of 10 µL cell suspension/sample and were allowed to adhere for 30 min. Subsequently, the samples were immersed in an additional 2 mL of DMEM with 10 % FBS at 37 °C in an incubator for three days. CrA treatment for 5 min was used for degradation layer removal. The degradation rate was calculated as described above for Mg discs.

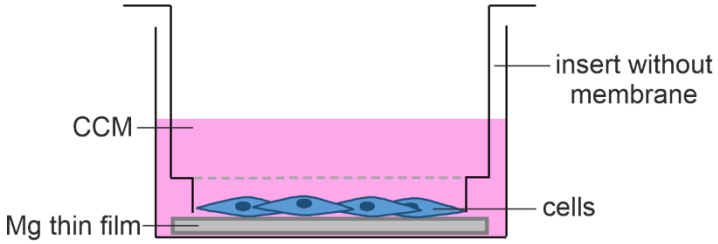

Figure 5 | Experimental set-up for the *in vitro* degradation of pure Mg thin films. A membrane-free well-plate insert was used to reduce thin film bending.

pH (Sentron SI600 with MiniFET probe, Sentron Europe B.V., Leek, The Netherlands) and osmolalities were measured after pre-incubation and after three days. To observe degradation-related pH changes, ΔpH was calculated using the following equation:

$$\Delta\mathrm{pH} = \mathrm{pH}_{\mathrm{Mg}} - \mathrm{pH}_{\mathrm{M}} \tag{7}$$

Where pH_M is the pH measured for medium without Mg and pH_{Mg} is the pH determined for medium with Mg. Likewise, degradation-induced changes in osmolality were calculated using equation 8.

$$\Delta\mathrm{osmolality} = \mathrm{osmolality}_{\mathrm{Mg}} - \mathrm{osmolality}_{\mathrm{M}} \tag{8}$$

With $osmolality_M$ representing the osmolality measured for medium without Mg and $osmolality_{Mg}$ representing the osmolality determined for medium with Mg.

The thin film appearance before and after degradation was documented using a stereo microscope (Wild M37, Leica Mikrosysteme Vertrieb GmbH, Wetzlar, Germany).

3.4 Biological material evaluation

The biological material evaluation was performed for Mg discs as well as for Mg-based thin films employing a cell viability staining, a morphology staining and DNA quantification focusing on multiple objectives. The cell viability staining was conducted to confirm the presence of neural cells on Mg discs after/during degradation and thus to verify that the observed degradation effects were indeed cell related. Moreover, the cell viability staining was employed to visualize the cell distribution on Mg discs. This cell distribution analysis in combination with the DNA quantification were used to investigate the effect of dense cell layers on Mg degradation. Lastly, the cell viability as well as the cell morphology staining were performed to study the suitability of Mg-based materials (especially thin films with varying degradation rates) for neural applications.

3.4.1 Viability and distribution of neural cells in contact with Mg-based materials

The viability of neural cells in contact with slower-degrading Mg-based materials (e.g., Mg discs, slow-degrading Mg-based thin films) was assessed in direct material contact. The effect of fast-degrading Mg-6Ag thin films, however, was analyzed in indirect material contact (i.e., materials were placed on top of an adherent cell layer), as these thin films were not stable enough for direct cell seeding. The cell viability analysis in direct and indirect material contact was performed as follows:

Direct contact

Cell viability and distribution were determined employing a live and dead cell staining using calcein AM (Life Technologies GmbH, Darmstadt, Germany) as a stain for live cells (appearing in green) and ethidium homodimer-1 (Sigma-Aldrich Chemie GmbH, Munich, Germany) for dead (red) cells. For the viability analysis of cells on thin films, cells were additionally nuclei-counterstained with Hoechst 33342 (Life Technologies GmbH, Darmstadt, Germany). Calcein AM, ethidium homodimer-1, and Hoechst 33342 were diluted in serum-free DMEM at 1 µM, 2 µM, and 2 µg/mL, respectively. The cells were washed with serum-free medium after six days of culture on Mg discs (compare Table 5), or after three days of culture on thin films (10^5 LN229, HMC3 cells and astrocytes) and incubated with the staining solution for 20 min in an incubator. Afterwards, cell viability and distribution were evaluated using a Nikon Eclipse Ni epi-fluorescence microscope (Nikon GmbH, Düsseldorf, Germany), or a Leica TCS SP8 confocal microscope (Leica Mikrosysteme Vertrieb GmbH, Wetzlar, Germany). Table 6 lists the excitation and emission wavelengths used for image acquisition with the confocal microscope.

Table 6 | Excitation (λ_{ex}) and emission (λ_{em}) wavelengths used for different fluorescent dyes.

Dye	λ_{ex} in nm	λ_{em} in nm
Calcein AM	488	515
Ethidium homodimer-1	552	617
Hoechst 33342	405	450

Indirect contact

To analyze the cytotoxicity of fast-degrading Mg-6Ag thin films (DR>1.5 mm/a) on selected brain cells, 10^4 LN229, HMC3 cells and astrocytes were seeded in a 24-well plate and were left to adhere overnight in an incubator. Fast-degrading Mg-6Ag thin films (provided by Lea Jessen, GRK2154-P1a) were sterilized in 70 % ethanol for 20 min and subsequently dried under sterile conditions. After ca. 12 h, cell supernatants were collected for osmolality and pH

measurements. The sterile thin films were carefully placed on top of the adherent cells and 2 mL of fresh DMEM + 10 % FBS was added. The cells were then incubated with the thin films for a further 24 h under cell culture conditions. Cells without the addition of Mg-6Ag thin films were cultured as a reference. Following incubation, the degraded thin films were removed and the supernatant was collected for osmolality and pH measurements to monitor the thin film degradation speed. Cell viability was visualized via staining with 1 µM calcein AM and 2 µg/mL Hoechst 33342 in serum-free DMEM for 20 min. Microscopic images of the entire well surface were taken using a Nikon eclipse Ti-S/L100 inverted epi-fluorescence microscope (Nikon GmbH, Düsseldorf, Germany) and the number of viable cells was counted employing the ImageJ software (v.1.8.0_112, Rasband, W.S., https://imagej.nih.gov/ij/).

3.4.2 Cell morphology on Mg-based materials

A cytoskeleton staining was applied to visualize the cell morphology on Mg based materials. The cytoskeleton staining was conducted using fluorescently labeled phalloidin, i.e., a toxin which shows a high binding affinity to F-actin, a major structural cytoskeleton protein of eukaryotic cells [109].

Cell morphology was monitored on Mg discs (10^5 LN229, A172, L929, HMC3, astrocytes and 10^5 MMC-treated LN229, A172, L929) and on Mg-6Ag thin films (10^5 LN229, HMC3, astrocytes) after six and three days of culture, respectively. Cells seeded and stained on glass cover slips (VWR International, Darmstadt, Germany) were selected as control. For the actin staining with tetramethylrhodamine (TRITC)-conjugated phalloidin (Sigma-Aldrich Chemie GmbH, Munich, Germany), the cells were fixed in 2 % paraformaldehyde (Alfa Aesar GmbH & Co KG, Karlsruhe, Germany) in PBS + 20 % FBS for 20 min and subsequently permeabilized with 0.5 % Triton X-100 (Sigma-Aldrich Chemie GmbH, Munich, Germany) in PBS + 20 % FBS for a further 20 min at room temperature. After permeabilization, the cells were washed with DMEM + 1 % bovine serum albumin (BSA, Carl Roth GmbH + Co. KG, Karlsruhe, Germany). The staining solution was prepared by diluting TRITC-conjugated phalloidin and 4′,6-diamidino-2-phenylindole (DAPI, Sigma-Aldrich Chemie GmbH, Munich, Germany) in DMEM + 1 % BSA to a final concentration of 0.12 µg/mL and 5 µg/mL, respectively. Finally, the samples were incubated in staining solution for 30 min at room temperature and were analyzed with a Leica TCS SP8 confocal microscope using the excitation and emission wavelengths listed in Table 7.

Table 7 | Excitation (λ_{ex}) and emission (λ_{em}) wavelengths used for TRITC and DAPI.

Dye	λ_{ex} in nm	λ_{em} in nm
TRITC	552	576
DAPI	405	450

3.4.3 Cell amount on Mg discs after degradation

The cell amount on Mg discs after six days of immersion was quantified via DNA measurement for 10^4, 10^5 and 10^5 MMC-treated cells (compare Table 5), to assess the influence of cell density on the degradation outcome. DNA isolation was performed as described above in chapter 3.2.

3.5 Degradation product/layer analysis

The degradation layer composition and depth of cell-seeded Mg discs were analyzed employing electron microscopic as well as infrared spectroscopic methods to elucidate if and how different types of neural cells impact the formation of degradation products. Eventually, the information obtained from this analysis was used to evaluate the underlying cell-induced Mg degradation mechanisms. Following, the different experimental set-ups and objectives are explained in detail.

3.5.1 Electron microscopy

Scanning electron microscopy (SEM) is a microscopic technique which uses a focused electron beam to image materials by scanning their surface. The interaction of an electron beam with the atoms of a material creates typical signals (Figure 6), such as secondary electrons (SE), back scattered electrons (BSE), x-rays, auger electrons, and photons (cathodoluminescence), which can be used for imaging (SE, BSE) and elemental identification (auger electrons, x-rays) [110]. Low-energy SEs are generated at the sample surface and are used to obtain information on the sample topography. BSEs are generated at higher penetration depths of the primary electron beam, resulting in higher electron energies compared to SEs. The generation of BSEs is highly dependent on the atomic number of the analyzed elements. Therefore, images obtained from BSEs can give information on the material composition (z-contrast). Characteristic x-rays emerge from a sample when an incident electron from the primary electron beam ejects an electron of the inner shell of an atom, creating an electron hole, which is then filled by an electron of a higher energy level [111]. Energy dispersive x-ray spectroscopy (EDX) measures the energy of the emitted characteristic x-rays and allows elemental identification.

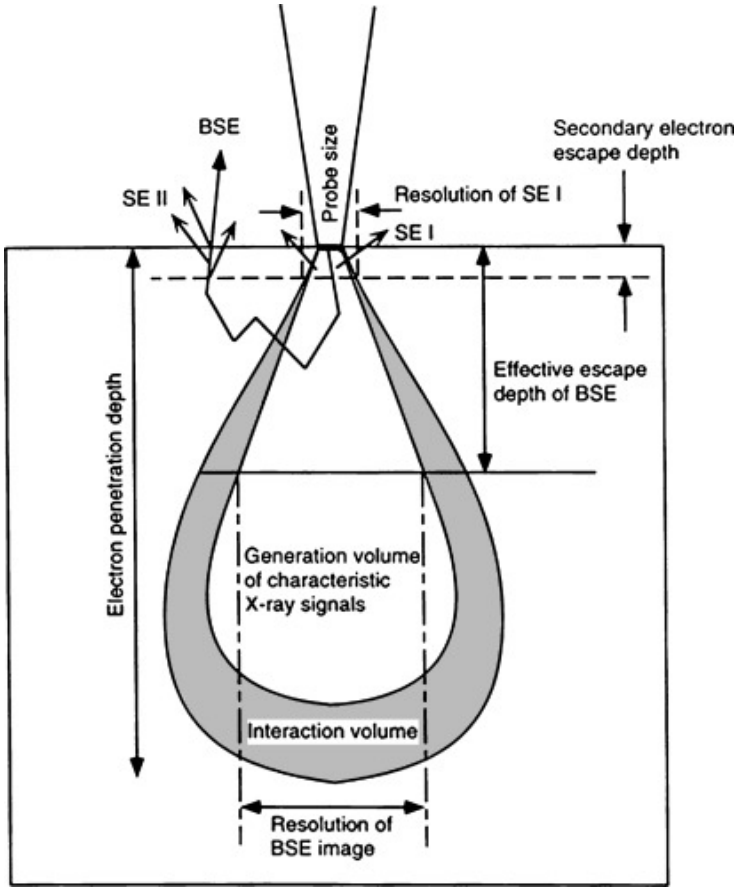

Figure 6 | Schematic illustration of some signals generated and used in SEM. SEs and BSEs are primarily used for image acquisition, while x-rays are employed for elemental identification. Reproduced from [110] with permission from Elsevier.

Electron microscopic analysis was performed to investigate the following aspects:

Surface morphology after degradation

The surface morphology before and after degradation product removal was analyzed for samples seeded with 10^5 HMC3 cells, 10^5 untreated and 10^5 MMC-treated LN229 cells, and without cells six days post immersion via SEM. These cell types/cell densities were chosen as they represent the samples exhibiting the highest and lowest degradation rates, respectively. Samples analyzed before degradation product removal were fixed in 2.5 % glutaraldehyde (Sigma-Aldrich Chemie GmbH, Munich, Germany) overnight and treated with 1 % osmium tetroxide (Sigma-Aldrich Chemie GmbH, Munich, Germany) for 30 min. An ascending alcohol series (20 %, 40 %, 60 %, 80 %, and 100 % 2-propanol; Merck KGaA, Darmstadt, Germany) was used to dehydrate the samples. The samples were immersed in the alcohol solutions for 1 h per solution and subsequently critical point dried (Leica EM CPD030, Wetzlar, Germany). Samples without degradation products (after CrA treatment) were not treated further. A VEGA3 SEM (Tescan GmbH, Dortmund, Germany) was used to perform SEM analysis,

imaging the region of interest utilizing an acceleration voltage of 2 keV (before CrA treatment), or 16 keV (after CrA treatment) and a SE detector.

Degradation layer cross section analysis

To analyze the degradation layer thickness and composition, cross section analysis of Mg cultured with cells for six days was carried out via SEM/EDX with focused ion beam (FIB) milling. The following specimens were investigated: Mg seeded with 10^5 LN229, A172, L929, HMC3, astrocytes, and 10^5 MMC-treated LN229, A172, and L929. All samples were fixed, dehydrated and critical point dried as described above. Critical point dried samples were mounted on SEM sample holders and sputtered with gold palladium. The analysis was done using an Auriga SEM (Zeiss, Oberkochen, Germany) equipped with an EDX device (Apollo XP; Ametek GmbH, Wiesbaden, Germany), and a LYRA3 SEM (Tescan GmbH, Dortmund, Germany) likewise equipped with an EDX detector (Oxford Instruments GmbH, Wiesbaden, Germany). Both SEMs additionally featured a gallium FIB source. FIB cross sectioning was performed at a densely cell-seeded spot. Images of the region of interest were taken with an acceleration voltage of 5 keV before FIB milling using a SE detector. Cross sectioning was achieved by rough FIB milling at 30 keV and subsequent fine milling at 15 keV. Images of the prepared cross-section, as well as the successive EDX analysis, were obtained at an acceleration voltage of 15 keV with a SE or BSE detector. Element distribution along the degradation layer was determined using EDX line scans, monitoring the elements: Mg, carbon (C), nitrogen (N), oxygen (O), sodium (Na), P, sulfur (S), potassium (K), and Ca.

3.5.2 Infrared spectroscopy

Infrared (IR) spectroscopy was additionally conducted to investigate the surface-near composition of the degradation layer growing on Mg discs cultured with cells.

IR spectroscopy is based on the excitation of molecular vibrations using IR radiation. The amount of energy required for the stimulation of molecule vibrations is characteristic for certain molecules/bonds [112]. Therefore, IR spectroscopy facilitates the identification and structural elucidation of unknown substances. Substances analyzed via IR spectroscopy, are required to be “IR-active”, i.e., the molecules need to undergo a change in dipole moment [112] upon excitation. IR spectroscopy typically measures the transmission, absorbance, or reflectance of IR light versus the frequency/wavenumber (ca. 4000 - 400 cm^{-1}) to create IR spectra for analysis.

Specimens used for IR analysis were: Mg without cells and with 10^5 LN229 and astrocytes, as well as 10^5 MMC-treated LN229. IR spectra were obtained using an IR microscope (Bruker Tensor 27 and Hyperion 200; Bruker GmbH, Mannheim, Germany) in reflectance mode.

Spectra were collected at three different sample areas and were averaged from 256 scans with a resolution of 2 cm^{-1}.

3.6 Cell metabolism analysis

Cell metabolism, and as a consequence thereof cell-related pH changes, can be a major impact factor for Mg degradation. Hence, the cell metabolic activity was analyzed assessing lactate levels, bulk and local pH to elucidate cell-induced degradation mechanisms. Following, the experimental set-ups used to quantify the cell metabolic activity are described in detail.

3.6.1 Lactate content

To preserve cellular pH homeostasis, excess lactate and H^+, generated during glycolysis and ATP breakdown, are extruded from the intracellular space through various transporter mechanisms as described in chapter 1.3.1. Therefore, supernatant lactate concentrations can be used as an indirect indicator for cell metabolic activity and cell-induced local acidification. Extracellular lactate was analyzed using a lactate detection kit (Lactate-GloTM Assay, Promega GmbH, Walldorf, Germany), which is based on a multi-step enzymatic conversion of lactate into a bioluminescent signal as shown in Figure 7.

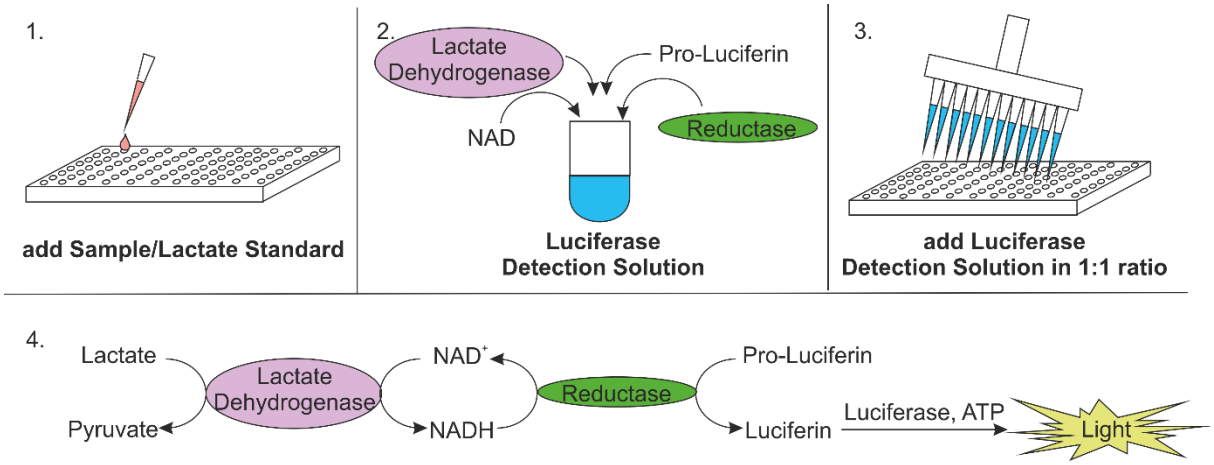

Figure 7 | Function principle of the lactate detection kit. Lactate is converted into a bioluminescent signal in a multistep enzymatic reaction.

Lactate dehydrogenase (LDH) is used to catalyze the conversion of the lactate sample to pyruvate. This process is accompanied by the simultaneous reduction of nicotinamide adenine dinucleotide (NAD^+/NADH) from NAD^+ to NADH. NADH, in turn, is involved in the enzymatic conversion of a pro-luciferin reductase substrate to luciferin. The luciferin generated in this way is then oxidized in the presence of luciferase, creating a bioluminescent signal, which can be plotted as a function of lactate concentration.

Supernatant lactate contents were measured for 10^4, 10^5, and 10^5 MMC-treated cells on Mg discs after six days of culture. Depending on the estimated lactate content, samples were diluted 1:50, 1:100, or 1:500 with PBS. The lactate standard curve ranged from 0 to 200 µM and was obtained from serial dilution with PBS. DMEM + 10 % FBS without cells was used as a control blank. 50 µL of standards, blank, and samples were pipetted into a white-walled 96-well plate (PerkinElmer Cellular Technologies Germany GmbH, Hamburg, Germany) in duplicates. The lactate detection reagent for the analysis of 96 wells was prepared by mixing 5 mL luciferin detection solution with 50 µL of reductase, reductase substrate, LDH, and NAD^+ reagents. All wells were incubated with 50 µL of the lactate detection reagent for 60 min at room temperature. Luminescence was then recorded using a VICTOR3 multilabel plate reader.

3.6.2 Bulk pH

Bulk pH is a term to describe the global solution pH. Even though bulk pH can largely differ from local pH (e.g., surface pH of a degrading Mg material), changes in bulk pH can provide valuable information on degradation and cell metabolic processes in *in vitro* degradation systems. The bulk pH changes induced by cell metabolism and pH homeostasis were analyzed by supernatant pH measurement of Mg and TCP seeded with cells and subsequent calculation of ∆pH as shown in equation 9.

$$\Delta\mathrm{pH} = \mathrm{pH}_{\mathrm{Mg+cells}} - \mathrm{pH}_{\mathrm{Mg}} \quad (9)$$

Where $pH_{Mg+cells}$ represents the pH measured for cells on Mg and pH_{Mg} represents the pH determined for Mg without cells.

∆pH was determined for 10^4, 5 x 10^4, 10^5 and 10^5 MMC-treated cells (LN229, A172, L929, HMC3, astrocytes) on Mg and TCP after three and six days of culture.

3.6.3 Local pH

The scanning ion-selective electrode technique (SIET) uses ion-sensitive microelectrodes to measure local ion concentrations in aqueous media at very low concentrations (detection limit is 0.01 pH units for the electrodes used in this thesis) [113, 114]. In this thesis, the concentration of H^+ (local pH) was measured, but the method can also be used to analyze the concentration of other ions, such as Ca^{2+}, K^+, Na^+ and Cl^- (using respective microelectrodes). A SIET set-up (Figure 8) includes one or multiple microelectrodes, a reference electrode, a camera and light source to view the sample, as well as a set of stepper motors which allow microelectrode movement in x, y and z direction. Therefore, SIET offers a versatile range of

feasible measuring set-ups (e.g., 2D mapping, line scans, resting probe). Local ion concentrations are recorded potentiometrically via the measurement of voltage changes in the analyzed electrolyte and the read-outs are processed by a connected computer [113]. The spatial resolution of the technique is dependent on the microelectrode tip size (100-250 µm for the electrodes used in this thesis).

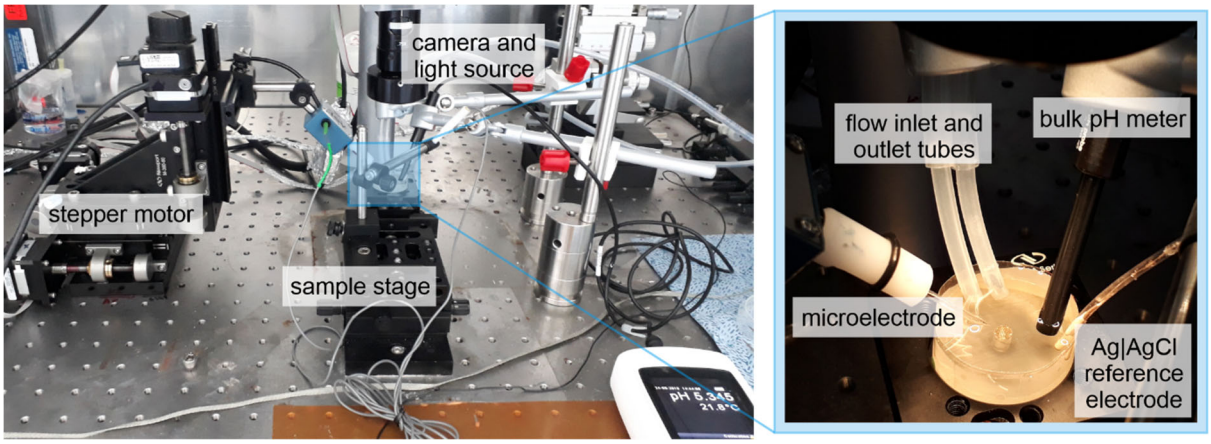

Figure 8 | Experimental SIET set-up. The set-up can be adapted for the use of two simultaneously measuring electrodes.

For local pH analysis of cells on Mg substrates, HP Mg rods with a diameter of 4 mm (Helmholtz-Zentrum Geesthacht, Geesthacht, Germany) were embedded in epoxy resin (EpoxyCureTM 2 resin and hardener, Buehler, Lake Bluff, USA), ground (4000 grit size; Hermes Schleifmittel GmbH, Hamburg, Germany), and sterilized in an ultrasonic bath in 70 % ethanol for 30 min. The sterile specimens were then wrapped with adhesive tape under sterile conditions to form a container for medium storage on top of the embedded sample, as shown in Figure 8 (right). The samples were pre-incubated in 2 mL DMEM + 10 % FBS overnight in an incubator. LN229 cells (10^5) were seeded on the SIET sample in a volume of 10 µL medium and were allowed to adhere for 15-30 min. Afterwards, 2 mL of culture medium was added and the cells were cultured for five or six days. Medium was exchanged after three days of culture. Specimens immersed in DMEM + 10 % FBS without cells were used as a reference. Before the SIET measurement, the cells were stained with 1 µM calcein AM to visualize the cell distribution on Mg. Further, DMEM + 10 % FBS was replaced by serum-free DMEM for the measurement itself to avoid blockage of the pH probe as a result of protein adsorption. The analysis of localized pH was performed using a commercial SIET/SVET/DVIT system (Applicable Electronics,LLC, Sandwich, USA) with the corresponding ASET-LV4 software (Science Wares, Inc., Falmouth, USA). pH-sensitive glass-capillary micro-electrodes with a tip orifice diameter of 1.5-3 µm and filled with hydrogen ionophore I (cocktail B; Sigma-Aldrich Chemie GmbH, Munich, Germany) were used to record pH development. The microelectrode

was positioned at a distance of ca. 100 µm above the sample's surface and was stepwise moved (100 µm/step) in x and y direction for near-surface scans. The measurement was performed under static conditions, and under flow using a flow speed of 0.66 mL/min generated by a peristaltic pump (TL15E; MDX Biotechnik International GmbH, Nörten-Hardenberg, Germany).

The local pH around cells on inert substrates was measured as a reference to quantify the magnitude of cell-induced pH changes. A volume of 10 µL containing 10^4 LN229 cells was seeded on plastic petri dishes (Life Technologies GmbH, Darmstadt, Germany) and was left to adhere for 15-30 min to ensure that cell attachment was limited to one local spot. Afterwards, 3 mL of DMEM + 10 % FBS was added and the cells were cultured for four to six days. The bicarbonate pH buffer system in DMEM is formulated for the use in atmospheres with 5-10 % CO_2. However, SIET measurements were performed under atmospheric conditions (ca. 0.04 % CO_2). Therefore, the DMEM used for SIET measurements was CO_2-equilibrated, to avoid a rapid pH increase of the cell culture medium during SIET measurements due to the exposure to atmospheric conditions. For medium CO_2-equilibration, the lid of a bottle of serum-free DMEM was unscrewed and left open overnight under sterile conditions to allow gas exchange. SIET measurements were performed with a resting probe set-up, using two commercial pH-sensitive glass micro-electrodes (Unisense a/s, Aarhus, Denmark). One micro-electrode was positioned above the cell layer, while the other microelectrode was positioned above a cell-free area. Both electrodes were positioned at the same height, ca. 50 µm above the cell surface, and were left at their positions throughout the entire measurement duration (resting probe). Measurements were performed under static conditions in CO_2-equilibrated, serum-free DMEM for ca. 1 h. Reference measurements on cell-free petri dishes were carried out to determine the calibration error and drift speed of both electrodes.

∆pH was calculated from the single probe read-outs using the following equations:

$$\Delta\mathrm{pH} = \mathrm{pH}_{\mathrm{no\ cells}/2} - \mathrm{pH}_{\mathrm{cells}/1} - \overline{\Delta\mathrm{pH}}_{\mathrm{reference}} \quad (10)$$

$$\Delta\mathrm{pH}_{\mathrm{reference}} = \mathrm{pH}_{\mathrm{reference}/2} - \mathrm{pH}_{\mathrm{reference}/1} \quad (11)$$

$pH_{no\ cells/2}$ and $pH_{cells/1}$ represent the absolute probe read-outs for the electrode above a cell-free area and for the electrode above cells, respectively. $pH_{reference/2}$ and $pH_{reference/1}$ refer to the single electrode read-outs during a reference measurement.

3.7 Extracellular matrix analysis

Apart from metabolites cells actively secret ECM products. These ECM products are likely in direct contact with the subjacent Mg-based material and may thus influence Mg degradation. In this thesis, the ECM of different neural cell types was analyzed to clarify if and how selected ECM molecules impact Mg degradation. For this purpose, the content, distribution and chemical interaction (with a Mg-based substrate) of collagen (type IV), chondroitin sulfate (CS) and HA were examined as representative compounds of the brain ECM. The detailed experimental set-ups are described below.

3.7.1 Collagen type IV content

The collagen type IV content was determined by measuring the supernatant arresten content using enzyme-linked immunosorbent assays (ELISA). Arresten is a 26 kDa α1-chain fragment of collagen type IV [115] and can therefore be used to determine collagen type IV contents indirectly. ELISA is an antibody-based technique to quantify an antigen (e.g., protein) in liquid samples. The sandwich ELISA (Figure 9), an ELISA subtype, is based on the use of two antibodies (capture and detection antibody) specific to the same antigen. In a first step, the antigen binds to a capture antibody, which was used beforehand to coat a substrate (e.g., microplates). Afterwards, a second antibody (detection antibody) additionally binds to the antigen creating the "sandwich". A reporter enzyme (typically horse radish peroxidase (HRP)) is employed to bind to the detection antibody and to catalyze a color reaction which can be measured via the absorbance using a microplate reader.

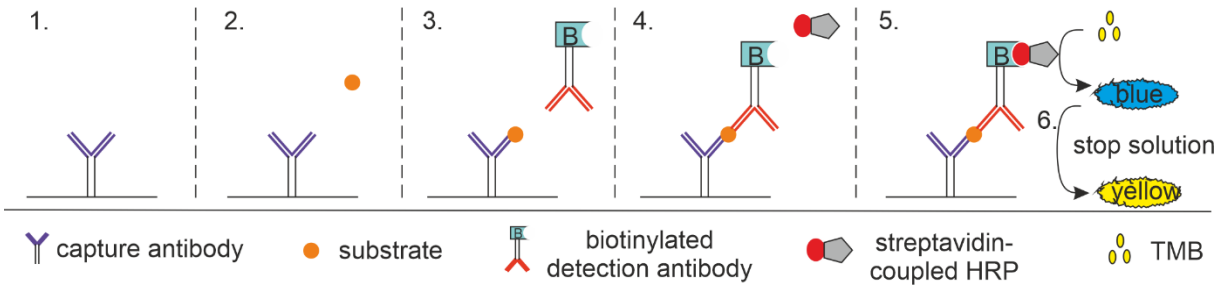

Figure 9 | Simplified principal of sandwich ELISAs. Antigen quantification is accomplished by a multistep binding process of two antibodies to the antigen and a subsequent enzyme-catalyzed color reaction with 3,3′,5,5′-tetramethylbenzidine (TMB).

The supernatant arresten contents of 10^5, and 10^5 MMC-treated cells seeded on Mg and TCP were analyzed six days post immersion using a human arresten DuoSet® ELISA (R&D Systems, Abingdon, UK) and a mouse arresten ELISA kit (MyBioSource, Inc., San Diego, USA) according to the manufacturer's instructions for the kits.

3.7.2 Extracellular matrix distribution

The ECM distribution was evaluated via GAG staining with the fluorescein isothiocyanate (FITC) conjugated lectins (Vector Laboratories Inc., Burlingame, USA) wheat germ agglutinin (WGA) and soybean agglutinin (SBA). WGA and SBA specifically bind to the sugar moieties *N*-acetylglucosamine (glcNAc) and *N*-acetylgalactosamine (galNAc), respectively. It can be assumed, that WGA stains HA and SBA stains CS with sufficient specificity, since glcNAc is one of two monomers present in HA and galNAc occurs in CS [116, 117]. To visualize collagenous parts of the ECM, the Col-F collagen-binding reagent (ImmunoChemistry Technologies LLC, Bloomington, USA) was used. Col-F shows an unspecific affinity to elastin and collagen. The cells were nuclei-counterstained with 2 µg/mL Hoechst 33342 and incubated with 10 µg/mL WGA/SBA or 15 µM Col-F in serum-free DMEM for 30 min at physiological conditions. Staining was performed after six days of culture on Mg for 10^4, and 10^5 LN229, astrocytes, L929, HMC3, and 10^5 MMC-treated LN229 cells. The specimens were examined with a Leica TCS SP8 confocal microscope (Mg) and a Nikon Eclipse Ni epi-fluorescence microscope (Mg, full surface scans). FITC-conjugated compounds were imaged at an excitation and emission wavelengths of 488 nm and 515 nm, respectively. Hoechst 33342 fluorescence was measured at the excitation and emission wavelengths given in Table 6 and Table 7. The ImageJ software was employed to determine the ratio of green to blue fluorescently stained sample area on full surface scans.

3.7.3 Interaction of extracellular matrix molecules with Mg

The impact of HA, CS and collagen type IV on Mg degradation as well as the detailed chemical interaction of these ECM molecules with a Mg-based substrate were analyzed using immersion tests and attenuated total reflection (ATR)-Fourier-transform infrared spectroscopy (FTIR) as described below.

Immersion test

The influence of single ECM compounds on the Mg degradation rate was investigated in semi-static immersion tests. HA and CS were chosen as GAG representatives of the brain ECM. Collagen type IV was selected as a relevant protein for analysis. The immersion media were prepared by dissolving or diluting the selected molecules in distilled water at the following concentrations: 0.05 M CS (Sigma-Aldrich Chemie GmbH, Munich, Germany), 0.01 M HA (Sigma-Aldrich Chemie GmbH, Munich, Germany), and 0.003 mM collagen type IV (CellSystems GmbH, Troisdorf, Germany). These concentrations either equaled the solubility limit of the molecules in water, or they corresponded with the minimum concentration required to obtain reliable data from subsequent IR spectroscopy measurements. The pH of the immersion media was adjusted to 6.5 ± 0.5 with 1 M HCl or 1 M NaOH for one medium group

and was left unadjusted for the second group of immersion media. Further, the immersion media were sterile filtered (pore size 0.2 µm).

Mg samples were ground, cleaned, and weighed following the standard procedure for immersion tests with discs, as already described in chapter 3.3. Sterile Mg discs were then incubated in 2 mL of the respective immersion media for six days. For the analysis with collagen type IV, an additional sample group of collagen-coated Mg discs was prepared. Mg discs were incubated with 40 µL of the 0.003 mM collagen type IV solution for 1 h in an incubator. Afterwards, 2 mL of distilled water were added as immersion medium. Medium exchange was performed after three days of immersion for all samples. After immersion, the samples were CrA treated for 20 min, weighed, and the degradation rate was calculated using equation 5.

pH and osmolalities were measured at each medium change, degradation-induced pH and osmolality changes were analyzed by calculating ΔpH and Δosmolality using equations 7 and 8.

In situ ATR-FTIR

The chemical interaction of ECM molecules and metabolites with Mg substrates was studied using ATR- FTIR in Kretschmann geometry to elucidate some of the underlying degradation mechanisms. These measurements were performed as part of a guest research stay at the Corrosion Technology and Electrochemistry Group under the supervision of Prof.dr.ir. J.M.C. Mol at TU Delft, Netherlands. ATR-IR spectroscopy is a specific IR-spectroscopic technique, which allows the surface analysis of opaque substrates. A major component of an ATR-IR spectrometer is the internal reflection element (IRE), for instance zinc selenide (ZnSe) or germanium (Ge) crystals. IREs have a higher refractive index than the analyte above the IRE. Thus, an incident IR beam undergoes total internal reflection at the IRE surface (Figure 10). This process of reflection causes the formation of an evanescent wave, which penetrates the analyte. The interaction of analyte and evanescent wave leads to a reduction in intensity of reflected light, elucidating the origin of the method's name [118]. The Kretschmann configuration (Figure 10) refers to a special ATR-IR set-up where a thin metal film is deposited directly on top of the IRE. In this set-up, the evanescent wave, created at the IRE-metal interface, interacts with the metal film. This process causes the formation of a so-called surface plasmon polariton, i.e., a kind of electromagnetic wave, which extends to the medium above the metal film (e.g., an electrolyte) and facilitates an *in situ* analysis of the metal-medium interface [119].

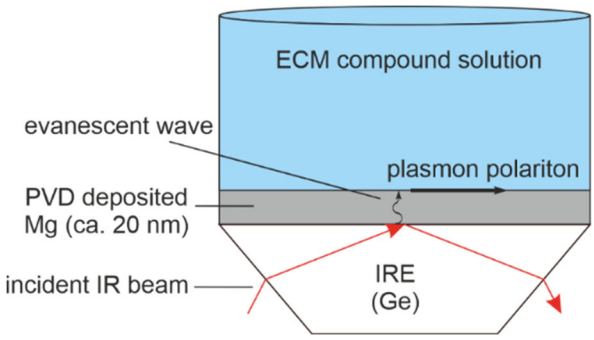

Figure 10 | ATR-FTIR set-up in Kretschmann geometry. The Kretschmann configuration enables to measure the interaction of ECM compound and the Mg substrate directly at the medium-material interface.

Mg substrates were fabricated by physical vapor deposition (PVD) of HP Mg (Mg discs, compare chapter 3.1, Helmholtz-Zentrum Geesthacht, Geesthacht, Germany) on Ge IREs (60°, PIKE Technologies, Inc., Madison, USA) using a VCM 600 standard vacuum thermal evaporator (Norm Electronics Ltd., Athens, Greece). The Mg films obtained from this fabrication process exhibited a thickness of approximately 20 nm. ATR-FTIR measurements were performed using a Thermo-Nicolet Nexus FTIR spectrometer (Thermo Fisher Scientific Inc., Waltham, USA) equipped with a nitrogen-purged VeeMAX III single reflection ATR accessory (PIKE Technologies, Inc., Madison, USA). The angle of IR light incidence was set to 80°. The measurement of Mg deposited on germanium IREs and immersed in distilled water was used to obtain IR backgrounds. For molecule-Mg interaction analysis, the distilled water was replaced immediately after IR background acquirement by a compound-containing solution, and IR spectra were collected. ATR-FTIR measurements were conducted for 0.05 M CS and 0.01 M HA, with pH adjusted to 6.5 ± 0.5. IR spectra obtained from the immersion of the bare germanium IREs (without Mg) in the compound-containing solutions were used as a reference. Spectra were recorded every 3 s and averaged from 16 cycles with a resolution of 4 cm^{-1} until no change in the spectra could be observed anymore. Data evaluation was performed using the OMNIC 8.1 software (ThermoElectron Corporation, Madison, USA).

3.8 Statistical analysis

All data were obtained from three independent experiments with three or six replicates, unless indicated otherwise and are graphically presented as the arithmetical mean ± standard deviation (SD). Statistical analysis was performed using Prism (version 6, GraphPad Software, La Jolla, USA). The respective statistical tests used for each experiment are indicated individually for each result section.

4 Results

4.1 Proliferation of different neural cell types and mitomycin C treatment efficacy

The cell proliferation on TCP and Mg of all cell types used in this thesis is shown in Figure 11. All untreated cell types showed a significant increase in DNA content after six days of culture on TCP (Figure 11a), indicating proliferation for all cell types. While L929, both GBM cell lines and HMC3 cells exhibited high proliferation rates, astrocytes proliferated considerably slower. Likewise, the DNA contents of untreated L929, A172, LN229 and HMC3 cells increased substantially after six days of culture on Mg (Figure 11b), whereas DNA contents of astrocytes on Mg remained stable. Since primary astrocytes were used in this study, a very limited proliferative activity of these cells was expected and is hence not related to material effects.

As all cell types exhibited different proliferative activities, a MMC treatment was used to inhibit proliferation and to facilitate the direct comparison of the different cell types and their impact on Mg degradation. No significant increase in DNA content after six days of culture on either TCP or Mg discs was evident for any of the treated cell types, confirming the treatment efficacy and non-toxicity. At day six of culture a proliferation inhibition of ca. 90 % was achieved by MMC treatment for all cell types on TCP and Mg.

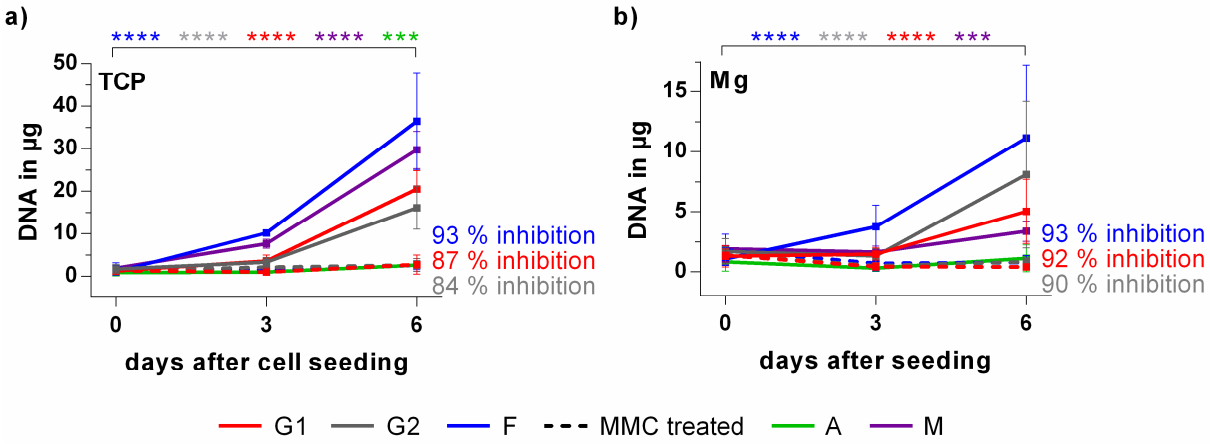

Figure 11 | MMC treatment efficacy and cell proliferation on Mg and TCP. a) Absolute DNA content in µg for 10^5 untreated and MMC-treated LN229 (G1), A172 (G2), L929 (F), astrocytes (A) and HMC3 (M) cells on TCP (n=3). **b)** Absolute DNA content in µg for 10^5 untreated and MMC-treated LN229 (G1), A172 (G2), L929 (F), astrocytes (A) and HMC3 (M) cells on Mg (n=3). Statistical analysis was conducted employing Mann-Whitney or t-test.

4.2 Mg disc characterization after degradation in direct cell contact

4.2.1 Influence of cell type and cell density on degradation rate and osmolality

Figure 12a shows the relative degradation rates (DRs) for Mg discs seeded with different cell types and cell densities after six days of immersion with cells. The DRs differed cell type-, as well as cell density-dependently. While MMC treatment led to a significant degradation reduction compared to the cell-free control, untreated cells promoted Mg degradation or had no significant influence.

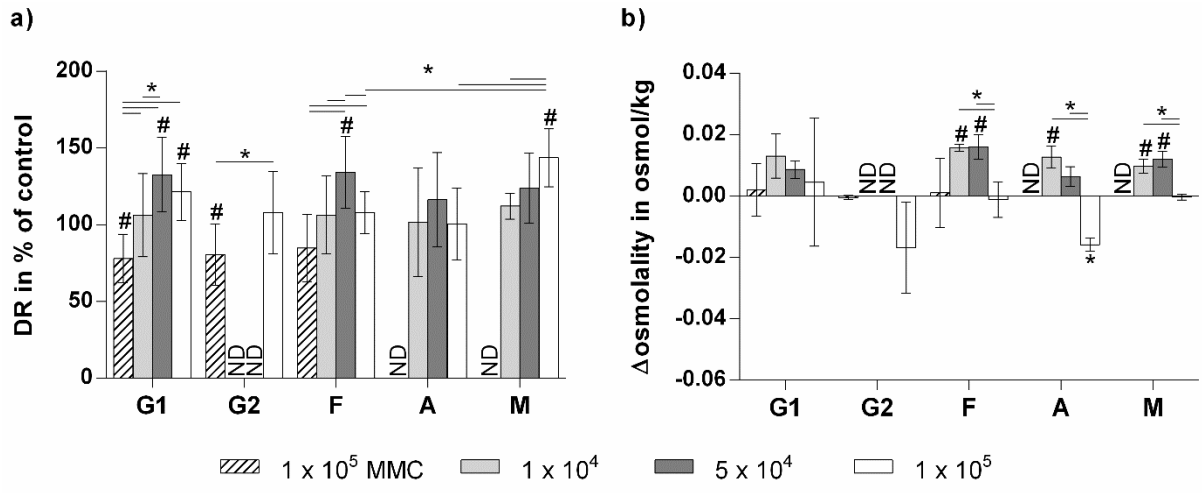

Figure 12 | Cell type and cell density-dependent degradation of Mg discs. a) DR in % of the control (cell-free Mg, 100 %) and **b)** Δosmolality of Mg seeded with LN229 (G1), A172 (G2), L929 fibroblasts (F), astrocytes (A) and HMC3 microglial cells (M) at different densities (untreated and MMC-treated) after six days of immersion. Values were calculated from three independent experiments with n=6 (DRs) or n=3 (Δosmolality) per experiment for each cell number and cell type. Statistically significant differences between cell densities and cell types were tested by **a)** two-way ANOVA and **b)** one-way ANOVA with Tukey's multiple comparisons post-hoc test and indicated by an asterisk or number sign. P-values of 0.05 or lower were considered statistically significant. Number signs indicate significant differences compared to control. ND = not determined. Results were partly published in [120].

An increase of the number of initially seeded cells from 10^4 to 5 x 10^4, enhanced Mg degradation continuously within the GBM, fibroblast, and microglia sample group. For microglial cells, the degradation was elevated even further when increasing the cell number to 10^5, whereas samples seeded with 10^5 L929 or LN229 showed less or no significant difference in degradation compared to samples seeded with 5 x 10^4 cells of the same cell type.

No significant impact of the cell amount on Mg degradation could be observed for samples seeded with astrocytes.

The comparison of samples seeded with 10^5 untreated cells among the different cell types revealed that samples cultured with HMC3 degraded most, followed by LN229 and then followed by L929, A172, and astrocytes. No statistically significant alterations between the cell type groups were evident for the remaining cell densities.

The influence of cells seeded on Mg on the supernatant osmolality after six days of immersion is depicted in Figure 12b. For changes in ∆osmolality after three days and cells seeded on TCP please compare Figure s1. Cell-seeding on Mg led to positive or near-zero ∆osmolality values for all cell types and cell densities except for samples seeded with 10^5 A172 or astrocytes. 10^4 L929, astrocytes, and HMC3 cells, as well as 5 x 10^4 L929, and HMC3 cells significantly increased ∆osmolality compared to the material control without cells ($\Delta osmolality_{control}$ = 0), whereas 10^5 astrocytes caused a significant decrease in ∆osmolality compared to the material control. Generally, ∆osmolality was highest for 10^4 cells seeded on Mg and decreased with growing cell density irrespective of the cell type.

4.2.2 Influence of cells on the degradation surface after immersion

After six days of immersion, the degradation surface morphology was analyzed for the material control (no cells), the sample groups with the highest (10^5 HMC3 and 10^5 LN229) and the lowest degradation (10^5 MMC-treated LN229) before and after degradation product removal with chromic acid. Representative images of this analysis are displayed in Figure 13. All samples exhibited cracked layers of degradation products before chromic acid treatment (probably resulting from the drying) without any distinct differences between the sample groups. After chromic acid treatment, the material control and samples seeded with 10^5 MMC-treated LN229 cells showed rough surfaces but no sign of pitting corrosion. Contrarily, fast degrading samples seeded with 10^5 LN229 and 10^5 HMC3 cells were densely covered with a significant number of corrosion pits.

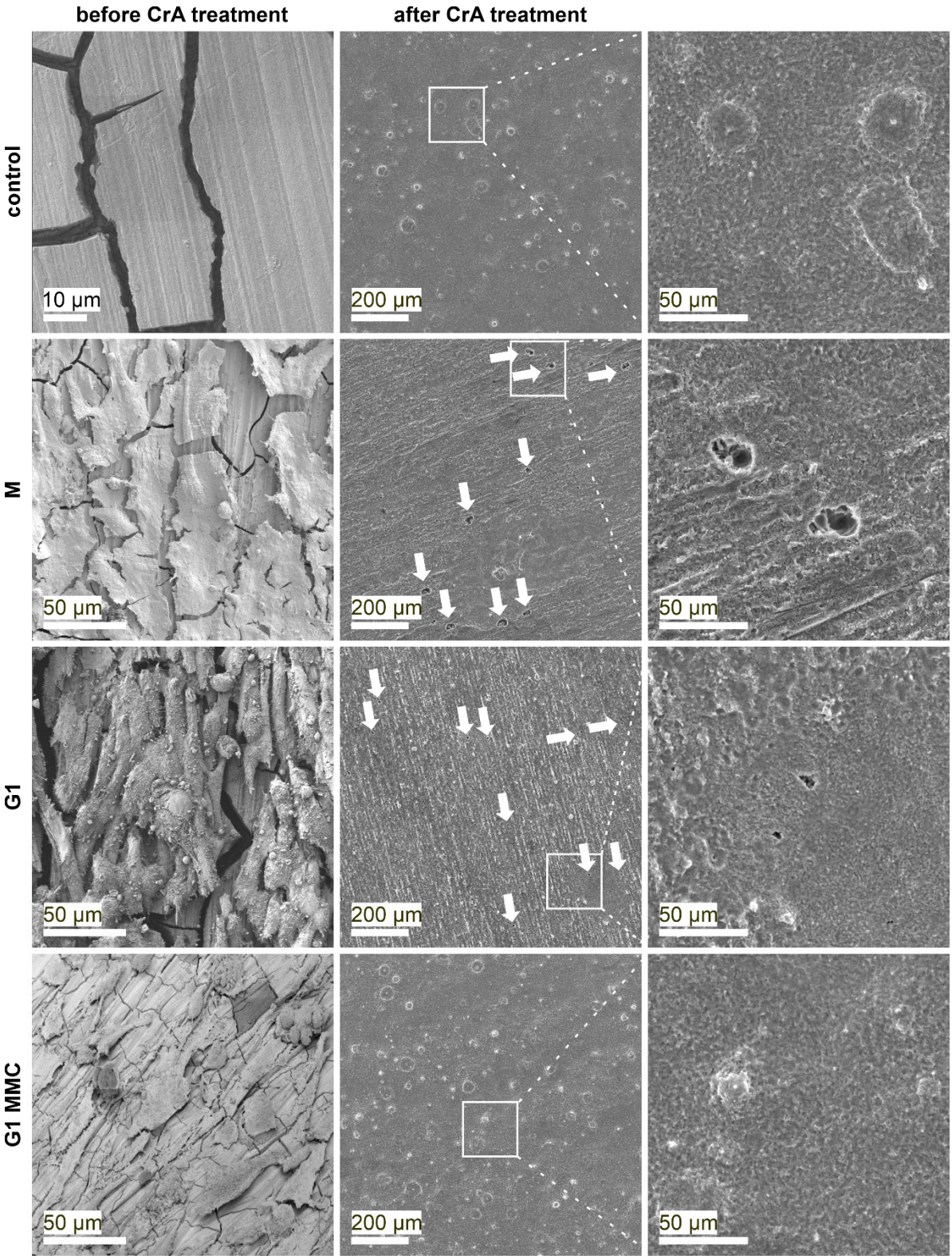

Figure 13 | Surface morphology of cell-seeded Mg discs after degradation. SEM images of cell-free Mg (control) and Mg seeded with 10^5 HMC3 (M), 10^5 LN229 (G1) and 10^5 MMC-treated LN229 (G1 MMC) after six days of immersion before and after degradation product removal with CrA. White arrows indicate degradation pits. Results were partly published in [120].

4.2.3 Influence of cell type on degradation layer thickness, morphology, and composition

The cross-section analysis of Mg seeded with 10^5 untreated, and MMC-treated cells is displayed in Figure 14. Thickness measurements of the degradation layer revealed considerably thinner layers for samples seeded with cells regardless of the cell type compared to the material control. However, degradation layers increased in thickness and porosity when samples were seeded with MMC-treated cells compared to untreated cells.

Analysis of the elemental distribution along the degradation layer from the surface to bulk material showed that the degradation layer predominantly consisted of Mg and lower contents of S, C, P, and Ca for all treated and untreated cells. As expected, Mg contents increased when approaching the bulk material, while the contents of all other elements decreased with growing distance from the layer surface. Striking differences in degradation layer composition compared to the other samples were observed for Mg seeded with astrocytes and MMC-treated cells. Astrocyte-seeded Mg exhibited higher contents in Ca, and P near the sample surface than all other samples. MMC treatment led to the formation of oxygen-rich degradation layers and slightly increased C contents at the sample surface.

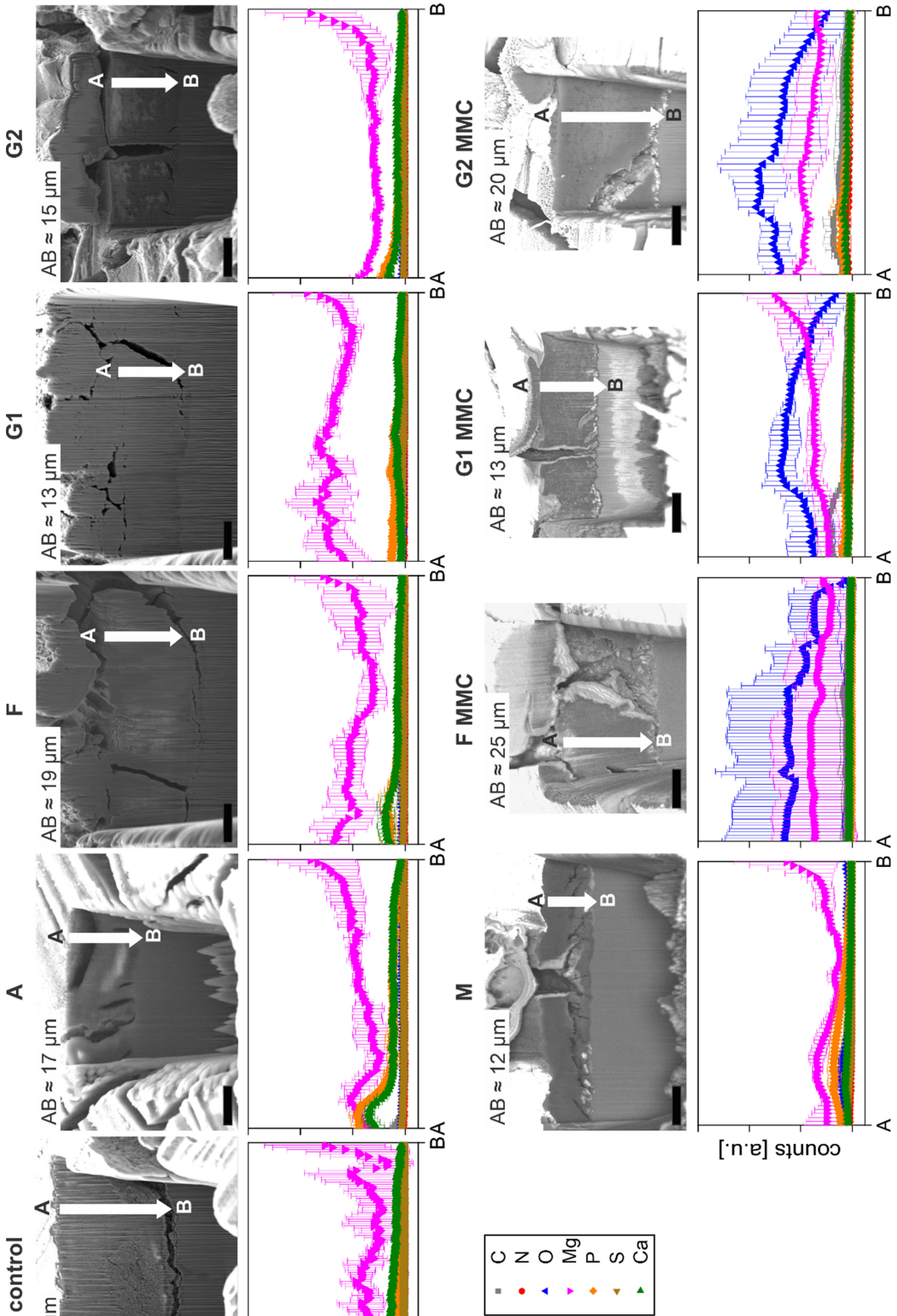

Figure 14 | Degradation layer thickness, morphology, and composition of cell-seeded Mg discs. SEM images and EDX line profiles of FIB-milled cross sections of Mg discs seeded without cells (control) and with 10^5 astrocytes (A), HMC3 (M), L929 fibroblasts (F), LN229 (G1), A172 (G2), and 10^5 MMC-treated LN229 (G1 MMC), A172 (G2 MMC) and L929 (F MMC) after six days of immersion. Scale bar is 10 µm.

Figure 15 provides an overview of the IR spectra obtained from Mg surfaces seeded with different cell types.

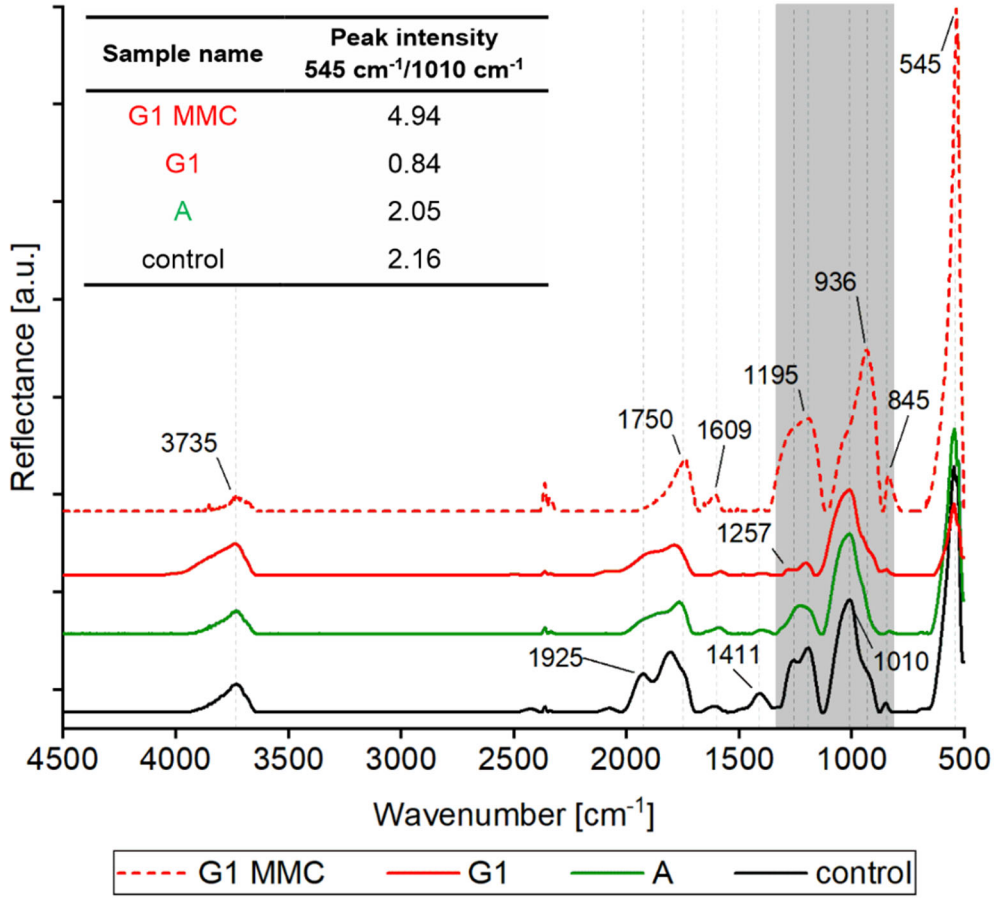

Figure 15 | Degradation layer surface composition of cell-seeded Mg discs. FTIR spectra obtained from Mg discs seeded with 10^5 LN229 (G1), astrocytes (A) and 10^5 MMC-treated LN229 (G1 MMC) after six days of immersion with the respective intensity ratio of the peaks at 545 and 1010 cm^{-1} for all samples.

All samples showed a distinctive band at 3735 cm^{-1}, which was assigned to the OH stretching vibration and indicated the presence of $Mg(OH)_2$ [67, 121, 122]. The band at 1750 cm^{-1} is characteristic for the carbonyl stretching vibration, most probably originating from adsorbed organic molecules or cells [123-125]. Phosphate-related bands appeared in the grey-colored area (1257 cm^{-1}, 1195 cm^{-1}, 1010 cm^{-1}, and 845 cm^{-1}) for all samples. These phosphate bands were likely to emerge due to a combination of phosphate-containing functional groups in nucleic acids (e.g., DNA and ribonucleic acid (RNA)) [126, 127] and magnesium phosphate formation [67, 128-130]. Additionally, stretching and/or bending vibrations of adsorbed organic molecules (mainly C-O and C-C stretching, OH bending from carbohydrates and nucleic acids) presumably also contributed to the bands in this wavenumber range [67, 124, 131, 132]. Furthermore, all samples exhibited minor bands at 1609 cm^{-1} and 1411 cm^{-1}, which were

associated with carboxylic stretching vibrations, or the symmetric stretching vibration of carbonate. The prominent band at 545 cm^{-1} related to Mg oxide or hydroxide vibrations [121, 122, 133, 134]. Overall, the IR spectra for different cells and treatments exhibited no significant difference in appearing bands. Yet, the intensity of the Mg oxide/hydroxide related bands (Table in Figure 15) for Mg seeded with MMC-treated LN229 was higher than for all other tested samples, indicating the formation of oxygen-rich degradation products as likewise observed in the cross-section analysis.

4.3 Analysis of cell-induced degradation mechanisms

4.3.1 Cell layer density

The staining of alive and dead cells on Mg six days post immersion is depicted in Figure 16. Dense layers of viable cells were observed for all cell types and treatments. Only minor amounts of dead cells were visible for all cell types. Supplementary images at higher magnification of the respective disc areas are provided in Figure s2. An increased number of initially seeded cells promoted higher cell layer densities, as expected. The cell layer of 10^5 L929 initially seeded cells had even grown to such a great extent, that a large proportion of cells detached during the process of staining, as can be seen especially at the sample edges. Moreover, an increasing cell layer thickness was accompanied by elevated gas bubble formation. This gas bubble formation was particularly pronounced for 10^5 LN229 and HMC3 cells, as well as for 5 x 10^4 L929 and HMC3 cells. MMC treatment diminished the cell layer thickness considerably in comparison to the respective control of 10^5 untreated cells, underlining the efficacy of the treatment.

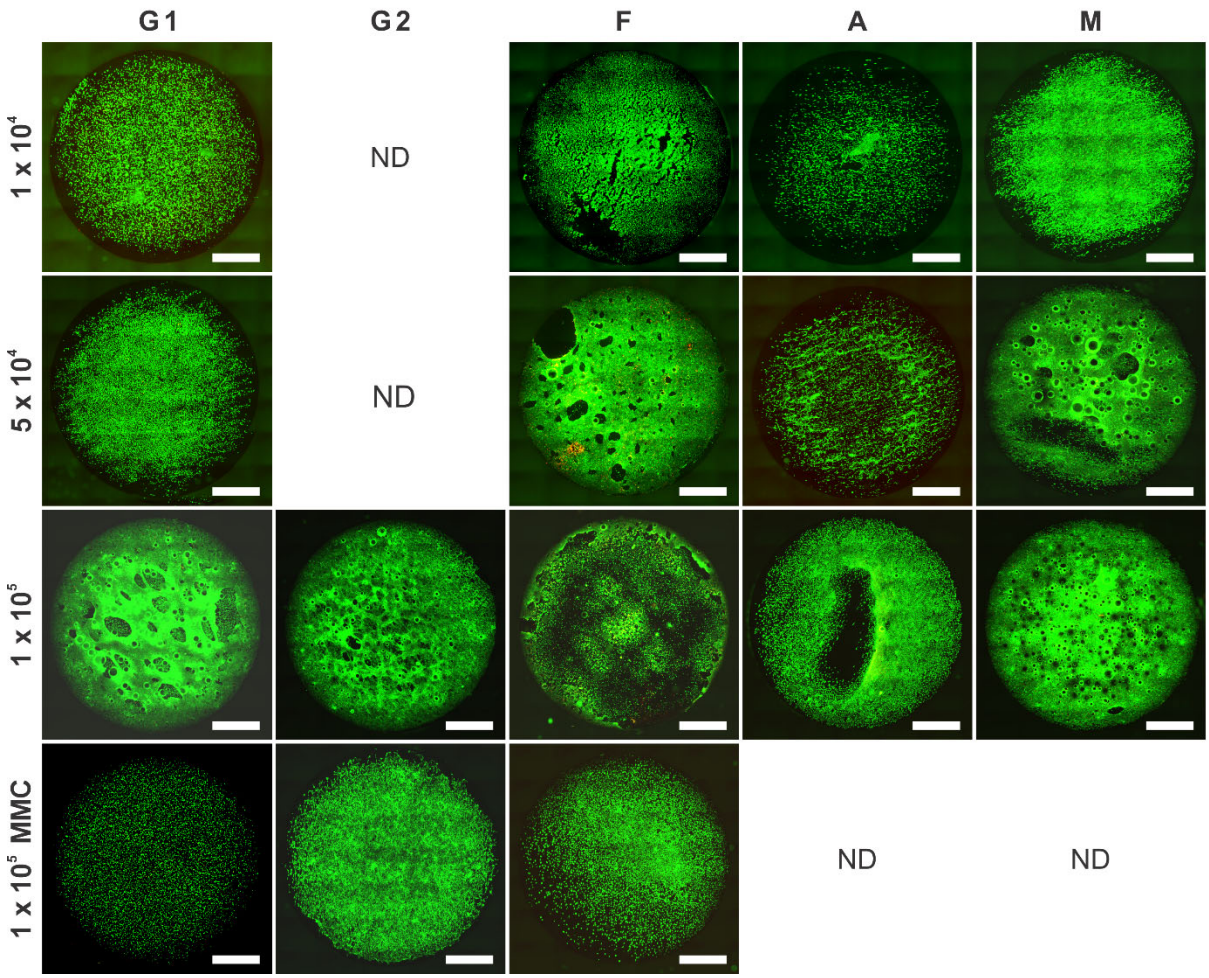

Figure 16 | Cell distribution and viability on Mg discs. Calcein/ethidium homodimer-1 staining of viable and dead LN229 (G1), A172 (G2), L929 (F), astrocytes (A) and HMC3 (M) cells after six days of culture on Mg discs at different cell densities (untreated and MMC-treated). Viable cells appear in green and dead cells in red. Scale bar is 2 mm. ND = not determined. Published in [120].

A cell morphology staining of all cell types on Mg and glass at a density of 1 x 10^5 cells (Figure 17) was conducted to illustrate the cell viability and cytocompatibility further. All untreated and MMC-treated cells adhered to both substrates in their expected, cell-specific morphologies. The change of substrate did not influence cell morphology for any of the analyzed cell types.

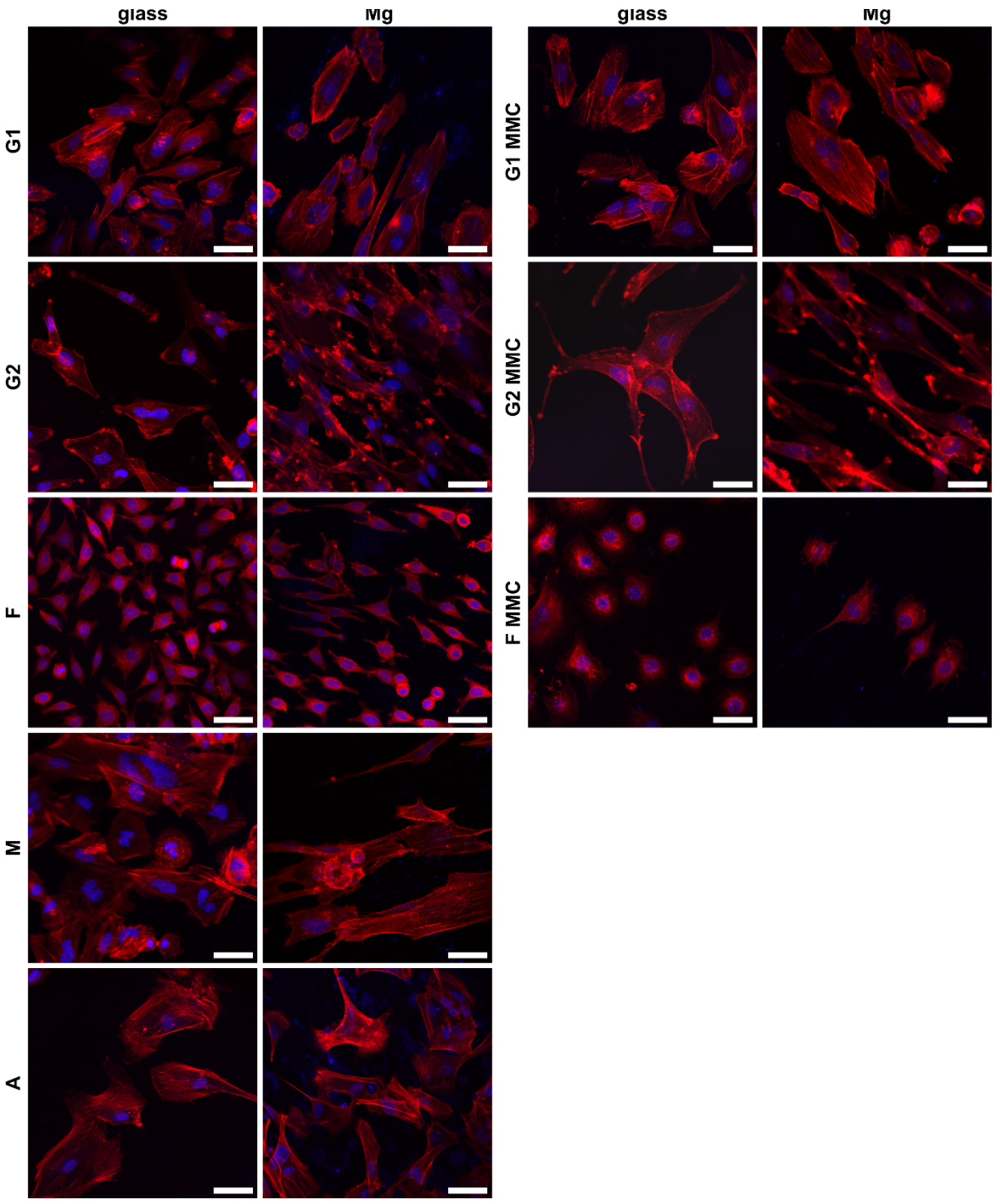

Figure 17 | Cell morphology on Mg discs and glass substrates. Actin staining of LN229 (G1), A172 (G2), L929 (F), HMC3 (M), astrocytes (A) and MMC-treated LN229 (G1 MMC), A172 (G2 MMC) and L929 (F MMC) cells on Mg discs and glass after six days of culture. F-actin appears in red; cell nuclei are counter-stained in blue. Scale bar is 50 µm. Results were published in [120].

The observations made during the viability staining were additionally quantified via DNA measurements. Figure 18 presents the absolute DNA content of 10^4, 10^5 untreated, and 10^5 MMC-treated cells on Mg after six days of culture. DNA contents increased continuously with an increasing number of initially seeded cells, supporting the cell staining results. Likewise, MMC treatment led to a significant reduction in DNA content compared to 10^5 untreated cells for all treated cell types.

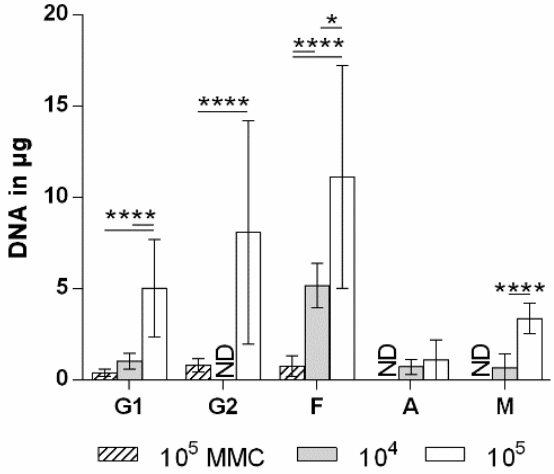

Figure 18 | **DNA quantification.** Absolute DNA content in µg of LN229 (G1), A172 (G2), L929 (F), astrocytes (A) and HMC3 (M) cells (untreated and MMC-treated) on Mg discs after six days of immersion for different cell densities. DNA values were calculated from three independent experiments with n=3 per experiment for each cell type and cell number. One-way ANOVA with Tukey's multiple comparisons post-hoc test was employed to determine statistical differences between cell densities (*p ≤0.05, **** p≤0.0001). ND = not determined. Results were published in [120].

4.3.2 Metabolite content

Absolute supernatant lactate levels of Mg seeded with cells six days post immersion are depicted in Figure 19. Samples seeded with 10^4 untreated cells exhibited lower lactate levels than samples seeded with 10^5 untreated cells for all cell types. The difference in lactate content between 10^4 and 10^5 cells of the same cell type was most distinctive for LN229 cells and least apparent for astrocytes. MMC treatment reduced the amount of supernatant lactate significantly compared to the respective control group of 10^5 untreated cells. Generally, lower lactate levels were detected for slow proliferating cells, such as astrocytes, while fast proliferating cell lines generated higher levels of extracellular lactate.

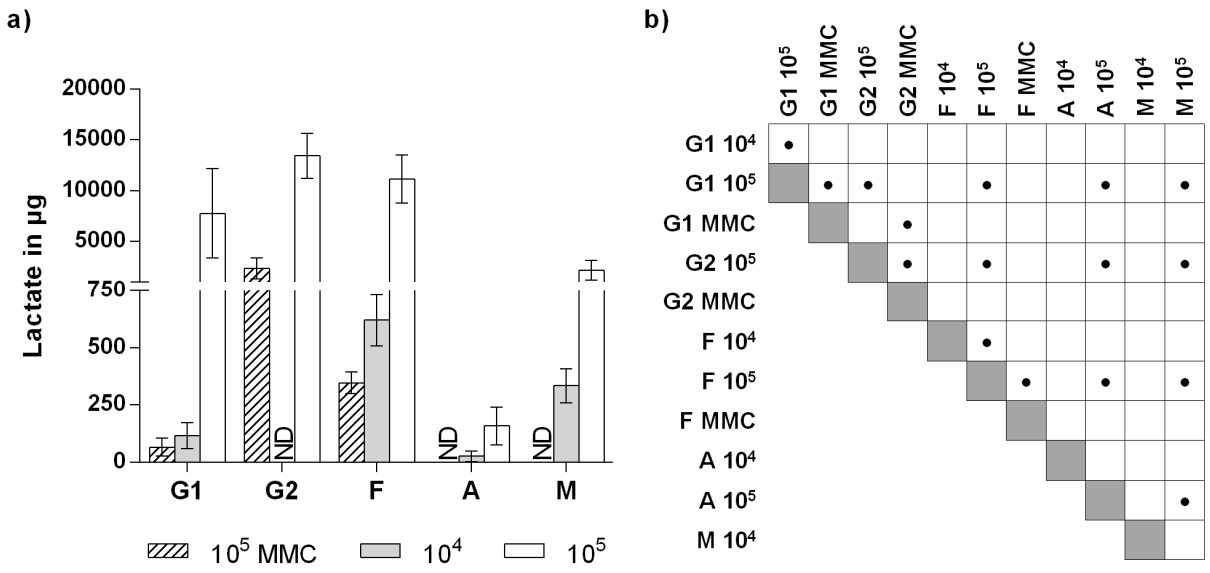

Figure 19 | **Metabolite quantification. a)** Supernatant lactate levels in µg for Mg seeded with untreated and treated LN229 (G1), A172 (G2), L929 (F), astrocytes (A) and HMC3 (M) cells at different seeding densities six days post immersion. Values were obtained from three independent experiments with n=3 per experiment for each condition. ND = not determined. **b)** Tukey's multiple comparisons post-hoc test (two-way ANOVA) for supernatant lactate contents. Dots indicate significant differences with a p-value of 0.05 or lower between cell densities and/or cell types. Results were published in [120].

4.3.3 Bulk pH

Figure 20 shows the ΔpH values for cells seeded on Mg (Figure 20a) and TCP (Figure 20b) after six days of culture. Additional data for ΔpH obtained on Mg and TCP after three days is given in Figure s3. ΔpH values for untreated L929 cells and astrocytes on Mg were positive or near-zero and showed no significant alteration for the different cell densities. Untreated HMC3 cells significantly reduced ΔpH values with an increasing number of initially seeded cells. A similar trend was observed for untreated LN229 cells. MMC-treated cells exhibited negative or near-zero ΔpH values. Compared to the cell-free material control ($\Delta pH_{control}$ = 0), 10^5 A172 and HMC3 caused a statistically significant reduction in ΔpH. 10^4 astrocytes, instead, led to a statistically significant increase in ΔpH. ΔpH values for 10^4 and 10^5 astrocytes on TCP were near-zero and did not differ from another. However, 10^5 astrocytes increased ΔpH compared to the lower cell densities, as well as compared to the cell-free control. Untreated L929 cells behaved similarly. As observed on Mg, untreated HMC3 and LN229 cells significantly reduced ΔpH with an increasing number of initially seeded cells. The magnitude of this pH change was even more pronounced on TCP than on Mg for both cell types. ΔpH for 10^5 A172 cells was

near-zero and did not differ from the cell-free control. MMC treatment caused negative ΔpH values.

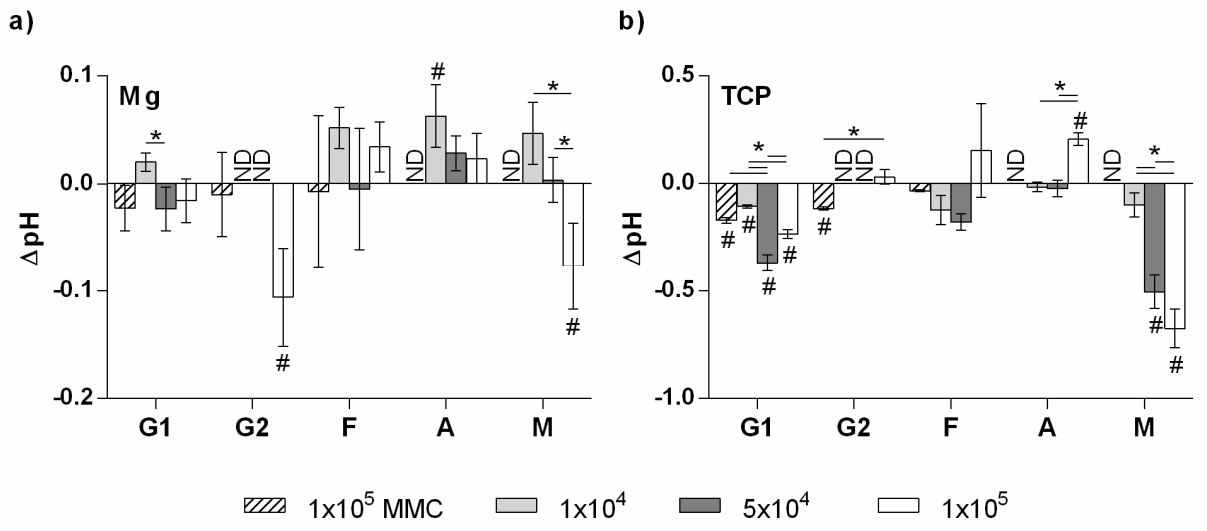

Figure 20 | Cell-induced changes in bulk pH. ΔpH of untreated and MMC-treated LN229 (G1), A172 (G2), L929 (F), astrocytes (A) and HMC3 (M) cells on **a)** Mg and **b)** TCP at different cell densities six days post immersion (n=3). Statistically significant differences between cell densities were determined using one-way ANOVA and indicated by an asterisk or number sign. P-values of 0.05 or lower were considered statistically significant. Number signs indicate significant differences compared to control ($\Delta pH_{control}$ = 0). ND = not determined. Results were partly published in [120].

4.3.4 Local pH

Figure 21a illustrates representative mappings of local pH evolution in serum-free DMEM on Mg under static and flow conditions (with and without cells) after 1.5 and 3 h of measurement. During static measurements, pH increased steadily over the entire scanned surface from an initial pH of 7.5 at the beginning of the measurement (top of map after 1.5 h) to a maximum pH of 8.2 after 3 h of measurement (bottom of map after 3 h). No distinct differences in pH were observed comparing the areas above Mg and epoxy resin. The observed pH increase followed the direction of the scanning pattern (lines from left to right, starting at the top and ending at the bottom). The observations made during static measurements relate to saturation processes [60]. Therefore, local pH changes cannot be resolved with this particular measuring set-up. Following, dynamic conditions were selected to study the cell-influence on local pH further. Under dynamic conditions (flow speed 0.66 mL/min) without cells, the Mg area was clearly distinguishable from the epoxy resin area by higher pH values. After 1.5 h, the area above Mg exhibited pH values from 7.4-8.15 (ΔpH = 0.75), whereas the surrounding DMEM

above epoxy resin showed pH values from 7-7.2. Similar values were observed after 3 h of measurement, yet the pH range above Mg decreased to 7.4-7.8 (ΔpH = 0.4).

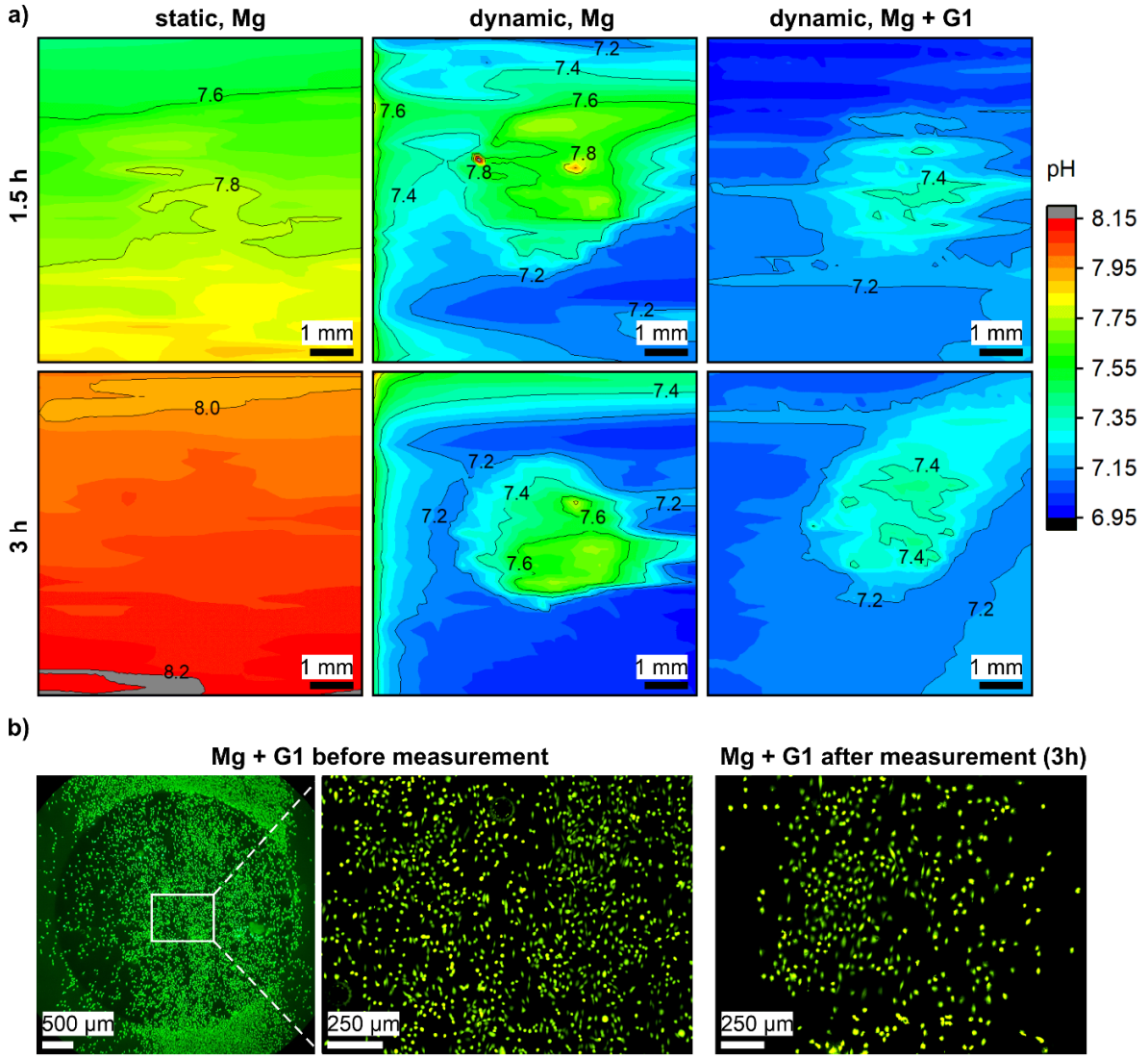

Figure 21 | **Local pH analysis on cell-seeded Mg. a)** Representative pH mappings of Mg without and with LN229 (G1) cells under static and hydrodynamic conditions (0.66 mL/min). **b)** Calcein staining before and after pH mapping.

Likewise, the local pH above Mg seeded with cells was increased compared to the surrounding medium above epoxy resin under dynamic conditions with cells, enabling a distinct identification of the Mg area after 1.5 and 3 h. In comparison to Mg without cells, the overall pH range above Mg was significantly smaller for Mg seeded with cells and varied from 7.3-7.4 (ΔpH = 0.1) and 7.2-7.45 (ΔpH = 0.25) after 1.5 and 3 h, respectively. Areas with high or low densities of cells (compare Figure 21b) did not lead to significant differences in local pH values.

The calcein staining revealed the cell distribution and viability before and after 3 h of measurement under flow conditions (Figure 21b). The cells were alive after the measurement, still a notable number of cells detached/died during the measurement time.

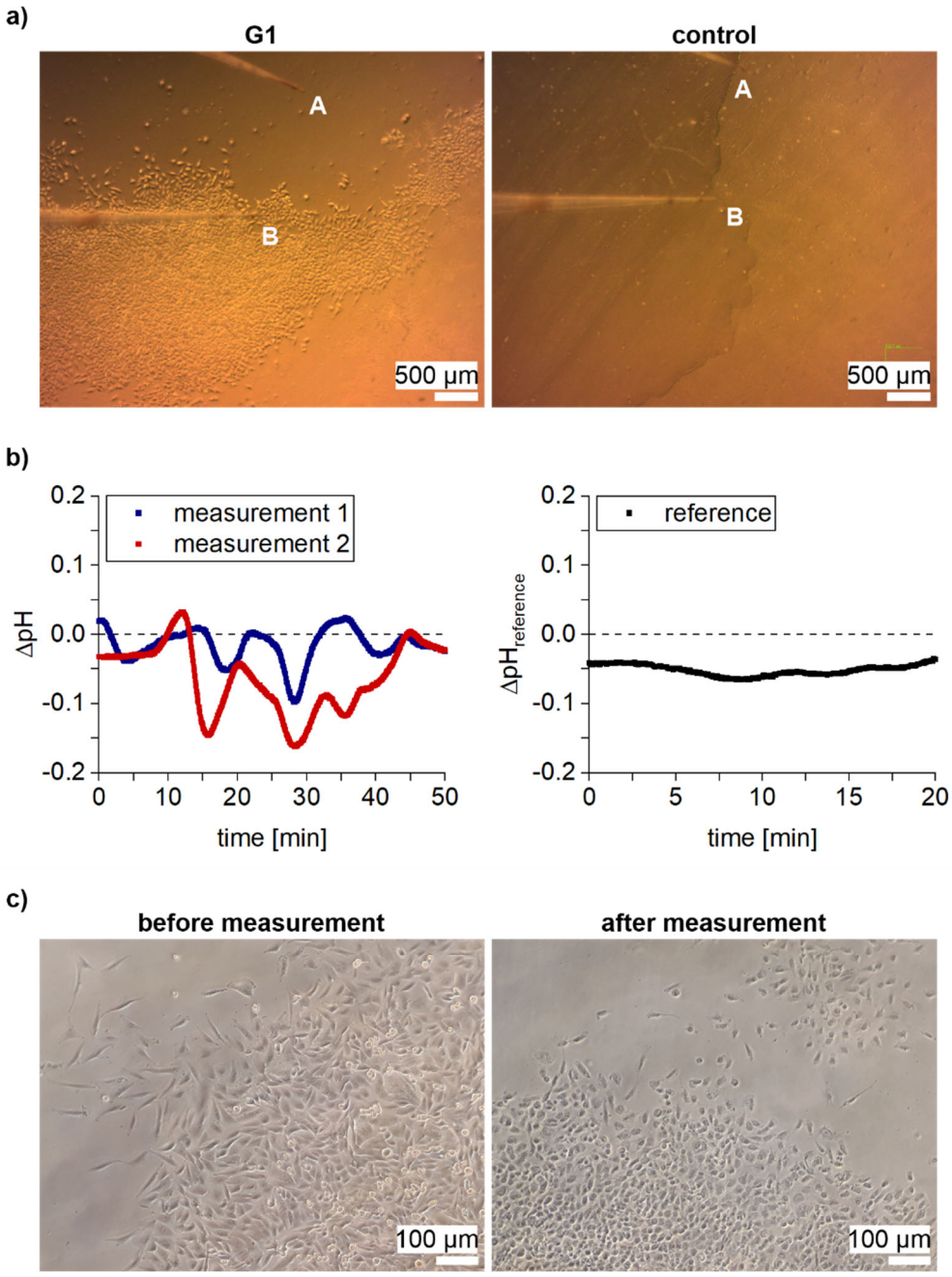

Figure 22 | Cell-induced local acidification on inert substrates. a) Electrode positions for the measurement with LN229 cells (left) and without cells (right). During the measurement with cells, probe B was positioned above cells and probe A was positioned above a cell-free area. **b)** ΔpH (difference between probe A and B considering the calibration error) development around cells for two representative measurements (left) and $\Delta pH_{reference}$ (calibration error between probe A and B) development (right). **c)** Cell appearance before and after the measurement obtained from optical microscopy.

Reference measurements of local pH around cells on inert substrates (TCP) were conducted to observe cell-related pH changes without the interference of degradation-induced pH changes. For this purpose, local pH was measured under static conditions using two independent electrodes (Figure 22a) positioned above cells (electrode B) and above a cell-free area (electrode A). The difference between the local pH above cells and next to cells, considering the error ($\Delta pH_{reference}$) caused by probe calibration and drift, is displayed in Figure 22b for two representative measurements. Both measurements show a reproducible, oscillating pattern of pH decrease caused by cells after ca. 15 min, 30 min and 35-40 min (ca. every 10-15 min). The calibration and drift error (Figure 22b right) between both probes remained constant at a mean ΔpH of ca. 0.05. Optical micrographs of LN229 cells before and after the measurement (to monitor cell viability during the measurement) are shown in Figure 22c. The cells remained viable after ca. 1 h of measurement, but appeared to be less firmly attached (less wide spread morphology).

4.3.5 Extracellular matrix composition and distribution

The supernatant arresten levels of 10^5 untreated LN229, A172, and L929, as well as 10^5 MMC-treated LN229, A172, and L929 were analyzed to determine differences in ECM composition for MMC-treated and untreated cells. The absolute supernatant arresten quantities measured are shown in Figure 23. The untreated tumor cell lines LN229 and A172 exhibited high levels of ca. 2927 and ca. 3193 pg arresten, respectively. MMC treatment of these cell lines caused a severe reduction in supernatant arresten levels to ca. 66 pg for LN229 and ca. 208 pg for A172. Supernatant arresten contents of L929 cells, however, remained unaffected by the MMC treatment.

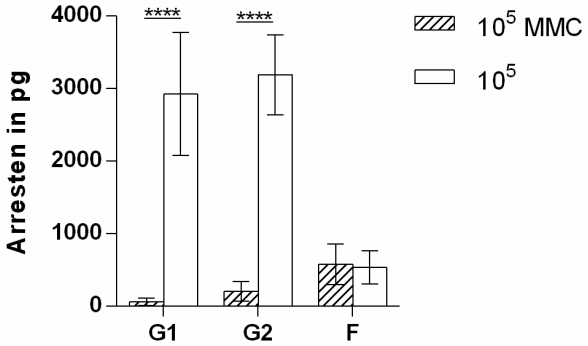

Figure 23 | **Indirect collagen type IV quantification.** Absolute supernatant arresten contents in pg for Mg seeded with 10^5 untreated and MMC-treated LN229 (G1), A172 (G2) and L929 (F) cells after six days of culture. Arresten values were calculated from three independent experiments with n=3 per experiment for each cell type and treatment. Mann-Whitney or t-test were employed to determine statistical differences between cell densities (**** p≤0.0001). ND = not determined.

The results of the ECM distribution analysis via fluorescence staining are illustrated in Figure 24-26. WGA-staining (Figure 24) revealed the occurrence of glcNAc for all cell types and cell densities, demonstrating the presence of HA for all analyzed samples. HA was found to be primarily located within the glycocalyx for all cell types. However, smaller proportions of HA outside the glycocalyx were additionally stained for all cell types (especially 10^5 astrocytes) apart from L929 fibroblasts. The SBA-staining (Figure 25) demonstrated the presence of galNAc/CS for all untreated cells, albeit only minor amounts of galNAc were stained for 10^4 and 10^5 L929 cells. For MMC-treated LN229 cells, galNAc/CS was virtually nonexistent. GAGs stained by SBA were mainly present within the glycocalyx for astrocyte-seeded samples. Large portions of collagen and elastin were stained for 10^4 and 10^5 LN229, L929, and HMC3 cells using the Col-F binding reagent (Figure 26), whereas for MMC-treated LN229 cells, or astrocytes less or little protein content was shown.

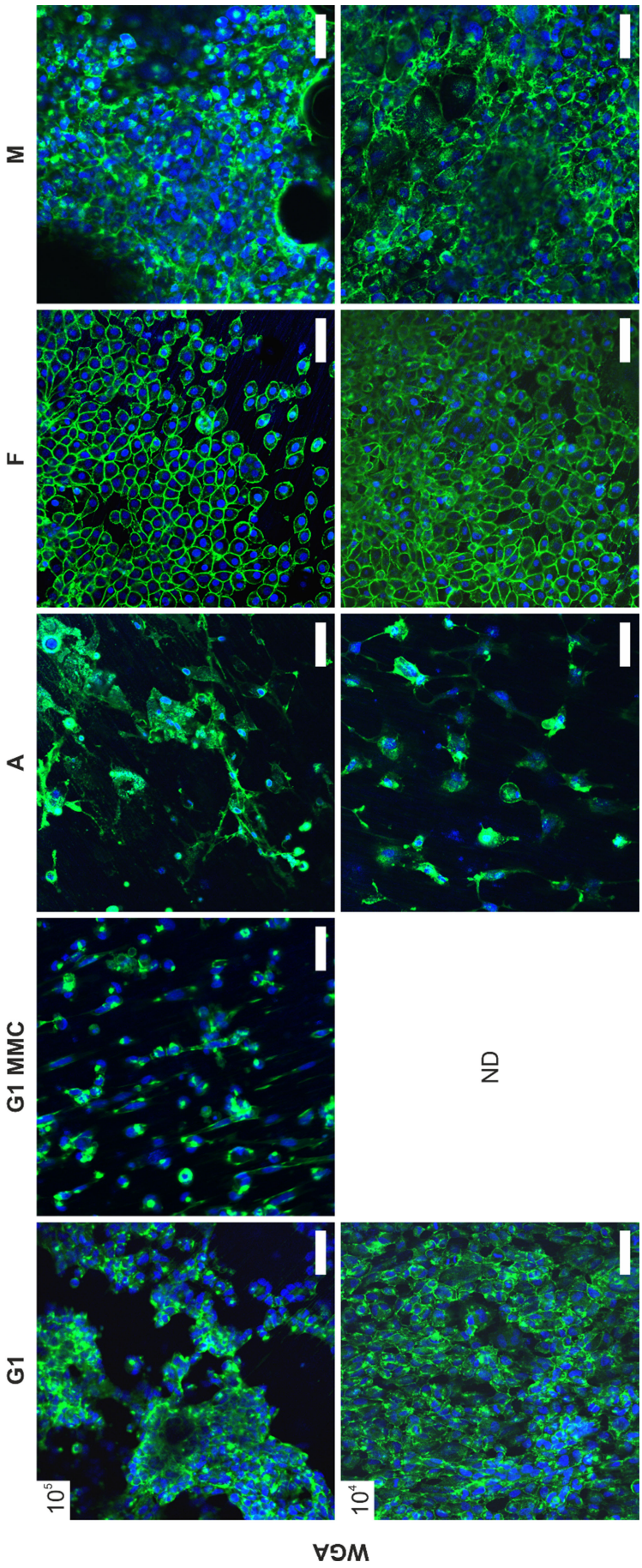

Figure 24 | Cell type- and cell density-dependent HA distribution. Fluorescence staining of WGA (green) on Mg seeded with 10^4 and 10^5 untreated LN229 (G1), astrocytes (A), HMC3 (M), L929 (F) cells and 10^5 MMC-treated L229 (G1 MMC) cells after six days of immersion. Cell nuclei were counter-stained in blue. Scale bar is 250 µm. ND = not determined. Parts of the results were published in [120].

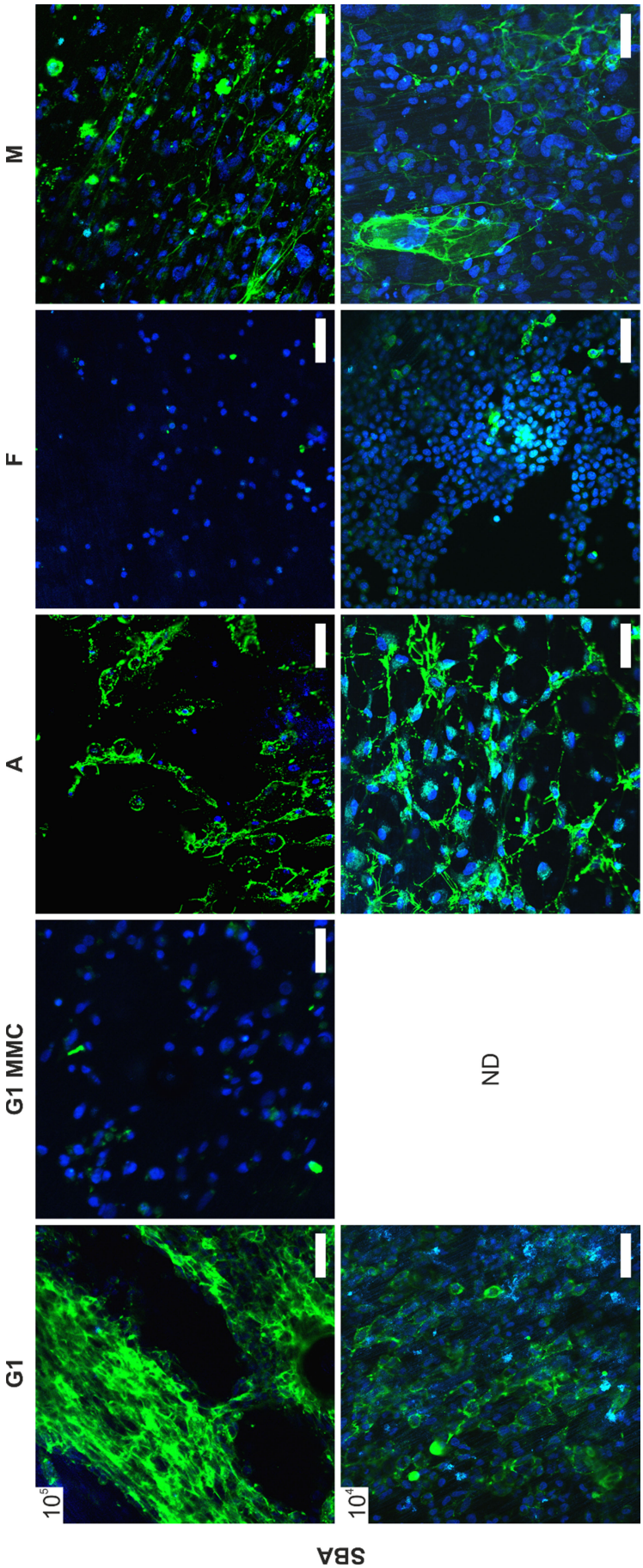

Figure 25 | Cell type- and cell density-dependent CS distribution. Fluorescence staining of SBA (green) on Mg seeded with 10^4 and 10^5 untreated LN229 (G1), astrocytes (A), HMC3 (M), L929 (F) cells and 10^5 MMC-treated L229 (G1 MMC) cells after six days of immersion. Cell nuclei were counter-stained in blue. Scale bar is 250 µm. ND = not determined. Parts of the results were published in [120].

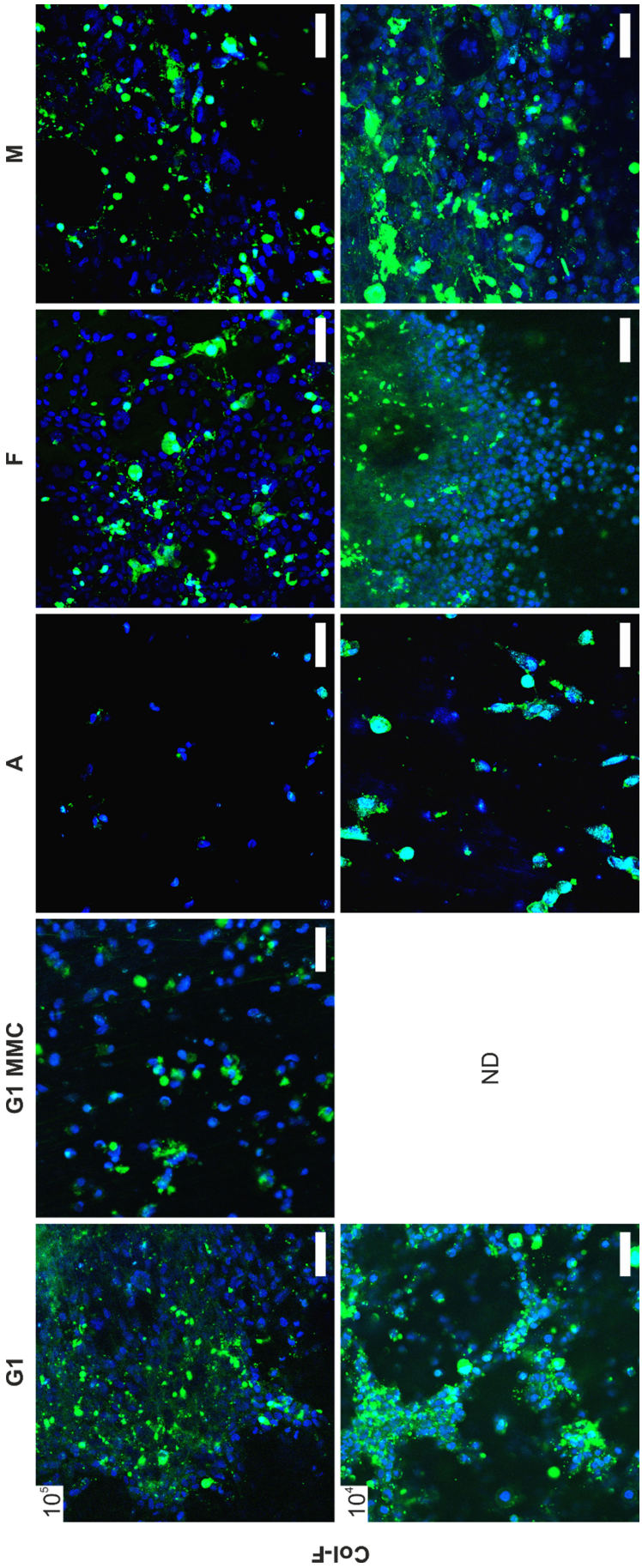

Figure 26 | Cell type- and cell density-dependent collagen/elastin distribution. Fluorescence staining of collagen/elastin (Col-F, green) on Mg seeded with 10^4 and 10^5 untreated LN229 (G1), astrocytes (A), HMC3 (M), L929 (F) cells and 10^5 MMC-treated L229 (G1 MMC) cells after six days of immersion. Cell nuclei were counter-stained in blue. Scale bar is 250 µm. ND = not determined. Parts of the results were published in [120].

Figure 27 summarizes the ECM compound amount/cell amount ratios for all conducted stainings on Mg. Significant differences were observed for LN229 and HMC3 cells when correlating the sample area stained in green (ECM compound) with the sample area stained in blue (cell nuclei) for the WGA-staining (Figure 27a). Reducing the number of initially seeded cells led to higher GAG/cell ratios for both cell types. By contrast, GAG/cell ratios for LN229 and HMC3 increased with a higher number of initially seeded cells for the SBA staining (Figure 27b). The GAG/cell ratios for astrocytes and L929 fibroblasts remained unaffected by the cell number for both WGA and SBA staining. While MMC treatment decreased the SBA/cell ratio compared to the untreated LN229 sample group, it did not impact the WGA/cell ratio. The protein/cell ratios obtained from Col-F staining (Figure 27c) were larger for 10^5 HMC3 cells than for 10^4 cells. No statistically significant cell density-dependent differences were evident for the remaining cell types. Nonetheless, a trend towards elevated protein/cell ratios for lower cell numbers was perceptible.

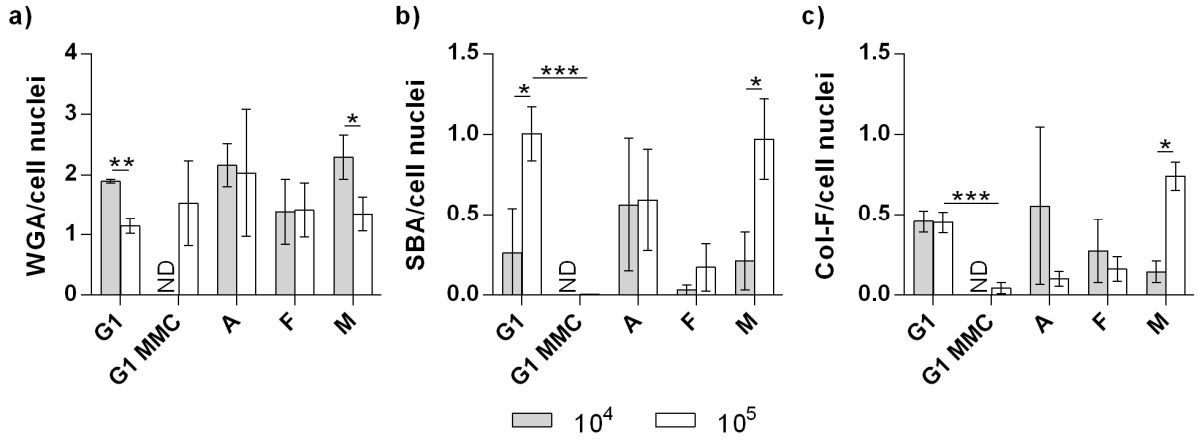

Figure 27 | Quantification of cell type- and cell density-dependent ECM composition. a)-c) Ratios of sample area stained in green (WGA, SBA, Col-F) to area stained in blue (cell nuclei) for Mg seeded with 10^4 and 10^5 cells analyzed using Image J software (n=3). Statistical analysis was performed by unpaired t-test (* p≤0.05, ** p≤0.01, *** p≤0.001). ND = not determined. Results were published in [120].

4.3.6 Influence of extracellular matrix molecules on degradation product formation

The impact of selected ECM molecules in aqueous solution on Mg degradation rate, pH change, and osmolality change is plotted in Figure 28. The addition of HA did not affect the DR of Mg (Figure 28a) for both medium groups (unadjusted pH and pH adjusted to 6.5). CS enhanced Mg degradation in water without pH adjustment but did not alter Mg degradation when adjusting the initial pH to 6.5. Collagen type IV (Figure 28b) significantly decreased Mg degradation. Yet, the kind of collagen type IV addition (coating or immersion) did not alter the degradation outcome.

After three days of immersion in the ECM compound-containing solutions without pH adjustment, ΔpH increased for HA and CS (Figure 28c) compared to the control (Mg in water). In contrast, the immersion of Mg in pH-adjusted solutions induced lower pH changes for HA and CS compared to the control (Mg in water), as well as in comparison to the respective solution without pH adjustment. The ΔpH difference between the solutions containing the same compound with and without pH adjustment, was more obvious for 0.05 M CS than for for 0.01 M HA. The addition of collagen type IV did not affect ΔpH compared to the respective control, irrespective of the type of addition (coating or immersion). The pH changes after six days (Figure 28d) of immersion were almost identical to the observations made at day three for all compounds.

When comparing Δosmolality (Figure 28e-f) of Mg immersed in compound-containing solutions with Δosmolality of Mg immersed in water only, statistically significant differences were observed only for collagen type IV three days post immersion. After six days of immersion (Figure 28f), the addition of CS as well as the coating with collagen type IV increased Δosmolality compared to the control (Mg in water). The immersion of Mg in HA- or collagen type IV-containing solutions either did not alter, or decreased Δosmolality compared to the control, respectively. pH adjustment had no significant influence on Δosmolality compared to the respective unadjusted sample group.

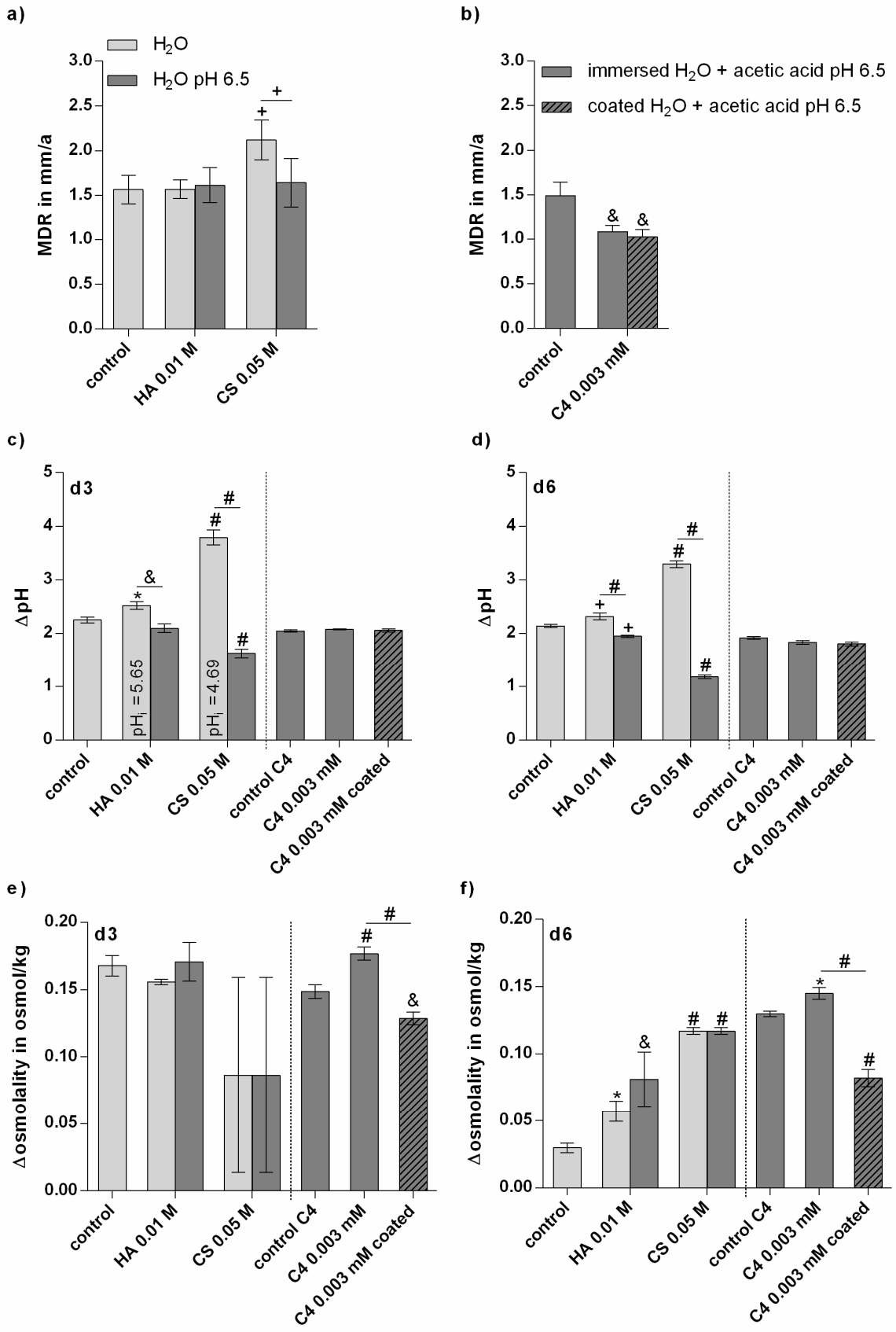

Figure 28 | Impact of selected ECM molecules on Mg disc degradation. a) and **b)** DRs of Mg immersed in water, HA, CS and collagen type IV (C4) with and without adjusted pH after

six days (n=6). **c)** Respective ΔpH values after three and **d)** six days of immersion (n=3). **e)** Respective Δosmolality values after three and **f)** six days of immersion. Two-way ANOVA or one-way ANOVA with Tukey's multiple comparisons post-hoc test were employed to determine statistical differences between the treatment conditions (* p≤0.05, + p≤0.01, & p≤0.001, and # p≤0.0001).

The chemical interaction of thin Mg layers with selected ECM molecules was studied employing *in situ* ATR-FTIR analysis and is shown in Figure 29. The interaction of Mg with distilled water only (Figure 29a) was observed as a reference, since all tested ECM compounds were dissolved in distilled water. Upon contact of Mg with water, distinctive bands appeared at 3706 cm^{-1}, 3429 cm^{-1}, 1646 cm^{-1}, 1035 cm^{-1} and 662 cm^{-1} These bands were associated with $Mg(OH)_2$, stretching and bending modes of – OH, as well as vibrational modes of Mg-O [121, 129, 132], respectively, indicating the formation of a $Mg(OH)_2$/MgO layer due to surface hydroxylation. Additional bands at 1480 cm^{-1} and 1387 cm^{-1} additionally suggested the formation surfaces carbonates resulting from the presence of atmospheric CO_2 [122, 128]. With proceeding immersion time, the intensity of all bands decreased continuously, indicating the dissolution and instability of the $Mg(OH)_2$/MgO film.

Figure 29b presents the data obtained from immersion of Mg with HA. The IR spectrum presented in green refers to the measurement of HA in absence of Mg. During the reference/blank measurement of HA, two main bands appeared at 1606 cm^{-1} and 1410 cm^{-1}, corresponding to the symmetric and asymmetric stretching of the carboxylic group [135]. The wavenumber position of these vibrations underlines the deprotonated state of HA under the testing conditions [135]. During the immersion of Mg with HA, bands at 3704 cm^{-1}, 3450 cm^{-1}, 1068 cm^{-1} and 676 cm^{-1} appeared. The appearing bands were assigned to $Mg(OH)_2$/MgO, as well as - OH stretching and bending modes [121, 129, 132]. Similarly to the reaction in water only, the immersion in HA led to the formation of a $Mg(OH)_2$/MgO layer which was instable and dissolved over time (decreasing band intensity). Yet, the strong and distinctive bands at 1640 cm^{-1} and 1410 cm^{-1} (- COOH stretching modes) underlined the chemical interaction of Mg and HA through its functional groups [135].

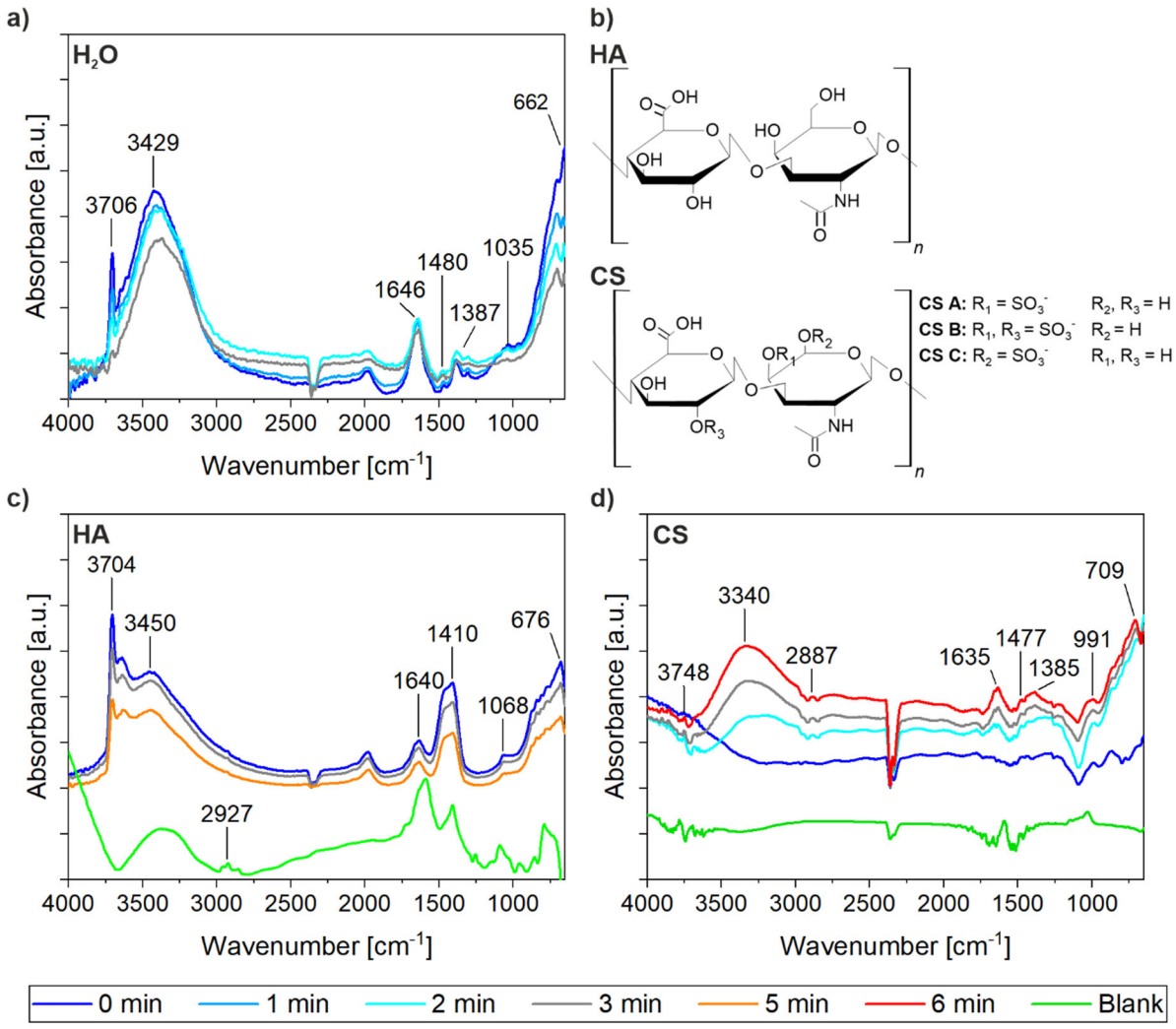

Figure 29 | Chemical interaction of ECM molecules with Mg substrates. a) ATR-FTIR spectra of Mg immersed in water. **b)** Chemical structure of HA and CS. **c)** ATR-FTIR spectra of Mg immersed with HA and **d)** CS.

The interaction of Mg and CS is shown in Figure 29c. During the blank measurement (CS without Mg), bands emerged at 1635 cm^{-1}, 1477 cm^{-1} and 1010 cm^{-1}, associated with the functional groups of CS (carboxylic group and sulfate group). The immersion of Mg in CS gave rise to a minor band at 3700 cm^{-1} and additional bands at 3340 cm^{-1}, 1635 cm^{-1} and 709 cm^{-1}, corresponding to the interaction with H_2O and the formation of a thin $Mg(OH)_2$/MgO film [121, 129]. Additional bands appeared at 2287 cm^{-1}, 1477 cm^{-1}, 1385 cm^{-1} and 991 cm^{-1}. These bands were assigned to the C-H stretching vibration of adjacent alkyl groups, symmetric and asymmetric stretching vibrations of the carboxylic group, and symmetric stretching vibrations of the sulfate groups [135, 136]. Furthermore, a negative band at 1089 cm^{-1} appeared upon immersion with HA, referring to the breakdown of the $Mg(OH)_2$ layer [135]. The intensity of appearing bands increased over time, indicating ongoing chemisorption of CS on the Mg surface through its functional groups.

4.4 *In vitro* degradation of Mg-based thin films

4.4.1 Mg-based thin film stability under *in vitro* conditions and cell influence on degradation

The thin film stability and *in vitro* degradation was analyzed for pure Mg and Mg-6Ag thin films. The results for both film types are presented separately hereinafter.

Pure Mg thin films

Figure 30a shows the DRs of two different batches of pure Mg thin films after three days of immersion with and without cells. The DRs of the material controls of both batches did not differ significantly from one another, indicating the reproducibility of the fabrication process. Furthermore, the DR of both material batches were slightly higher than the DR of pure Mg discs. Nevertheless, the DRs of both batches were in a range (ca. 0.4 mm/a) that is suitable for *in vitro* testing. Cell seeding had no significant influence on the DR.

∆pH and ∆osmolality (Figure 30c-d) exhibited positive values for all sample groups as a result of increasing degradation. No statistically significant differences in ∆pH values were observed when comparing cell-free and cell-seeded samples. ∆osmolality values, however, were significantly lower for astrocytes and HMC3-seeded samples compared to the cell-free control.

The optical appearance of Mg thin films before and after immersion is depicted in Figure 30d. Films were shiny and minimally curled before degradation. After degradation and chromic acid treatment, all films of both batches were still almost entirely intact with only a few degradation-induced irregularities at the sample edges. Despite the use of inserts to prevent film bending, all tested thin films curled up. This bending/curling was more severe for the faster degrading batch 20-05/20-**06**.

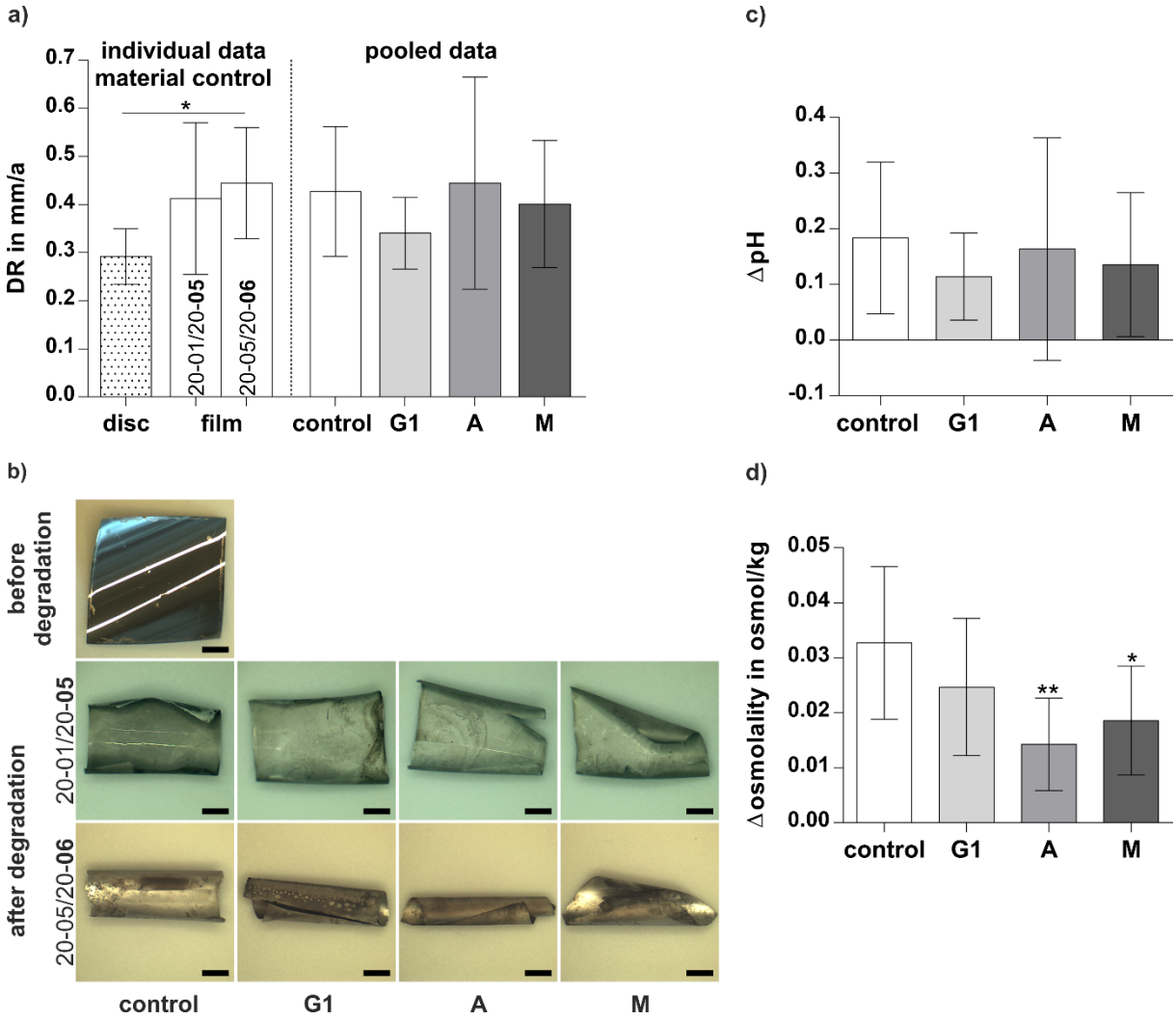

Figure 30 | ***In vitro*** **degradation of pure Mg thin films. a)** DRs of two pure Mg thin film batches without and seeded with 10^5 LN229 (G1), astrocytes (A) and HMC3 (M) cells after three days of immersion. **b)** Optical appearance of the thin films before and after degradation. Scale bar is 2 mm. **c)** ΔpH and **d)** Δosmolality values. One-way ANOVA with Tukey's multiple comparisons post-hoc test or Kruskal-Wallis test with Dunn's multiple comparisons post-hoc test were performed to determine statistically significant differences between material batches or groups (* $p<0.05$ and ** $p\leq0.01$).

Mg-6Ag thin films

The DRs of Mg-6Ag thin films after three days of immersion with and without films for three different material batches are displayed in Figure 31a. All three material batches exhibited comparable DRs (ca. 0.8 mm/a). However, the DRs for thin films were significantly higher than for the extruded Mg discs. Seeding of 10^5 LN229, HMC3 cells, or astrocytes did not influence the DR significantly.

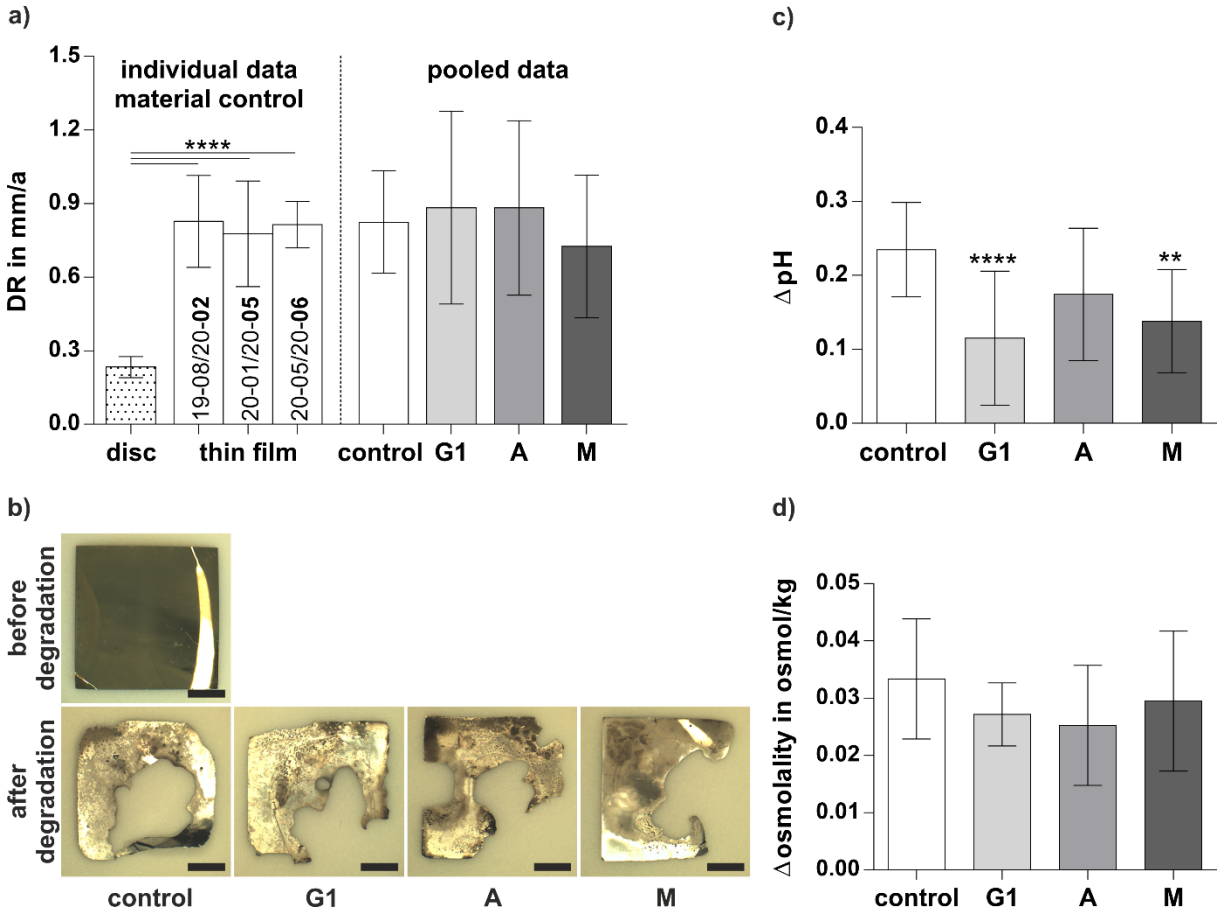

Figure 31 | *In vitro* degradation of Mg-6Ag thin films. a) DRs of three different Mg-6Ag thin film batches (individual data) immersed without cells and seeded with 10^5 LN229 (G1), astrocytes (A) and HMC3 (M) (pooled data) after three days of immersion. **b)** Optical thin film appearance before and after immersion with and without cells. **c)** Respective ΔpH and **d)** Δosmolality values. One-way ANOVA with Tukey's multiple comparisons post-hoc test or Kruskal-Wallis test with Dunn's multiple comparisons post-hoc test were performed to determine statistically significant differences between material batches or cell types (** p≤0.01, *** p≤0.001, and **** p≤0.0001).

Figure 31b illustrates the thin film appearance before and after degradation. Before degradation, Mg-6Ag thin films were flat and shiny. Immersion in medium for three days lead to a notable loss of thin film integrity for all samples groups (with and without cells). Material loss occurred at local spots and expanded approximately circularly from the spot of origin.

ΔpH and Δosmolality values were positive for all tested samples, underlining ongoing degradation (Figure 31c-d). Seeding with LN229 or HMC3 cells lead to a significant decrease in ΔpH compared to the material control, whereas seeding with astrocytes did not alter ΔpH. In contrast, cell-seeding had no significant influence on Δosmolality.

4.4.2 Cytocompatibility of Mg-based thin films

The cell viability staining of LN229, HMC3 cells and astrocytes demonstrated a significant number of viable cells on the pure Mg thin films for all analyzed cell types (Figure 32). No dead cells were evident on the analyzed material.

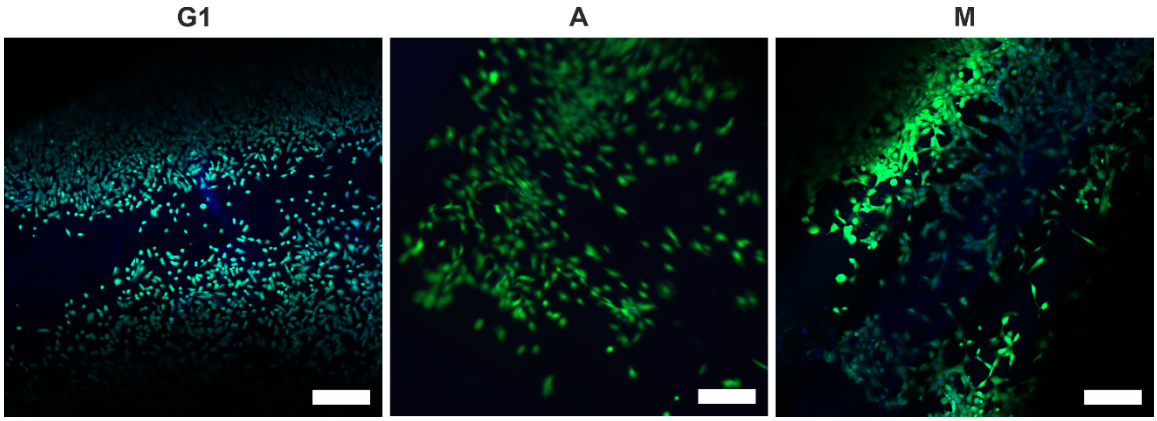

Figure 32 | Viability of neural cells on pure Mg thin films. Calcein/ethidium homodimer-1 staining of viable (green) and dead (red) LN229 (G1), astrocytes (A), and HMC3 (M) cells on Mg thin films three days after cell seeding. Nuclei were counter-stained in blue. Scale bar is 100 µm.

Figure 33 shows the cell viability staining of LN229, HMC3 cells and astrocytes in direct material contact with Mg-6Ag thin films after three days. All cell types formed dense layers of viable cells on the material surface, suggesting a general cytocompatibility of the material. No dead cells were evident on the analyzed material. While HMC3 cells and astrocytes adhered wide spread, LN229 cells appeared to attach rather spherically to the Mg-6Ag thin film surface.

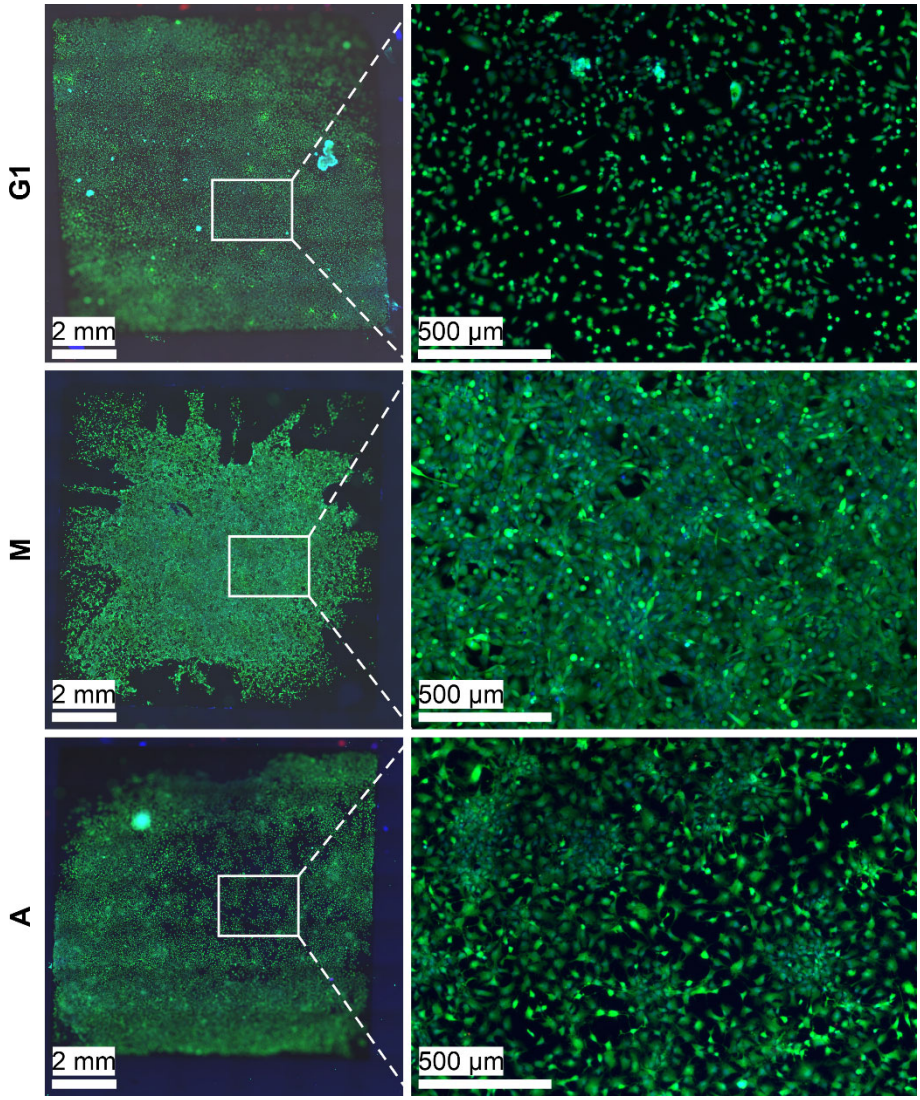

Figure 33 | Viability of neural cells on slow-degrading Mg-6Ag thin films. Calcein/ethidium homodimer-1 staining of viable (green) and dead (red) LN229 (G1), astrocytes (A), and HMC3 (M) cells on slow-degrading Mg-6Ag thin films (DR≈0.8 mm/a) three days after cell seeding. Nuclei were counter-stained in blue.

The comparison of the cell-specific morphologies on Mg-6Ag thin films and glass (Figure 34) underlined the observations made during the cell viability staining further. Astrocytes and HMC3 cells adhered to both substrates in their cell-specific morphology, whereas LN229 cells adhered to Mg-6Ag less wide spread than to glass.

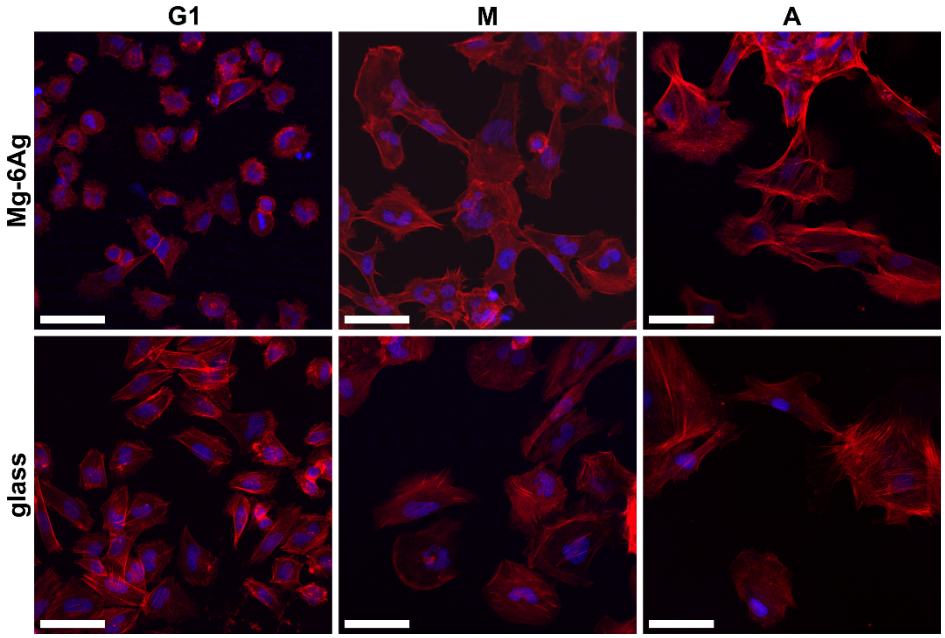

Figure 34 | Morphology of neural cells on slow-degrading Mg-6Ag thin films. F-actin (red) and nuclei staining (blue) of LN229 (G1), HMC3 (M) cells and astrocytes (A) on slow-degrading Mg-6Ag thin films (DR≈0.8 mm/a) and glass after three days. Scale bar is 250 µm.

The results obtained from cytotoxicity analysis in indirect material contact are shown in Figure 35. The cell viability decreased significantly for all cell types compared to the respective control when adding Mg-6Ag thin films. However, healthy cell types showed a trend towards lower susceptibility than tumor cells. ΔpH and Δosmolality values were comparable for all sample groups with Mg-6Ag thin film addition, confirming that the material degradation was constant for all sample groups.

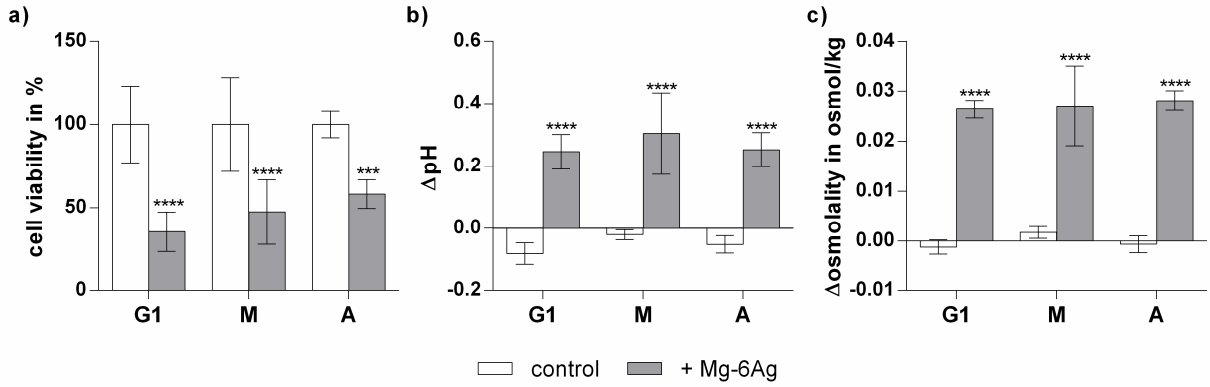

Figure 35 | Cytotoxicity analysis of fast-degrading Mg-6Ag thin films. a) Cell viability of LN229 (G1), HMC3 (M) and astrocytes (A) after 24 h of indirect contact with fast-degrading Mg-6Ag thin films (DR>1.5 mm/a). **b)** Respective ΔpH and **c)** Δosmolality values. Statistical analysis was performed using two-way ANOVA (*** p≤0.001 and **** p≤0.0001).

5 Discussion

5.1 Influence of different neural cell types on the degradation rate of pure Mg discs in direct contact

Mg-based neural implants may be applicable for a diverse number of medical conditions. Therefore, different types of brain cells, either serving different functions within the CNS or representing different pathologies, were selected in this study to obtain a broad overview of the cellular influence on Mg degradation. The analysis of the influence of different types and densities of neural cells on the degradation of pure Mg discs revealed that the selected brain cells caused either degradation inhibition or degradation promotion. The exact degradation outcome was dependent on the cell type and its proliferative activity (slow-proliferating versus fast-proliferating). Additionally, the initial cell number seeded on top of the material had a crucial influence (increased degradation with an increased cell number) on the Mg degradation.

A high dependence of the degradation of Mg-based materials on cell type and cell number has previously been reported, mainly for cells relevant in orthopedic and cardiovascular applications [72-78]. Degradation promotion was observed for fibroblasts, osteosarcoma cells (SaOS-2) and macrophages in direct contact with Mg-based alloys by Kannan et al. [72], Witecka et al. [73], and Zhang et al. [74], respectively. In contrast, studies performed with preosteoblasts, HeLa, endothelial and osteosarcoma cells (MG63) [75-78] demonstrated degradation inhibition for Mg alloys and pure Mg. In the aforementioned *in vitro* studies, degradation promotion was related to pH reduction as a result of the cell metabolism [72, 73] and oxidation by reactive oxygen species (ROS) generated by cells [74]. While degradation inhibition was explained by the formation of a passivating cell layer [75, 76] and the formation of a more stable degradation layer due to the incorporation of Ca and P ions released by cells [77, 78]. The diversity of these findings underlines the vast complexity of cell-material interactions, which may explain underlying degradation mechanisms, once more. A selection of conceivable cell-material interactions relevant for neural cells was classified in passive and active cell influences and is listed in Table 8. In this thesis, most of these interactions were investigated to elucidate the detailed degradation mechanisms and will be discussed hereinafter.

Table 8 | List of conceivable neural cell-material interactions relevant for Mg degradation. Degradation promoting effects are displayed in red, degradation reducing effects are shown in green.

Passive cell influences	Active cell influences
▪ Formation of a dense layer of cells and ECM i. Inhibition of material-medium contact ii. Hindered diffusion of degradation promoting ions from below the cell layer causing pitting/crevice corrosion	▪ Metabolism i. Local pH reduction ii. Material oxidation by ROS iii. Chemical equilibrium shift of Mg dissolution reaction due to Mg^{2+} uptake by cells ▪ Chemical interaction of ECM molecules secreted by cells with Mg i. Formation of stable degradation products ii. Formation of instable degradation products iii. Binding of Mg^{2+} to ECM products (e.g., proteins) causing a chemical equilibrium shift ▪ Phagocytosis i. Chemical equilibrium shift of the Mg dissolution reaction due to ingestion of Mg particles by microglial cells

5.2 Passive cell influences on Mg degradation

For all analyzed samples, the formation of a dense layer consisting of cells and ECM (Figure 16 live/dead staining, Figure 24-26 ECM staining) was observed on top of the material surface, irrespective of the cell type, cell density or treatment. The density of this layer increased with an increasing amount of cells present on the material from MMC-treated cells to 10^5 untreated cells (Figure 18 DNA quantification). Previously, such a dense layer of cells has been associated with degradation inhibition in some studies [75, 76]. Seuss et al. [75] showed that dense layers of HeLa cells on AZ91D could increase the impedance compared to the cell-free control within the first hours of cell-seeding. Moreover, they observed even higher degradation inhibition when enhancing the cell seeding density. Likewise, Wagener et al. [76] reported a degradation reduction for aminopropyltriehtoxysilane/vitamin C-coated, pure Mg seeded with cells (endothelial cells, MG63) compared to the material control after five days of immersion. In these studies, the underlying mechanism was ascribed to the cell layer acting as a physical barrier which inhibits material-medium contact. Similarly, such a passivating effect induced by cell layers on material surfaces has previously been seen on non-degrading materials, such as titanium and stainless steel during electrochemical measurements [137, 138].

In the present study, however, an increasing cell layer density correlated with elevated degradation rates. These results suggest that cell layers might impact Mg degradation via multiple, simultaneously occurring mechanisms. In fact, a dense layer of cells and ECM might also hinder the diffusion of molecules and ions actively released by cells from below the cells to the surrounding bulk medium. As a consequence, the local accumulation of degradation promoting molecules or ions, such as H^+, may induce crevice/pitting corrosion below cells (Figure 36). The role of this degradation mechanism has previously been reported by Hiromoto et al. [139] on titanium and stainless steel substrates, and by Witecka et al. on Mg-2.0Zn0.98Mn [73].

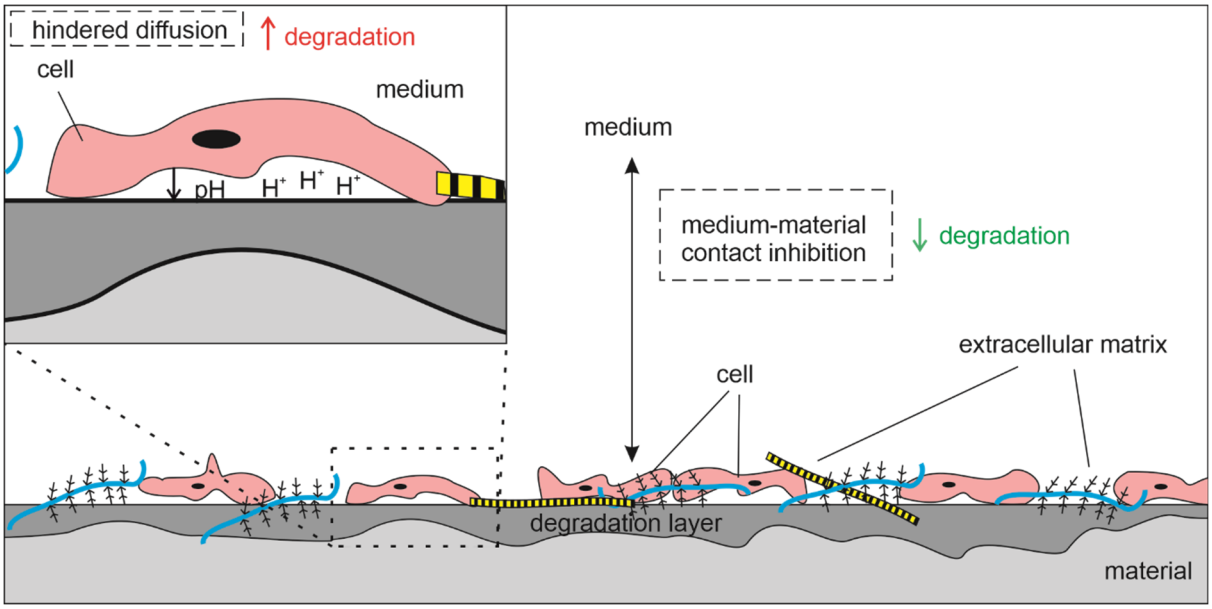

Figure 36 | Schematic illustration of the proposed degradation mechanisms related to cell layer formation. Cell layer formation may induce degradation inhibition due to medium-material contact inhibition and degradation promotion due to the hindered diffusion of acidifying cell metabolites.

The mapping of local pH of LN229-seeded Mg indirectly visualizes the hindered diffusion of ions through the cell layer further. In comparison to the cell-free control, the overall pH range (ΔpH) above Mg was significantly lower for LN229-seeded Mg. Yet, the degradation rate of comparable LN229-seeded Mg samples (compare Figure 12a 10^5 LN229) was significantly higher than the material control. Two approaches are conceivable to explain these observations. On one hand, a lower ΔpH could be an indicator for a more homogeneous degradation (less pitting corrosion). This explanation is not probable as later discussed in chapter 5.3.1. A more likely explanation is that the cell layer blurs the actual degradation-induced pH changes close to the material surface via hindered ion diffusion.

Additionally, Δosmolality values (Figure 12b) may indicate hindered diffusion. Figure 37 shows the schematic trend of Δosmolality and DR development in dependence of the cell amount observed in this study. Since the DR increases with a growing cell amount, the same trend would be expected for Δosmolality. However, the exact opposite trend was observed for Δosmolality (decreasing Δosmolality with an increasing cell amount). One explanation for the Δosmolality reduction is that osmotically active solutes, e.g., generated by Mg degradation, are trapped under a dense cell/ECM layer and do therefore not contribute to the osmolality measured in the supernatant. Further explanations are discussed in chapter 5.3.3.

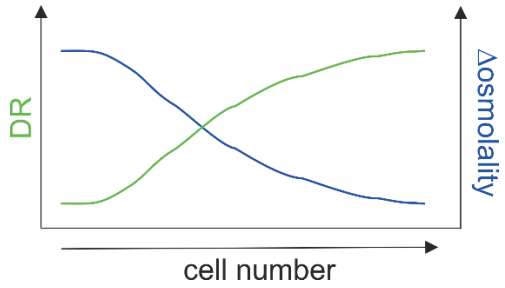

Figure 37 | Schematic trend of Δosmolality and DR development. The DR increases with an increasing number of initially seeded cells, while Δosmolality decreases.

It is conceivable that the actual cell layer impact is highly dependent on cell metabolic and proliferative activity. For instance, material-medium contact inhibition appears to be a relevant factor for degradation reduction for samples seeded with MMC-treated cells, whereas for untreated cells the mechanism of hindered diffusion seems to be more crucial.

5.3 Active cell influences on Mg degradation

5.3.1 Metabolism

In this study, cell-induced degradation promotion was predominantly observed for untreated, fast-proliferating cell types such as tumor cells, fibroblasts, and microglial cells. A high proliferative activity and hence increased cell number goes along with an increased overall content of metabolites which in turn can interact with the surface of an underlying Mg substrate. Cell metabolic activity has been reported to be one of the major impact factors for Mg degradation promotion [72, 73]. Cellular metabolic processes, such as cellular respiration, are closely linked to cellular pH homeostasis and thus pH development in the extracellular microenvironment. During cellular respiration, metabolic by-products (e.g., lactate/H^+ and CO_2) accumulate intracellularly, prompting extrusion mechanisms to maintain CO_2/pH homeostasis, as described in chapter 1.3.1. This in turn leads to local acidification of the extracellular microenvironment [88] and locally altered CO_2 contents, affecting Mg degradation.

Cell-induced acidification

In this thesis, cell-induced pH alterations and lactate production were analyzed as measures of cell metabolic activity. In fact, increased degradation correlated with elevated supernatant lactate levels (Figure 19). Nonetheless, the highest degradation rate observed (Figure 12a 10^5 HMC3 cells) did not correspond to the highest lactate content measured. These results suggest that HMC3-prompted degradation progression might not only be caused by local acidification due to lactate/H^+ extrusion. Instead, other acidification mechanisms, e.g., CO_2 conversion to carbonic acid in aqueous environment or via carbonic anhydrases, might additionally affect Mg degradation.

Moreover, the development of bulk pH correlated with the observed degradation trends and was shown to be cell type dependent (Figure 20). The degradation of Mg itself in aqueous environment causes alkalization, as described in chapter 1.2. Therefore, positive ΔpH values emerge as a result of ongoing degradation. Instead, negative ΔpH values either indicate degradation stabilization or regression (e.g., for MMC-treated cells), or they arise from severe cell-related acidification, which even superimposes alkalization evoked by degradation. To attribute the occurrence of negative ΔpH values to one of these two effects, a comparison with the respective degradation rates is necessary. Acidification caused by cells was particularly pronounced for HMC3 cells and tumor cells. The magnitude of cell-induced acidification is known to be cell type dependent and excessive in tumor cells owing to their altered cellular respiration (Warburg effect) and pH homeostasis mechanisms [81, 87, 88].

Suoto et al. [113] recently showed that the analysis of bulk pH only does not sufficiently reflect the degradation processes occurring at the material surface in cell-free experimental set-ups. Furthermore, a layer of cells/ECM can interfere with ion diffusion, as discussed in chapter 5.2, wherefore bulk pH measurements will not resemble local pH values around cells fully, as previously shown on inert titanium substrates [140]. This highlights the necessity to additionally analyze local pH when increasing the complexity of a Mg degradation system by adding cells and analyzing their influence on degradation. Local pH was measured for LN229 cells on Mg and inert substrates representatively via SIET. On Mg the mean local pH was slightly lower for samples seeded with cells than for the cell-free control (Figure 21), suggesting surface-near acidification by cells even under hydrodynamic conditions. Due to the underlying, degrading Mg material and the degradation-associated pH increase, cell-related acidification is not as obvious. Thus, local pH was additionally measured on inert TCP to quantify pH reduction by LN229 cells (Figure 22) approximately. The analysis affirmed an oscillating pattern of a notable pH reduction by 0.1-0.2 pH units (detection limit of the method is 0.01 pH units). Extracellular pH changes in a range even slightly higher than the range measured in this thesis have previously been reported for tumor cells *in vitro* and *in vivo* [141-

144]. The oscillating pattern is possibly related to the cyclic cellular respiration processes, as biochemical oscillations are commonly observed for multiple cellular processes [145, 146]. Nevertheless, it should be noted that the experimental conditions could also have caused the observed oscillation, since the measurement was conducted under atmospheric conditions owing to the set-up limitations. Additionally, the available SIET set-up used in this study is technically limited to pH measurements above the cell layer in a distance of ca. 50 µm. Hence, it can be assumed that the pH reduction below cells is even more pronounced, as observed by Satake et al. [147].

Degradation mechanisms related to cell-induced acidification

In terms of Mg degradation, local acidification can lead to the local reduction of the passivating abilities of the degradation product layer, resulting in degradation phenomena such as pitting corrosion [72, 139]. Indeed, the surface morphology analysis via SEM after six days of immersion for the slowest and fastest degrading sample confirmed severe pitting corrosion for fast-degrading samples seeded with HMC3 cells. As already mentioned above, HMC3 cells caused substantial acidification, which is presumably a major reason for the observed pitting.

Besides, the pH decrease modified the degradation layer thickness and morphology. Samples seeded with strongly acidifying cells, such as HMC3 cells, exhibited significantly thinner and less porous degradation layers as shown in Figure 38.

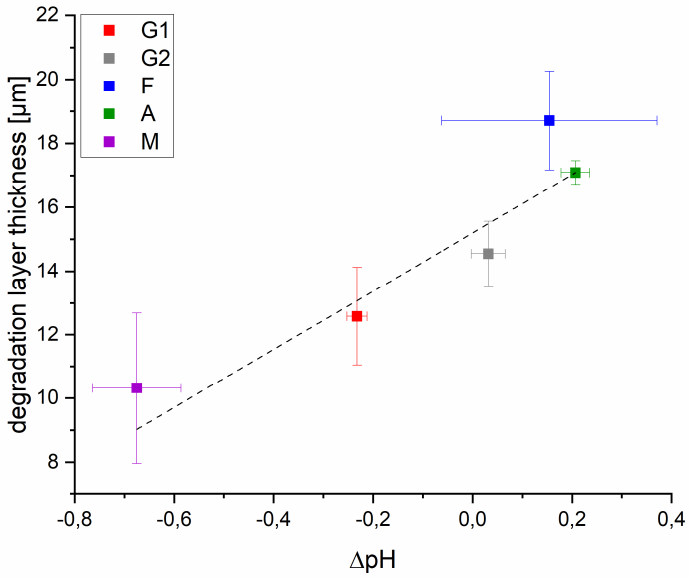

Figure 38 | Correlation of degradation layer thickness and cell-induced local acidification. The degradation layer thickness decreases with an increasing local acidification caused by LN229 (G1), A172 (G2), astrocytes (A), L929 (F) or HMC3 (M) cells (ΔpH on TCP).

A pH-dependence of degradation rate, product formation and product layer thickness is an accepted mechanism in Mg degradation [21, 22]. Under physiological conditions the degradation layer is typically composed of products such as e.g., $Mg(OH)_2$, $MgCO_3$, and Ca/P-phases [55, 60]. A stable layer of these compounds is known to passivate the magnesium surface, in turn leading to a decrease in degradation [55]. The solubility and precipitation of these compounds, however, is highly dependent on the surface and solution pH [148]. Surface alkalization (as a result of $Mg(OH)_2$ dissolution, as described in chapter 1.2) reduces the solubility of the degradation products and enhances precipitation due to oversaturation [56, 148]. In contrast, surface acidification (e.g., caused by cells) promotes the dissolution of the passivating degradation layer, as observed here for untreated cells. This degradation layer reduction caused by cell-related pH decrease can be assumed to be a major mechanism for Mg degradation promotion due to brain cells.

Cell metabolism-related degradation inhibiting effects

Moreover, the observed changes in degradation layer composition (highly increased levels of O and moderately increased levels of C, Figure 14 and Figure 15) for samples seeded with MMC-treated cells might also likely be attributed to cell metabolic effects. MMC is a chemotherapeutic drug that inhibits cell proliferation based on irreversible cross-linking of the double-stranded DNA [149]. However, other mechanisms of action, including the inhibition of glycolysis and stimulation of the TCA cycle in some types of cancer cells, have been reported for MMC [150]. While the TCA cycle yields CO_2 as a metabolic by-product, glycolysis and the subsequent ATP breakdown produce lactate/H^+ (compare chapter 1.3.1). Hence, the ratio of CO_2 to lactate/H^+ output may be expected to be changed (increased CO_2 and decreased lactate/H^+) in MMC-treated cells compared to untreated cells in this study.

In general, the presence of surface-near CO_2 might elicit two different mechanisms in the Mg degradation process. On one hand the released CO_2 can be an additional factor for local pH decrease as a result of CO_2 hydration and subsequent dissolution to H^+/HCO_3^- in aqueous media. This local pH decrease can induce the same degradation layer reduction mechanism as described above, if the pH decrease is too severe due to a high cell metabolic activity to be buffered by the bicarbonate buffering system in DMEM. On the other hand, the cell-produced CO_2 might lead to a favored formation of thermodynamically stable magnesium carbonates [53], if the local acidification is less severe owing to an altered cell metabolic activity as described for the MMC-treated cells.

5.3.2 Chemical interaction of extracellular matrix compounds with Mg

Aside from metabolites, cells actively secrete ECM molecules, which will likely be in direct contact with the subjacent Mg material. Organic molecules, such as proteins or amino acids, were previously shown to majorly impact Mg degradation [62, 63, 67]. Thus, studying the interaction of relevant ECM molecules with Mg is crucial to elucidate the corresponding degradation mechanisms. Here, the content and role of HA, CS and collagenous ECM products was analyzed representatively for the brain ECM. The ECM composition was shown to be dependent on the cell type, cell density and MMC treatment regarding the selected compounds. Moreover, the variation of ECM composition could be linked to distinctive degradation trends.

Impact of GAG compounds

Samples with higher contents of HA (Figure 27, e.g., astrocytes, 10^4 LN229) exhibited lower degradation rates than samples with low contents of HA (e.g., 10^5 LN229). The interaction analysis of HA and Mg by ATR-FTIR (Figure 29) showed chemisorption of HA on Mg via the carboxylic groups of HA. However, HA did not appear to favor the formation of new degradation products and did not significantly reduce Mg degradation in demineralized water (Figure 28). Yet, under physiological conditions, more specifically in the presence of inorganic salts, HA was reported to be a potential attenuator of Mg degradation [151, 152]. Kim et al. [151] demonstrated that HA coatings on plasma electrolytic oxidation (PEO)-coated Mg can decrease degradation and additionally indicated that HA alone might already slow down degradation. This degradation inhibiting effect might be related to the high binding affinity of HA towards Ca^{2+} and PO_4^{3-} [152]. Both ionic species are abundantly present in DMEM and can therefore be complexed by HA during the immersion in the cell culture medium. This in turn, can lead to surface-near oversaturation of Ca^{2+} and PO_4^{3-} and subsequent precipitation of Ca/P-products on top of the Mg degradation layer [148]. In fact, HA has previously been suggested to be used as a precursor to evoke hydroxyapatite, i.e., a Ca/P-product, formation on substrates for orthopedic applications by utilizing the described mechanism [153]. With regard to Mg, Ca/P degradation products are known to reduce Mg degradation. Indeed, the cross section analysis of HA-rich samples (Figure 14 10^5 astrocytes) confirmed the presence of higher Ca and P contents at the degradation layer surface.

On the other hand, samples with higher contents of CS (Figure 27 10^5 LN229, 10^5 HMC3) showed increased degradation compared to samples with low CS contents (MMC-treated LN229). Similarly to HA, CS can act as a chelator for divalent cations such as Ca^{2+} and Mg^{2+} [154-156]. In contrast to HA, CS may favor the formation of Mg-CS complexes through the

interaction of Mg^{2+} with the sulfate functional groups, as reported by Rodgers et al. [155]. Such a chelation of Mg^{2+} by CS was observed in the ATR-FTIR analysis, indicated by the decreasing IR bands at 3704 cm^{-1} and 1089 cm^{-1} (Figure 29c). The binding of Mg^{2+} to ECM molecules such as CS is thought to cause a shift in the chemical equilibrium of the Mg dissolution reaction (compare equations 1-3) and thus promotes degradation. An increase in degradation rate due to CS was additionally confirmed during the immersion of Mg discs in 0.05 M CS (Figure 28). Besides, the immersion test also revealed that the relatively low pH of CS (pH_{CS} = 4.69) might be an additional factor for Mg degradation promotion. It should be noted that, unlike HA, CS naturally only occurs covalently bound to a core protein forming CSPGs [154]. Even though the interaction of CSPGs and Mg substrates through the GAG side chains is a likely scenario owing to the structural conformation of PGs, additional interactions of the core proteins with the Mg substrates cannot be excluded entirely.

A third group of PG-bound GAGs, namely HS, plays a subordinate role in the brain ECM and was therefore not tested in detail in this study. Nevertheless, studies demonstrate that HS can likewise bind metal ions [157], though showing a higher affinity towards several divalent cations, including Ca^{2+}, than Mg^{2+} [157]. Thus, HS might impact Mg degradation in a similar manner (via chelation) as HA or CS.

The metal ion chelation by GAGs can additionally be deduced from the ∆osmolality values after six days of immersion (Figure 12b). This chelation might be a second explanation for unexpectedly decreased ∆osmolality values in addition to the trapping of osmotically active solutes under a cell/ECM barrier layer as described in chapter 5.2.

Impact of protein compounds

The analysis of collagen/elastin content via fluorescent staining did not allow any entirely valid correlations of protein content and degradation rate. The protein/cell ratio remained unaffected by the cell density for all cell types, except for HMC3 cells. For HMC3 cells, the protein content increased for higher cell densities and might therefore be associated with increased degradation for this cell type. Similarly, faster degrading untreated LN229 cells showed higher protein contents than slower degrading MMC-treated LN229 cells. The Col-F binding reagent used for the protein staining labels different kinds of collagens and elastin unspecifically. Accordingly, this analysis did not facilitate a detailed conclusion whether a specific type of collagen or elastin might be relevant for a potential degradation promoting effect.

To exemplify the role of proteins in the interaction of neural cells with Mg-based materials further, the impact of collagen IV was investigated in a highly simplified environment. An increased expression of collagen IV has been reported in GBM [95, 98], as it is a protein associated with the basement membrane of newly formed blood vessels (cancer hallmark

sustained angiogenesis). Therefore the impact of collagen IV on Mg degradation might be primarily of interest when studying the impact of GBM cells on Mg degradation. The analysis of supernatant arresten levels indeed confirmed increasing arresten contents with an increasing proliferative activity for the tumor cell lines LN229 and A172. Hence, a link between increased collagen IV expression and increased Mg degradation rate might be conceivable. Yet, in demineralized water, collagen IV caused Mg degradation inhibition. Protein-related inhibition of Mg degradation has mainly been linked to the formation of a passivating barrier layer as a result of protein adsorption [63], or the chelating/binding of Ca^{2+} and subsequent formation of degradation inhibiting Ca/P-phases in previous studies [67, 68]. On the other hand, Mg degradation promotion due to the presence of proteins has also been reported and has been ascribed to Mg^{2+} binding [66, 69], as observed for CS GAGs in this study. Generally, the role of proteins in Mg degradation is discussed to be highly complex and dependent on a vast number of influencing factors including, the type of protein, the surrounding medium composition, as well as the chemical and physical properties of the Mg material itself [63, 71]. Thus, there are two different explanations for the observed discrepancies:

i. Under physiological conditions, collagen IV might have a different (degradation increase) or no impact on Mg degradation compared to its impact in demineralized water. As previously shown, the change in salt-based medium composition alone can drastically alter the influence of proteins on the degradation outcome including the degradation rate, degradation product composition, degradation layer thickness and morphology [67]. In addition to that, Hou et al. [68] suggested that individual proteins in protein mixtures can interact and thereby change degradation even further. The actual *in vitro* situation is even more complex than the cell-free environments studied so far, as cell-secreted organic molecules add to the system. Therefore, the effect of collagen IV on Mg degradation in a simplified environment can only provide a basic understanding of the underlying mechanisms.

ii. The impact of collagen IV on Mg degradation under physiological conditions might be identical to its impact in demineralized water. Though, the role of collagen IV, or cell-secreted proteins in general, might be negligible in the neural cell system studied here. Firstly, fibrous proteins are not abundantly present in brain ECM [158]. And secondly, the amount of cell-secreted proteins is likely to be insignificant compared to the amount of proteins in the serum (FBS) of the CCM. Protein-related degradation effects in the studied system might therefore more likely be related to serum proteins rather than to cell-secreted proteins.

5.3.3 Other effects

Other effects that require attention when analyzing the impact of neural cells on Mg degradation include: the uptake of Mg^{2+} by cells, excretion of MMPs and ROS, as well as phagocytosis.

Mg^{2+} uptake

Mg^{2+} is one of the most abundant cations in the human organism and is involved in a number of physiologically relevant processes, such as cell proliferation, DNA stabilization, enzymatic reactions and protein synthesis. Under physiological conditions Mg^{2+} homeostasis is tightly regulated via ion channel transport mechanisms (e.g., via transient receptor potential cation channels subfamily M (TRMPs) such as TRPM6 and TRPM7). When introducing an external Mg^{2+} source (i.e., Mg-based implant) it can be expected that Mg^{2+} released from the source will be taken up by cells through these transport mechanisms. A cellular uptake of Mg^{2+} alters the chemical equilibrium of the Mg dissolution reaction (compare equations 1-3) and might thereby increase degradation. Concurrently, the removal of osmotically active Mg^{2+} from the surrounding environment will diminish the supernatant osmolality. This mechanism might be a third explanation for unexpectedly decreased ∆osmolality values observed in this study. In GBM the overexpression of TRPM7 [159] as well as increased Mg^{2+} levels in the tumor tissue [160, 161] have been reported. Consequently, the cellular uptake of Mg^{2+} might be higher in the GBM cells than in the healthy cell types used in this study, explaining the higher degradation rates for the GBM cells.

MMP secretion

The ECM is subjected to MMP-driven remodeling [100]. MMP expression is known to be dependent on cell type and cell density [162]. In GBM the expression of some MMPs (e.g., MMP2, -9) is increased, fostering ECM remodeling to build a tumor-favored microenvironment [163]. Therefore, MMPs can indirectly influence Mg degradation by digesting ECM molecules that inhibit or promote degradation cell type- and cell density-dependently.

ROS excretion

ROS are generated as a by-product in a number of physiological cellular processes, e.g., during oxidative phosphorylation, and are involved in cell signaling [164]. Commonly occurring ROS in cells include superoxides (O_2^-), hydroxyl radicals (HO•) and hydrogen peroxide (H_2O_2) [165]. ROS have a high oxidative ability and can increase Mg degradation once secreted by cells, as previously observed for macrophages by Zhang et al. [74]. For the cell types studied here, ROS are of particular relevance in microglial cells. Microglial have macrophage-like functions in the CNS and can react with increased ROS secretion upon activation as a

response to external stimuli [166]. Increased Mg degradation for HMC3-seeded samples might thus also be related to the secretion of ROS.

Phagocytosis

Phagocytosis describes the ingestion of small particles by cells such as macrophages, osteoclasts and activated microglia [167]. Zhang et al. [168] have recently reported the ability of macrophages to phagocytize degradation product fragments of a Mg-based alloy *in vitro*. Such a removal of degradation products from the degrading interface may be an additional mechanism for cell-induced degradation promotion. In this study, this mechanism is only relevant for HMC3 cells, as these cells are the only cells that are able to phagocytize after undergoing activation [169].

5.4 Summary of cell-induced Mg degradation mechanisms

It can be assumed that all or at least a majority of the aforementioned degradation mechanisms occur in parallel, creating a highly complex and dynamic degradation environment. The magnitude of single interaction mechanisms, and as a consequence thereof the degradation outcome, is dependent on the cell type and might furthermore be highly time-determined as suggested by Witecka et al. [73]. A time dependence of the involved degradation mechanisms has similarly been suggested for the interaction of Mg and organic molecules by Hou et al. [67].

At early stages of the material-cell interaction, the formation of a passivating barrier layer based on adsorbed proteins (from the cell culture medium) and cell bodies might initially stabilize the degradation layer and thereby inhibit Mg degradation. This process is likely to occur in most of the cell types analyzed here as the negative ΔpH values measured after three days of immersion (compare Figure s3) suggest. As mentioned before (chapter 5.3.1) negative ΔpH values can indicate both: cell-induced acidification as well as degradation inhibition. A clear assignment usually requires the respective degradation rate data. In this case, however, the ΔpH values measured on TCP under the same conditions can also be used to exclude severe acidification. It seems fair to assume, that cells require an initial time span of some hours to adhere to the material and to adjust to the new environment [170]. Only after these initial hours, cells will start to reinitiate certain cellular functions, such as proliferation [171, 172]. Therefore, the time interval during which a cell layer can inhibit degradation can be assumed to be dependent on how easily cells adapt to the new environment as well as on the cell metabolic and proliferative activity.

After the initial phase of cell attachment and as cells start to proliferate, secrete ECM and accumulate metabolites, the mechanisms of hindered diffusion of degradation promoting ions,

local acidification, ion binding etc. (described in chapter 5.3) will gain increasing relevance. Another factor that greatly highlights time dependence is enzyme-driven ECM digestion. Eventually, the degradation net outcome after a longer time of immersion depends on how degradation inhibiting effects balance degradation promoting effects. Based on the findings presented in this study, it can be concluded that after six days of immersion cell-induced acidification due to metabolic activity presumably weighs heaviest for the neural cells studied. To confirm this hypothesis further, an additional in-depth analysis of the cell-induced degradation mechanisms (i.e., changes in degradation rate, degradation layer thickness and composition) would have to be monitored at different time points in future research.A summary of all cell-related degradation mechanism studied in this thesis is shown in Figure 39.

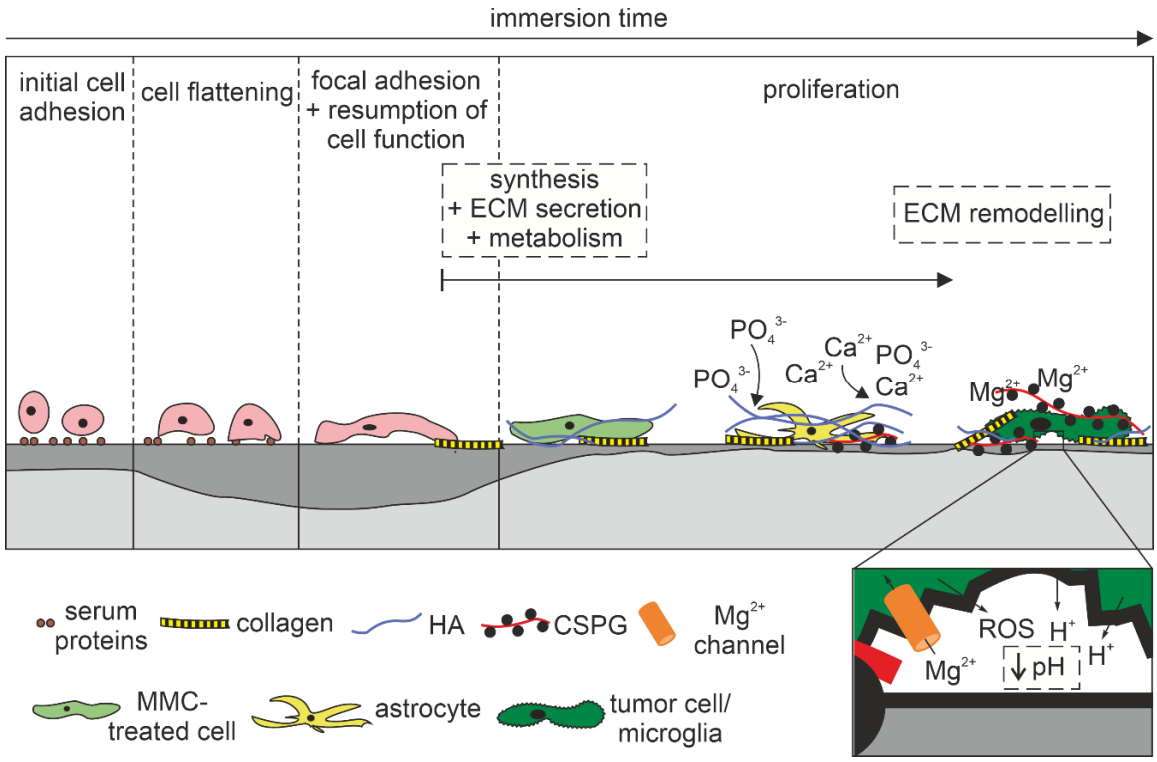

Figure 39 | Schematic summary of neural cell-induced Mg degradation mechanisms. During the initial processes of cell adhesion (first cell-material contact, cell flattening and focal adhesion), cells may inhibit Mg degradation owing to the formation of a passivating barrier layer composed of adsorbed serum proteins and cell bodies. As cells begin to reinitiate cellular functions, Mg degradation is majorly influenced by cell-secreted ions and molecules (ECM molecules + metabolites). The detailed mechanisms are cell type-dependent and include: formation of O/C-rich degradation layers (MMC-treated cells), precipitation of Ca/P-rich phases mediated by HA (astrocytes), local pH reduction due to metabolic acids, chemical equilibrium shift of the Mg dissolution reaction due to cellular Mg^{2+} uptake and binding/chelation of Mg^{2+} by ECM molecules and/or serum proteins, and Mg oxidation as a result of ROS secretion.

5.5 Stability and *in vitro* degradation of Mg-based thin films

Considering the functional importance and sensitivity of neural tissue, neural implants have to meet a variety of requirements, including suitable miniaturized geometries to prevent serious damage of functional and healthy tissue during implantation. Such customized and miniaturized geometries can be obtained from thin film fabrication via magnetron sputtering. Therefore, it is a promising fabrication method for Mg-based neural implants for potential clinical applications. To predict the *in vivo* performance of magnetron sputtered Mg-based neural implants, the *in vitro* degradation of Mg-based thin films was assessed.

Despite their low thickness of approximately 20 µm and extremely low weight (2-5 mg), pure Mg as well as Mg-6Ag thin films were shown to be sufficiently stable to allow weight loss measurement during *in vitro* testing after an immersion duration of four days. Pure Mg thin films exhibited degradation rates comparable to those measured for bulk Mg materials, whereas the degradation rates of Mg-6Ag thin films were higher than the degradation rates of the respective bulk material. Nevertheless, the degradation rates appeared to still be in an acceptable range for cell attachment, as discussed in detail hereinafter in chapter 5.6.

The difference in degradation rates between Mg-6Ag thin films and the respective bulk material is likely to occur owing to the difference in microstructural features between both materials. The extruded Mg-based discs exhibit isotropic microstructures, whereas magnetron sputtered Mg-based thin films typically feature textured microstructures [50, 173, 174]. During the sputtering process, single crystallites grow in hexagonal columns perpendicular onto the substrate with their basal planes facing the free surface. This can be decisive for the Mg degradation, as some crystallographic planes have been suggested to be more resistant towards degradation than others [175, 176]. More importantly though, the microstructure characterization (XRD analysis performed by Lea Jessen) of the Mg-6Ag thin films indicated the presence of intermetallic MgAg phases. Intermetallic phases are known to enhance Mg degradation, as they can act as local cathodes owing to their higher standard potential compared to Mg [177]. In bulk materials, a heat treatment (T4) following the actual process of material fabrication is required to increase the solubility of Ag in Mg, and thus to avoid the formation of intermetallic phases. Technically, magnetron sputtering facilitates the fabrication of single-phase materials with ultra-low degradation rates up to a concentration of 6 wt% Ag without the need of a subsequent heat treatment, as reported by Jessen et al. [50]. Yet, 6 wt% Ag appeared to be a critical maximum concentration of Ag at which the resulting thin film microstructure is extremely sensitive to nominal and practically unavoidable variations in the processing parameters (e.g., minimal changes in target composition after the use of a new sputtering target).

Moreover, the presence of intermetallic phases explains the optical appearance of Mg-6Ag thin films after degradation. The formation of galvanic cells around intermetallic particles caused localized degradation [177] which in turn became visible in form of the observed localized loss in film integrity. The thin film appearance of pure Mg thin films in contrast, indicated uniform degradation with no distinctive signs of severe localized degradation. Unlike Mg-6Ag thin films though, Mg thin films severely bent during degradation, which is presumably related to the formation of a degradation layer that introduces internal strains. To allow in-depth *in vitro* and future *in vivo* analysis of pure Mg thin films, thin film bending has to be avoided, as otherwise analysis becomes increasingly difficult or even impossible as can be seen from the cell viability staining images. Potential approaches to reduce thin film bending during *in vitro* analysis could for instance focus on fitting the thin films into customized plastic frames.

Cell-seeding, however, did not alter Mg or Mg-6Ag thin film degradation compared to the cell-free control. It can be assumed that the detailed degradation mechanisms during material-cell contact are somewhat similar (Mg-6Ag) or even identical (pure Mg) to the aforementioned and discussed cell-induced mechanisms. In fact, the results even support the hypothesis of time-dependent degradation outcome, as discussed in chapter 5.4.

Taken altogether, the *in vitro* degradation results confirm the general suitability of the thin films for additional short term *in vitro* studies and potentially also initial *in vivo* analysis (e.g., *post-mortem* implantation) in terms of material stability. Admittedly, the results also underline the necessity to improve the degradation resistance of the Mg-6Ag thin films if the fabrication of slow-degrading materials is desired for an intended application.

5.6 Suitability of Mg-based materials for neural applications

The interactions between neural cells and Mg-based materials do not only comprise the impact of selected cell types on the degradation, but also the impact of Mg degradation related effects on neural cells. These degradation-related effects include H_2 release, the elevation of surface pH, or the release of ionic species (Mg^{2+}, alloying elements) [51, 56, 60]. Depending on the intended application (e.g., cancer treatment, or base material for neural electrodes), a desired cell response to Mg-based materials and their degradation effects can range from apoptosis (GBM cells) to stimulation of anti-inflammatory properties (microglial cells). To establish Mg-based neural implants, an in depth-understanding of the detailed impact of these implants on neural cell fate is indispensable. Although a detailed investigation of the material impact on the cells was not the main focus of this work, a preliminary and very general cytocompatibility analysis has been performed in direct and indirect material contact for different neural cell types.

The cell viability staining as well as the cytoskeleton staining on pure Mg discs and thin films confirmed that all cell types adhered to the material in their cell-specific morphology and remained viable throughout the entire immersion time, indicating the general biocompatibility of Mg-based materials for neural applications. Likewise, the cell viability and cytoskeleton staining of LN229, HMC3 and astrocytes on Mg-6Ag thin films suggested a good biocompatibility of this type of material in spite of the relatively high degradation rate of ca. 0.8 mm/a. Though, cancer cells appeared to attach less wide spread compared to healthy cells, suggesting cell-specific cytotoxic effects. Such a tendency of higher material toxicity towards cancer cells compared to healthy cells was likewise observed during cytotoxicity analysis in indirect contact with Mg-6Ag thin films with even higher degradation rates (>1.5 mm/a). In contrast to Mg-6Ag thin films, tumor cell morphology remained unaffected on pure Mg discs after six days with lower degradation rates (ca. 0.3 mm/a), illustrating low toxicity. Cell-specific cytotoxic effects might therefore either be related to the altered degradation rate (higher cytotoxicity with an increased degradation rate), and thus to the accompanying degradation effects, or to the release of Ag^{2+}.

Generally, cytotoxic effects of Mg-based materials on cancer cells have previously been reported [44-46], underlining the potential of these materials to be used in cancer treatment strategies. However, cancer therapy faces the challenge of preserving the cell integrity of healthy cells in the tumor stroma while causing maximum damage to cancer cells [178]. Targeted cancer cell toxicity of Mg-based materials, as observed in this study and as recently reported by Globig at al. [179], therefore holds a great potential for novel approaches in cancer therapy. Furthermore, the seemingly low levels of toxicity towards healthy neural cells indicate that Mg-based thin films might also be a promising material to be applied in other neurological disorders such as epilepsy, AD and stroke. The application-specific efficacy of Mg-based thin film neural implants could largely be enhanced and customized by degradation rate tailoring (e.g., high degradation rates for cancer treatment, low degradation rates for neural electrode materials), alloying or therapeutically active agent coating.

6 Conclusion

In this thesis, the influence of neural cells on Mg degradation and some of the underlying degradation mechanisms were investigated to anticipate the *in vivo* material performance and suitability of Mg-based materials for neural applications. For this purpose, four different brain-related cells types were selected, representing physiological and pathological conditions to shed light on a broad range of cell-material interactions in the specific neural environment. In a second part, pure Mg and Mg-6Ag thin films were analyzed regarding their stability and suitability for neural application in preliminary *in vitro* degradation tests, as magnetron sputtering of Mg-based materials is a promising fabrication method to obtain clinically relevant implant geometries.

The degradation analysis reveals cell type- and cell density-dependent degradation behavior of pure Mg discs. Degradation promotion is observed mainly for cells with high proliferative activity (e.g., cancer cells, microglial cells), whereas slow-proliferating cells (e.g., MMC-treated cells, astrocytes) can be linked to degradation inhibition or invariance. Degradation promotion is majorly related to cell metabolism and hence local pH reduction. Local pH decrease does not only significantly affect the degradation rate, but also plays a role in the degradation layer formation. Additional degradation promoting effects observed in this thesis include the binding of Mg^{2+} to ECM products. In contrast, degradation inhibition is associated with the formation of a passivating layer of cell bodies and ECM, the formation of C/O-rich degradation products (presumably carbonates) and the mediating role of HA in Ca/P-phase precipitation. Most of these degradation mechanisms can be assumed to be time-determined and to counteract. The net degradation outcome is therefore highly dependent on the magnitude of single mechanisms, whereby cell-induced acidification appears to be the most relevant factor for the cells studied in this thesis.

Furthermore, Mg-based thin films prove to be sufficiently stable under *in vitro* conditions and qualify for further analysis. The initial cytotoxicity analysis shows that Mg-6Ag thin films may be a promising material for targeted cancer cell toxicity which might be controllable via degradation rate tailoring, alloying or additional coating with drug-loaded polymers/hydrogels.

Although the degradation analysis of Mg seeded with different types of neural cells elucidated a number of cell-material interactions, these interactions require more attention in even more complex systems, i.e., co-cultures of two or more cell types, to further approach *in vivo* conditions in future research. Moreover, an in-depth analysis of the impact of Mg and its degradation effects on neural cells is indispensable to draw final conclusions on the suitability and potential of Mg-based neural implants.

References

[1] J.H.F.d. Baaij, et al., Magnesium in Man: Implications for Health and Disease, Physiological Reviews 95(1) (2015) 1-46, doi:10.1152/physrev.00012.2014.

[2] W. Jahnen-Dechent, M. Ketteler, Magnesium basics, Clinical kidney journal 5(Suppl 1) (2012) i3-i14, doi:10.1093/ndtplus/sfr163.

[3] J.H.F. de Baaij, et al., Regulation of magnesium balance: lessons learned from human genetic disease, Clinical Kidney Journal 5(Suppl_1) (2012) i15-i24, doi:10.1093/ndtplus/sfr164.

[4] B.J.C. Luthringer, et al., Magnesium-based implants: a mini-review, Magnesium Research 27(4) (2014) 142-154, doi:10.1684/mrh.2015.0375.

[5] G. Song, A. Atrens, Understanding Magnesium Corrosion—A Framework for Improved Alloy Performance, Advanced Engineering Materials 5(12) (2003) 837-858, doi:10.1002/adem.200310405.

[6] C. Xu, W. Gao, Pilling-Bedworth ratio for oxidation of alloys, Material Research Innovations 3(4) (2000) 231-235, doi:10.1007/s100190050008.

[7] Y. Yang, et al., Mg bone implant: Features, developments and perspectives, Materials & Design 185 (2020) 108259, doi:10.1016/j.matdes.2019.108259.

[8] N. Sezer, et al., Review of magnesium-based biomaterials and their applications, Journal of Magnesium and Alloys 6(1) (2018) 23-43, doi:10.1016/j.jma.2018.02.003.

[9] Y. Liu, et al., Recent Progress on Mg- and Zn-Based Alloys for Biodegradable Vascular Stent Applications, Journal of Nanomaterials 2019 (2019) 1310792, doi:10.1155/2019/1310792.

[10] F. Witte, et al., Degradable biomaterials based on magnesium corrosion, Current Opinion in Solid State and Materials Science 12(5) (2008) 63-72, doi:10.1016/j.cossms.2009.04.001.

[11] P. Chakraborty Banerjee, et al., Magnesium Implants: Prospects and Challenges, Materials (Basel) 12(1) (2019) 136, doi:10.3390/ma12010136.

[12] J.-L. Wang, et al., Biodegradable Magnesium-Based Implants in Orthopedics—A General Review and Perspectives, Advanced Science 7(8) (2020) 1902443, doi:10.1002/advs.201902443.

[13] N. Kafkas, S. Dragasis, Current knowledge on very late stent thrombosis, Continuing Cardiology Education 4(1) (2018) 40-44, doi:10.1002/cce2.75.

[14] M. Bartosch, et al., Magnesium stents – fundamentals, biological implications and applications beyond coronary arteries, BioNanoMaterials 16(1) (2015) 3, doi:10.1515/bnm-2015-0004.

[15] F. Witte, The history of biodegradable magnesium implants: A review, Acta Biomaterialia 6(5) (2010) 1680-1692, doi:10.1016/j.actbio.2010.02.028.

[16] Y. Chen, et al., Recent advances on the development of magnesium alloys for biodegradable implants, Acta Biomaterialia 10(11) (2014) 4561-4573, doi:10.1016/j.actbio.2014.07.005.

[17] B.E.-F. de Ávila, et al., Micromotor-enabled active drug delivery for in vivo treatment of stomach infection, Nature Communications 8(1) (2017) 272, doi:10.1038/s41467-017-00309-w.

[18] A. Alfaro, et al., MgO nanoparticles coated with polyethylene glycol as carrier for 2-Methoxyestradiol anticancer drug, PLOS ONE 14(8) (2019) e0214900, doi:10.1371/journal.pone.0214900.

[19] T.A. Ranathunge, et al., Doxorubicin Loaded Magnesium Oxide Nanoflakes as pH Dependent Carriers for Simultaneous Treatment of Cancer and Hypomagnesemia, Nanomaterials (Basel) 9(2) (2019) 208, doi:10.3390/nano9020208.

[20] M. Guo, et al., Magnesium hydroxide nanoplates: a pH-responsive platform for hydrophobic anticancer drug delivery, Journal of Materials Chemistry B 1(39) (2013) 5273-5278, doi:10.1039/C3TB20466A.

[21] S. Johnston, et al., The influence of pH on the corrosion rate of high-purity Mg, AZ91 and ZE41 in bicarbonate buffered Hanks' solution, Corrosion Science 101 (2015) 182-192, doi:10.1016/j.corsci.2015.09.018.

[22] W.F. Ng, et al., Effect of pH on the in vitro corrosion rate of magnesium degradable implant material, Materials Science and Engineering: C 30(6) (2010) 898-903, doi:10.1016/j.msec.2010.04.003.

[23] C. Zhang, et al., Fabrication and Characterization of Biodegradable Metal Based Microelectrodes for In Vivo Neural Recording, MRS Advances 4(46-47) (2019) 2471-2477, doi:10.1557/adv.2019.302.

[24] C. Zhang, et al., Electrochemical deposition of conductive polymers onto magnesium microwires for neural electrode applications, Journal of Biomedical Materials Research Part A 106(7) (2018) 1887-1895, doi:10.1002/jbm.a.36385.

[25] M. Sebaa, et al., The effects of poly(3,4-ethylenedioxythiophene) coating on magnesium degradation and cytocompatibility with human embryonic stem cells for potential neural applications, Journal of Biomedical Materials Research Part A 103(1) (2015) 25-37, doi:10.1002/jbm.a.35142.

[26] J.J. Vennemeyer, et al., Initial observations on using magnesium metal in peripheral nerve repair, J Biomater Appl 29(8) (2015) 1145-1154, doi:10.1177/0885328214553135.

[27] T.M. Hopkins, et al., Short and long gap peripheral nerve repair with magnesium metal filaments, Journal of Biomedical Materials Research Part A 105(11) (2017) 3148-3158, doi:10.1002/jbm.a.36176.

[28] C. Zhang, et al., Magnesium-based biodegradable microelectrodes for neural recording, Materials Science and Engineering: C 110 (2020) 110614, doi:10.1016/j.msec.2019.110614.

[29] R. Yamanaka, et al., Magnesium Is a Key Player in Neuronal Maturation and Neuropathology, International Journal of Molecular Sciences 20(14) (2019) 3439.

[30] R. Daneman, A. Prat, The blood-brain barrier, Cold Spring Harb Perspect Biol 7(1) (2015) a020412-a020412, doi:10.1101/cshperspect.a020412.

[31] J. Erdman, et al., Nutrition and traumatic brain injury: Improving acute and subacute health outcomes in military personnel, 2011.

[32] Magnesium in the Central Nervous System, The University of Adelaide Press2011.

[33] D. Stroebel, et al., Triheteromeric NMDA receptors: from structure to synaptic physiology, Current opinion in physiology 2 (2018) 1-12, doi:10.1016/j.cophys.2017.12.004.

[34] A.E. Kirkland, et al., The Role of Magnesium in Neurological Disorders, Nutrients 10(6) (2018) 730, doi:10.3390/nu10060730.

[35] X.-x. Dong, et al., Molecular mechanisms of excitotoxicity and their relevance to pathogenesis of neurodegenerative diseases, Acta Pharmacologica Sinica 30(4) (2009) 379-387, doi:10.1038/aps.2009.24.

[36] W. Li, et al., Elevation of brain magnesium prevents synaptic loss and reverses cognitive deficits in Alzheimer's disease mouse model, Mol Brain 7 (2014) 65-65, doi:10.1186/s13041-014-0065-y.

[37] A.P. Sen, A. Gulati, Use of magnesium in traumatic brain injury, Neurotherapeutics 7(1) (2010) 91-99, doi:10.1016/j.nurt.2009.10.014.

[38] P. Wlaź, et al., The effect of an acute and 7-day administration of magnesium chloride on magnesium concentration in the serum, erythrocytes, and brain of rats, Pharmacological Reports 68(2) (2016) 289-291, doi:10.1016/j.pharep.2015.09.006.

[39] W. Li, et al., Magnesium Sulfate for Acute Traumatic Brain Injury, Journal of Craniofacial Surgery 26(2) (2015) 393-398, doi:10.1097/scs.0000000000001339.

[40] X. Dong, Current Strategies for Brain Drug Delivery, Theranostics 8(6) (2018) 1481-1493, doi:10.7150/thno.21254.

[41] T.A. Juratli, et al., Current status of local therapy in malignant gliomas — A clinical review of three selected approaches, Pharmacology & Therapeutics 139(3) (2013) 341-358, doi:10.1016/j.pharmthera.2013.05.003.

[42] S.J. Cameron, et al., A Current Overview of the Biological and Cellular Effects of Nanosilver, International journal of molecular sciences, 2018.

[43] M.A. Franco-Molina, et al., Antitumor activity of colloidal silver on MCF-7 human breast cancer cells, J Exp Clin Cancer Res, 2010, p. 148.

[44] Q. Wang, et al., Cytotoxic Effects of Biodegradation of Pure Mg and MAO-Mg on Tumor Cells of MG63 and KB, Journal of Materials Science & Technology 30(5) (2014) 487-492, doi:10.1016/j.jmst.2014.03.004.

[45] Y. Zhang, et al., Preliminary Study on Cytotoxic Effect of Biodegradation of Magnesium on Cancer Cells, Journal of Materials Science & Technology 28(9) (2012) 769-772, doi:10.1016/S1005-0302(12)60128-5.

[46] M. Li, et al., Cytotoxic Effect on Osteosarcoma MG-63 Cells by Degradation of Magnesium, Journal of Materials Science & Technology 30(9) (2014) 888-893, doi:10.1016/j.jmst.2014.04.010.

[47] H. Qi, et al., Electrophoretic Deposition of Bioadaptive Drug Delivery Coatings on Magnesium Alloy for Bone Repair, ACS Applied Materials & Interfaces 11(8) (2019) 8625-8634, doi:10.1021/acsami.9b01227.

[48] J. Ma, et al., Similarities and differences in coatings for magnesium-based stents and orthopaedic implants, Journal of Orthopaedic Translation 2(3) (2014) 118-130, doi:10.1016/j.jot.2014.03.004.

[49] M. Chagnon, et al., Evaluation of Magnesium-based Medical Devices in Preclinical Studies: Challenges and Points to Consider, Toxicologic Pathology 47(3) (2019) 390-400, doi:10.1177/0192623318816936.

[50] L.K. Jessen, et al., Magnetron sputtered freestanding MgAg films with ultra-low corrosion rate, Acta Biomaterialia 98 (2019) 81-87, doi:10.1016/j.actbio.2019.05.060.

[51] M. Esmaily, et al., Fundamentals and advances in magnesium alloy corrosion, Progress in Materials Science 89 (2017) 92-193, doi:10.1016/j.pmatsci.2017.04.011.

[52] A.H.M. Sanchez, et al., Mg and Mg alloys: How comparable are in vitro and in vivo corrosion rates? A review, Acta Biomaterialia 13 (2015) 16-31, doi:10.1016/j.actbio.2014.11.048.

[53] M. Kieke, et al., Degradation rates and products of pure magnesium exposed to different aqueous media under physiological conditions, BioNanoMaterials 17(3-4) (2016) 131, doi:10.1515/bnm-2015-0020.

[54] R. Harrison, et al., Corrosion of magnesium and magnesium–calcium alloy in biologically-simulated environment, Progress in Natural Science: Materials International 24(5) (2014) 539-546, doi:10.1016/j.pnsc.2014.08.010.

[55] V. Wagener, S. Virtanen, Protective layer formation on magnesium in cell culture medium, Materials Science and Engineering: C 63 (2016) 341-351, doi:10.1016/j.msec.2016.03.003.

[56] S. Virtanen, Biodegradable Mg and Mg alloys: Corrosion and biocompatibility, Materials Science and Engineering: B 176(20) (2011) 1600-1608, doi:10.1016/j.mseb.2011.05.028.

[57] E. Ghali, et al., General and localized corrosion of magnesium alloys: A critical review, Journal of Materials Engineering and Performance 13(1) (2004) 7-23, doi:10.1361/10599490417533.

[58] L.L. Hamm, et al., Acid-Base Homeostasis, Clin J Am Soc Nephrol 10(12) (2015) 2232-2242, doi:10.2215/CJN.07400715.

[59] A.S. Silva, et al., The potential role of systemic buffers in reducing intratumoral extracellular pH and acid-mediated invasion, Cancer Res 69(6) (2009) 2677-2684, doi:10.1158/0008-5472.CAN-08-2394.

[60] J. Gonzalez, et al., Magnesium degradation under physiological conditions – Best practice, Bioactive Materials 3(2) (2018) 174-185, doi:10.1016/j.bioactmat.2018.01.003.

[61] N.A. Agha, et al., Magnesium degradation influenced by buffering salts in concentrations typical of in vitro and in vivo models, Materials Science and Engineering: C 58 (2016) 817-825, doi:10.1016/j.msec.2015.09.067.

[62] I. Johnson, et al., The Effects of Serum Proteins on Magnesium Alloy Degradation in Vitro, Scientific Reports 7(1) (2017) 14335, doi:10.1038/s41598-017-14479-6.

[63] S. Höhn, et al., Protein adsorption on magnesium and its alloys: A review, Applied Surface Science 464 (2019) 212-219, doi:10.1016/j.apsusc.2018.08.173.

[64] J. Walker, et al., Magnesium alloys: Predicting in vivo corrosion with in vitro immersion testing, Journal of Biomedical Materials Research Part B: Applied Biomaterials 100B(4) (2012) 1134-1141, doi:10.1002/jbm.b.32680.

[65] C.-L. Liu, et al., Synergistic effect of chloride ion and albumin on the corrosion of pure magnesium, Frontiers of Materials Science 8(3) (2014) 244-255, doi:10.1007/s11706-014-0251-y.

[66] A. Yamamoto, S. Hiromoto, Effect of inorganic salts, amino acids and proteins on the degradation of pure magnesium in vitro, Materials Science and Engineering: C 29(5) (2009) 1559-1568, doi:10.1016/j.msec.2008.12.015.

[67] R.-Q. Hou, et al., Exploring the effects of organic molecules on the degradation of magnesium under cell culture conditions, Corrosion Science 132 (2018) 35-45, doi:10.1016/j.corsci.2017.12.023.

[68] R.-Q. Hou, et al., Different effects of single protein vs. protein mixtures on magnesium degradation under cell culture conditions, Acta Biomaterialia 98 (2019) 256-268, doi:10.1016/j.actbio.2019.02.013.

[69] T. Li, et al., Influence of albumin on in vitro degradation behavior of biodegradable Mg-1.5Zn-0.6Zr-0.2Sc alloy, Materials Letters 217 (2018), doi:10.1016/j.matlet.2018.01.082.

[70] R.-C. Zeng, et al., In vitro degradation of pure Mg in response to glucose, Scientific Reports 5(1) (2015) 13026, doi:10.1038/srep13026.

[71] R. Hou, et al., Adsorption of Proteins on Degradable Magnesium—Which Factors are Relevant?, ACS Applied Materials & Interfaces 10(49) (2018) 42175-42185, doi:10.1021/acsami.8b17507.

[72] M.B. Kannan, et al., Influence of living cells (L929) on the biodegradation of magnesium–calcium alloy, Colloids and Surfaces B: Biointerfaces 126 (2015) 603-606, doi:10.1016/j.colsurfb.2015.01.015.

[73] A. Witecka, et al., Influence of SaOS-2 cells on corrosion behavior of cast Mg-2.0Zn0.98Mn magnesium alloy, Colloids and Surfaces B: Biointerfaces 150 (2017) 288-296, doi:10.1016/j.colsurfb.2016.10.041.

[74] J. Zhang, et al., Effect of macrophages on in vitro corrosion behavior of magnesium alloy, Journal of Biomedical Materials Research Part A 104(10) (2016) 2476-2487, doi:10.1002/jbm.a.35788.

[75] F. Seuss, et al., Corrosion of Mg alloy AZ91D in the presence of living cells, Journal of Biomedical Materials Research Part B: Applied Biomaterials 99B(2) (2011) 276-281, doi:10.1002/jbm.b.31896.

[76] V. Wagener, et al., Cell Adhesion on Surface-Functionalized Magnesium, ACS Applied Materials & Interfaces 8(19) (2016) 11998-12006, doi:10.1021/acsami.6b01747.

[77] N. Ahmad Agha, et al., The Degradation Interface of Magnesium Based Alloys in Direct Contact with Human Primary Osteoblast Cells, PLOS ONE 11(6) (2016) e0157874, doi:10.1371/journal.pone.0157874.

[78] E.K. Brooks, et al., Influence of MC3T3-E1 preosteoblast culture on the corrosion of a T6-treated AZ91 alloy, J Biomed Mater Res B Appl Biomater 104(2) (2016) 253-262, doi:10.1002/jbm.b.33378.

[79] M. CHESLER, Regulation and Modulation of pH in the Brain, Physiological Reviews 83(4) (2003) 1183-1221, doi:10.1152/physrev.00010.2003.

[80] R.W. Putnam, 22 - Intracellular pH Regulation, in: N. Sperelakis (Ed.), Cell Physiology Source Book (Third Edition), Academic Press, San Diego, 2001, pp. 357-372.

[81] P. Swietach, et al., The chemistry, physiology and pathology of pH in cancer, Philosophical Transactions of the Royal Society B: Biological Sciences 369(1638) (2014) 20130099, doi:10.1098/rstb.2013.0099.

[82] M.J. Rogatzki, et al., Lactate is always the end product of glycolysis, Front Neurosci 9 (2015) 22-22, doi:10.3389/fnins.2015.00022.

[83] M.-G. Vera, et al., Lactate Transporters and pH Regulation: Potential Therapeutic Targets in Glioblastomas, Current Cancer Drug Targets 16(5) (2016) 388-399, doi:10.2174/1568009616666151222150543.

[84] B. Blombach, R. Takors, CO2 - Intrinsic Product, Essential Substrate, and Regulatory Trigger of Microbial and Mammalian Production Processes, Frontiers in bioengineering and biotechnology 3 (2015) 108-108, doi:10.3389/fbioe.2015.00108.

[85] J.W. Deitmer, C.R. Rose, pH regulation and proton signalling by glial cells, Progress in Neurobiology 48(2) (1996) 73-103, doi:10.1016/0301-0082(95)00039-9.

[86] C.-K. Tong, et al., Interstitial Carbonic Anhydrase (CA) Activity in Brain Is Attributable to Membrane-Bound CA Type IV, The Journal of Neuroscience 20(22) (2000) 8247-8253, doi:10.1523/jneurosci.20-22-08247.2000.

[87] M.V. Liberti, J.W. Locasale, The Warburg Effect: How Does it Benefit Cancer Cells?, Trends in Biochemical Sciences 41(3) (2016) 211-218, doi:10.1016/j.tibs.2015.12.001.

[88] M. Damaghi, et al., pH sensing and regulation in cancer, Frontiers in Physiology 4(370) (2013), doi:10.3389/fphys.2013.00370.

[89] M.A. Proescholdt, et al., Function of carbonic anhydrase IX in glioblastoma multiforme, Neuro Oncol 14(11) (2012) 1357-1366, doi:10.1093/neuonc/nos216.

[90] S.K. Parks, et al., Disrupting proton dynamics and energy metabolism for cancer therapy, Nature Reviews Cancer 13(9) (2013) 611-623, doi:10.1038/nrc3579.

[91] C.S. Barros, et al., Extracellular matrix: functions in the nervous system, Cold Spring Harb Perspect Biol 3(1) (2011) a005108-a005108, doi:10.1101/cshperspect.a005108.

[92] D.R. Zimmermann, M.T. Dours-Zimmermann, Extracellular matrix of the central nervous system: from neglect to challenge, Histochemistry and Cell Biology 130(4) (2008) 635-653, doi:10.1007/s00418-008-0485-9.

[93] U. Novak, A.H. Kaye, Extracellular matrix and the brain: components and function, Journal of Clinical Neuroscience 7(4) (2000) 280-290, doi:10.1054/jocn.1999.0212.

[94] A. Belousov, et al., The Extracellular Matrix and Biocompatible Materials in Glioblastoma Treatment, Frontiers in Bioengineering and Biotechnology 7(341) (2019), doi:10.3389/fbioe.2019.00341.

[95] L.W. Lau, et al., Pathophysiology of the brain extracellular matrix: a new target for remyelination, Nature Reviews Neuroscience 14(10) (2013) 722-729, doi:10.1038/nrn3550.

[96] M.V.R. Marzenna Wiranowska, Extracellular Matrix Environment in Glioma Progression, in: D.A. Ghosh (Ed.), Glioma - Exploring Its Biology and Practical Relevance, InTech2011, pp. 257-284.

[97] D. Bonneh-Barkay, C.A. Wiley, Brain extracellular matrix in neurodegeneration, Brain Pathol 19(4) (2009) 573-585, doi:10.1111/j.1750-3639.2008.00195.x.

[98] L.S. Payne, P.H. Huang, The pathobiology of collagens in glioma, Mol Cancer Res 11(10) (2013) 1129-1140, doi:10.1158/1541-7786.MCR-13-0236.

[99] A. Malandrino, et al., Complex mechanics of the heterogeneous extracellular matrix in cancer, Extreme Mechanics Letters 21 (2018) 25-34, doi:10.1016/j.eml.2018.02.003.

[100] H.S. Sonbol, Extracellular Matrix Remodeling in Human Disease, J Microsc Ultrastruct 6(3) (2018) 123-128, doi:10.4103/JMAU.JMAU_4_18.

[101] H. Fujioka, et al., Neural Functions of Matrix Metalloproteinases: Plasticity, Neurogenesis, and Disease, Biochemistry Research International 2012 (2012) 789083, doi:10.1155/2012/789083.

[102] V.W. Yong, Metalloproteinases: Mediators of Pathology and Regeneration in the CNS, Nature Reviews Neuroscience 6(12) (2005) 931-944, doi:10.1038/nrn1807.

[103] V.W. Yong, et al., Metalloproteinases in biology and pathology of the nervous system, Nature Reviews Neuroscience 2(7) (2001) 502-511, doi:10.1038/35081571.

[104] G. Musumeci, et al., Characterization of matrix metalloproteinase-2 and -9, ADAM-10 and N-cadherin expression in human glioblastoma multiforme, Cell and Tissue Research 362(1) (2015) 45-60, doi:10.1007/s00441-015-2197-5.

[105] R.S. Pessoa, et al., 18 - Plasma-assisted techniques for growing hard nanostructured coatings: An overview, in: M. Aliofkhazraei (Ed.), Anti-Abrasive Nanocoatings, Woodhead Publishing2015, pp. 455-479.

[106] K. König, et al., Optically Induced Nanostructures, De Gruyter2015.

[107] L.K. Jessen, et al., Mechanical Properties of Magnetron Sputtered Free Standing Mg-Ag Alloy Films, Frontiers in Materials 6(236) (2019), doi:10.3389/fmats.2019.00236.

[108] ASTM, G31-72 (2004) Standard Practice for Laboratory Immersion Corrosion Testing of Metals, ASTM International, West Conshohocken, PA, 2004, p. 8.

[109] J. Stricker, et al., Mechanics of the F-actin cytoskeleton, Journal of Biomechanics 43(1) (2010) 9-14, doi:10.1016/j.jbiomech.2009.09.003.

[110] Z.L. Wang, J.L. Lee, Chapter 9 - Electron Microscopy Techniques for Imaging and Analysis of Nanoparticles, in: R. Kohli, K.L. Mittal (Eds.), Developments in Surface Contamination and Cleaning (Second Edition), William Andrew Publishing, Oxford, 2008, pp. 395-443.

[111] M. Uo, et al., Applications of X-ray fluorescence analysis (XRF) to dental and medical specimens, Japanese Dental Science Review 51(1) (2015) 2-9, doi:10.1016/j.jdsr.2014.07.001.

[112] Interpretation of Infrared Spectra, A Practical Approach, Encyclopedia of Analytical Chemistry.

[113] R. Souto, et al., In-situ visualization of local corrosion by Scanning Ion-selective Electrode Technique (SIET), 2010, pp. 2162-2173.

[114] S. Tong, et al., Non-invasive scanning ion-selective electrode technique and its applications to the research of higher plants, Progress in Natural Science 17(6) (2007) 625-629, doi:10.1080/10002007088537450.

[115] A. Dimberg, M. Sund, Cancer Angiogenesis and Vasculogenesis, 2014, pp. 403-411.

[116] B. Gallagher, Basal laminar thinning in branching morphogenesis of the chick lung as demonstrated by lectin probes, Journal of embryology and experimental morphology 94 (1986) 173-88.

[117] J.r. Winkler, H. Lünsdorf, Ultrastructure and Composition of Asteroid Bodies, Investigative Ophthalmology & Visual Science 42(5) (2001) 902-907.

[118] S.G. Kazarian, K.L.A. Chan, ATR-FTIR spectroscopic imaging: recent advances and applications to biological systems, Analyst 138(7) (2013) 1940-1951, doi:10.1039/C3AN36865C.

[119] A.P. Vinogradov, et al., Exciting surface plasmon polaritons in the Kretschmann configuration by a light beam, Physical Review B 97(23) (2018) 235407, doi:10.1103/PhysRevB.97.235407.

[120] R. Unbehau, et al., The impact of brain cell metabolism and extracellular matrix on magnesium degradation, Acta Biomaterialia (2020), doi:10.1016/j.actbio.2020.08.043.

[121] Y. Xin, et al., Influence of aggressive ions on the degradation behavior of biomedical magnesium alloy in physiological environment, Acta Biomaterialia 4(6) (2008) 2008-2015, doi:10.1016/j.actbio.2008.05.014.

[122] M. Jönsson, et al., Corrosion product formation during NaCl induced atmospheric corrosion of magnesium alloy AZ91D, Corrosion Science 49(3) (2007) 1540-1558, doi:10.1016/j.corsci.2006.08.004.

[123] A. de ninno, et al., Top-Down approach to nanotechnology for cell-on-chip applications, Biophysics and Bioengineering Letters 3 (2010).

[124] A.A. Bunaciu, et al., Cancer diagnosis by ft-Ir Spectrophotometry, 60 (2015) 415-426.

[125] W. Mihoubi, et al., FTIR spectroscopy of whole cells for the monitoring of yeast apoptosis mediated by p53 over-expression and its suppression by Nigella sativa extracts, PLOS ONE 12(7) (2017) e0180680, doi:10.1371/journal.pone.0180680.

[126] M.L.S. Mello, B.C. Vidal, Changes in the Infrared Microspectroscopic Characteristics of DNA Caused by Cationic Elements, Different Base Richness and Single-Stranded Form, PLOS ONE 7(8) (2012) e43169, doi:10.1371/journal.pone.0043169.

[127] T. Takeshita, et al., Biomineralization of Hydroxyapatite on DNA Molecules in SBF: Morphological Features and Computer Simulation, Langmuir 29(38) (2013) 11975-11981, doi:10.1021/la402589j.

[128] R. Willumeit, et al., Chemical surface alteration of biodegradable magnesium exposed to corrosion media, Acta Biomaterialia 7(6) (2011) 2704-2715, doi:10.1016/j.actbio.2011.03.004.

[129] R. Gao, et al., Fabrication of superhydrophobic magnesium alloy through the oxidation of hydrogen peroxide, Colloids and Surfaces A: Physicochemical and Engineering Aspects 436 (2013) 906-911, doi:10.1016/j.colsurfa.2013.08.020.

[130] Y. Ren, et al., Microwave Assisted Magnesium Phosphate Coating on AZ31 Magnesium Alloy, Biomedical Materials 12 (2017), doi:10.1088/1748-605X/aa78c0.

[131] S. Gaudenzi, et al., Cell apoptosis specific marker found by Fourier Transform Infrared Spectroscopy, Journal of Spectroscopy 18 (2004), doi:10.1155/2004/483591.

[132] N.C.S. Selvam, et al., Comparative study of microwave and conventional methods for the preparation and optical properties of novel MgO-micro and nano-structures, Journal of Alloys and Compounds 509(41) (2011) 9809-9815, doi:10.1016/j.jallcom.2011.08.032.

[133] M. Kandiban, et al., Synthesis and characterization of MgO nanoparticles for photocatalytic applications, 2015.

[134] L. Ai, et al., Sacrificial template-directed synthesis of mesoporous manganese oxide architectures with superior performance for organic dye adsorption, Nanoscale 4(17) (2012) 5401-5408, doi:10.1039/C2NR31333B.

[135] L.I. Fockaert, et al., ATR-FTIR in Kretschmann configuration integrated with electrochemical cell as in situ interfacial sensitive tool to study corrosion inhibitors for magnesium substrates, Electrochimica Acta 345 (2020) 136166, doi:10.1016/j.electacta.2020.136166.

[136] J. Ovalles, Determination of Sulphate for Measuring Magnesium Sulphate in Pharmaceuticals by Flow Analysis-Fourier Transforms Infrared Spectroscopy, LATIN AMERICAN JOURNAL OF PHARMACY 28 (2009) 173-182.

[137] S. Hiromoto, et al., Electrochemical properties of an interface between titanium and fibroblasts L929, Electrochimica Acta 48(4) (2002) 387-396, doi:10.1016/S0013-4686(02)00684-9.

[138] S. Hiromoto, T. Hanawa, Electrochemical properties of 316L stainless steel with culturing L929 fibroblasts, Journal of the Royal Society, Interface / the Royal Society 3 (2006) 495-505, doi:10.1098/rsif.2005.0108.

[139] S. Hiromoto, Corrosion of metallic biomaterials in cell culture environments, Electrochemical Society Interface 17 (2008) 41-44.

[140] S. Hiromoto, T. Hanawa, pH near Cells on Stainless Steel and Titanium, Electrochemical and Solid-State Letters 7(3) (2004) B9, doi:10.1149/1.1645353.

[141] M. Naciri, et al., Monitoring pH and dissolved oxygen in mammalian cell culture using optical sensors, Cytotechnology 57(3) (2008) 245-250, doi:10.1007/s10616-008-9160-1.

[142] R. Ohgaki, et al., Ratiometric fluorescence imaging of cell surface pH by poly(ethylene glycol)-phospholipid conjugated with fluorescein isothiocyanate, Scientific Reports 7(1) (2017) 17484, doi:10.1038/s41598-017-17459-y.

[143] C. Stock, et al., pH Nanoenvironment at the Surface of Single Melanoma Cells, Cellular Physiology and Biochemistry 20(5) (2007) 679-686, doi:10.1159/000107550.

[144] Y. Zhang, et al., High-resolution label-free 3D mapping of extracellular pH of single living cells, Nature Communications 10(1) (2019) 5610, doi:10.1038/s41467-019-13535-1.

[145] S. Iotti, et al., Oscillations in energy metabolism, Biochimica et Biophysica Acta (BBA) - Bioenergetics 1797(8) (2010) 1353-1361, doi:10.1016/j.bbabio.2010.02.019.

[146] A. Papagiannakis, et al., Autonomous Metabolic Oscillations Robustly Gate the Early and Late Cell Cycle, Molecular Cell 65(2) (2017) 285-295, doi:10.1016/j.molcel.2016.11.018.

[147] H. Satake, et al., Elucidation of interfacial pH behaviour at the cell/substrate nanogap for in situ monitoring of cellular respiration, Nanoscale 10(21) (2018) 10130-10136, doi:10.1039/C8NR02950D.

[148] F. Scholz, H. Kahlert, The calculation of the solubility of metal hydroxides, oxide-hydroxides, and oxides, and their visualisation in logarithmic diagrams, ChemTexts 1(1) (2015) 7, doi:10.1007/s40828-015-0006-0.

[149] M. Tomasz, Y. Palom, The mitomycin bioreductive antitumor agents: Cross-linking and alkylation of DNA as the molecular basis of their activity, Pharmacology & Therapeutics 76(1) (1997) 73-87, doi:10.1016/S0163-7258(97)00088-0.

[150] T. Saito, T. Kaneko, Effects of simultaneous application of mitomycin C and prednisolone on respiration and glycolysis of Ehrlich ascites tumor cells in vitro, Tohoku J Exp Med 95(1) (1968) 87-106, doi:10.1620/tjem.95.87.

[151] Y.-K. Kim, et al., Functions achieved by the hyaluronic acid derivatives coating and hydroxide film on bio-absorbed Mg, Applied Surface Science 473 (2019) 31-39, doi:10.1016/j.apsusc.2018.12.139.

[152] I. Milošev, et al., Hyaluronic acid stimulates the formation of calcium phosphate on CoCrMo alloy in simulated physiological solution, Journal of Materials Science: Materials in Medicine 24(3) (2013) 555-571, doi:10.1007/s10856-012-4827-8.

[153] Q. Li, et al., In vitro synthesis of bioactive hydroxyapatite using sodium hyaluronate as a template, Journal of Materials Chemistry 22(38) (2012) 20257-20265, doi:10.1039/C2JM33624C.

[154] G.M. Campo, et al., Chondroitin sulphate: antioxidant properties and beneficial effects, Mini Rev Med Chem 6(12) (2006) 1311-1320, doi:10.2174/138955706778993012.

[155] A.L. Rodgers, G.E. Jackson, Determination of thermodynamic parameters for complexation of calcium and magnesium with chondroitin sulfate isomers using isothermal titration calorimetry: Implications for calcium kidney-stone research, Journal of Crystal Growth 463 (2017) 14-18, doi:10.1016/j.jcrysgro.2017.01.056.

[156] S. Li, et al., Synthesis of chondroitin sulfate magnesium for osteoarthritis treatment, Carbohydrate Polymers 212 (2019) 387-394, doi:10.1016/j.carbpol.2019.02.061.

[157] I. Stevic, et al., Binding of Heparin to Metals, Cell Biochemistry and Biophysics 59(3) (2011) 171-178, doi:10.1007/s12013-010-9129-5.

[158] I. Koh, et al., The mode and dynamics of glioblastoma cell invasion into a decellularized tissue-derived extracellular matrix-based three-dimensional tumor model, Scientific Reports 8(1) (2018) 4608, doi:10.1038/s41598-018-22681-3.

[159] T.-D. Leng, et al., Suppression of TRPM7 inhibits proliferation, migration, and invasion of malignant human glioma cells, CNS Neurosci Ther 21(3) (2015) 252-261, doi:10.1111/cns.12354.

[160] J.S. Taylor, et al., Free magnesium levels in normal human brain and brain tumors: 31P chemical-shift imaging measurements at 1.5 T, Proc Natl Acad Sci U S A 88(15) (1991) 6810-6814, doi:10.1073/pnas.88.15.6810.

[161] S. Chandra, et al., Quantitative imaging of magnesium distribution at single-cell resolution in brain tumors and infiltrating tumor cells with secondary ion mass spectrometry (SIMS), J Neurooncol 127(1) (2016) 33-41, doi:10.1007/s11060-015-2022-8.

[162] H. Jayatilaka, et al., Tumor cell density regulates matrix metalloproteinases for enhanced migration, Oncotarget 9(66) (2018) 32556-32569, doi:10.18632/oncotarget.25863.

[163] E. Henke, et al., Extracellular Matrix in the Tumor Microenvironment and Its Impact on Cancer Therapy, Front Mol Biosci 6 (2020) 160-160, doi:10.3389/fmolb.2019.00160.

[164] S.J. Forrester, et al., Reactive Oxygen Species in Metabolic and Inflammatory Signaling, Circ Res 122(6) (2018) 877-902, doi:10.1161/CIRCRESAHA.117.311401.

[165] P.D. Ray, et al., Reactive oxygen species (ROS) homeostasis and redox regulation in cellular signaling, Cell Signal 24(5) (2012) 981-990, doi:10.1016/j.cellsig.2012.01.008.

[166] M.E. Lull, M.L. Block, Microglial activation and chronic neurodegeneration, Neurotherapeutics 7(4) (2010) 354-365, doi:10.1016/j.nurt.2010.05.014.

[167] U.-K. Hanisch, H. Kettenmann, Microglia: active sensor and versatile effector cells in the normal and pathologic brain, Nature Neuroscience 10(11) (2007) 1387-1394, doi:10.1038/nn1997.

[168] J. Zhang, et al., Macrophage phagocytosis of biomedical Mg alloy degradation products prepared by electrochemical method, Materials Science and Engineering: C 75 (2017) 1178-1183, doi:10.1016/j.msec.2017.02.126.

[169] H. Kettenmann, et al., Physiology of Microglia, Physiological Reviews 91(2) (2011) 461-553, doi:10.1152/physrev.00011.2010.

[170] A.A. Khalili, M.R. Ahmad, A Review of Cell Adhesion Studies for Biomedical and Biological Applications, International journal of molecular sciences 16(8) (2015) 18149-18184, doi:10.3390/ijms160818149.

[171] S. Bell, et al., Universal Kinetics of the Onset of Cell Spreading on Substrates of Different Stiffness, Biophysical Journal 116(3) (2019) 551-559, doi:10.1016/j.bpj.2018.12.020.

[172] M.A. Partridge, E.E. Marcantonio, Initiation of attachment and generation of mature focal adhesions by integrin-containing filopodia in cell spreading, Mol Biol Cell 17(10) (2006) 4237-4248, doi:10.1091/mbc.e06-06-0496.

[173] K. Schlüter, et al., Corrosion performance and mechanical properties of sputter-deposited MgY and MgGd alloys, Corrosion Science 78 (2014) 43-54, doi:10.1016/j.corsci.2013.08.027.

[174] D. Haffner, et al., Micropatterned freestanding magnetron sputtered Mg-alloy scaffolds, BioNanoMaterials 16(1) (2015) 19, doi:10.1515/bnm-2015-0007.

[175] M. Liu, et al., The effect of crystallographic orientation on the active corrosion of pure magnesium, Scripta Materialia 58(5) (2008) 421-424, doi:10.1016/j.scriptamat.2007.10.027.

[176] B.J. Wang, et al., High corrosion resistance and weak corrosion anisotropy of an as-rolled Mg-3Al-1Zn (in wt.%) alloy with strong crystallographic texture, Scientific Reports 7(1) (2017) 16014, doi:10.1038/s41598-017-16351-z.

[177] A.D. Südholz, et al., Electrochemical Properties of Intermetallic Phases and Common Impurity Elements in Magnesium Alloys, Electrochemical and Solid-State Letters 14(2) (2011) C5, doi:10.1149/1.3523229.

[178] R.V.J. Chari, Targeted Cancer Therapy: Conferring Specificity to Cytotoxic Drugs, Accounts of Chemical Research 41(1) (2008) 98-107, doi:10.1021/ar700108g.

[179] P. Globig, et al., Optimizing an Osteosarcoma-Fibroblast Coculture Model to Study Antitumoral Activity of Magnesium-Based Biomaterials, International journal of molecular sciences 21(14) (2020) 5099, doi:10.3390/ijms21145099.

List of Figures

List of Tables

Appendix

1. Supplementary figures

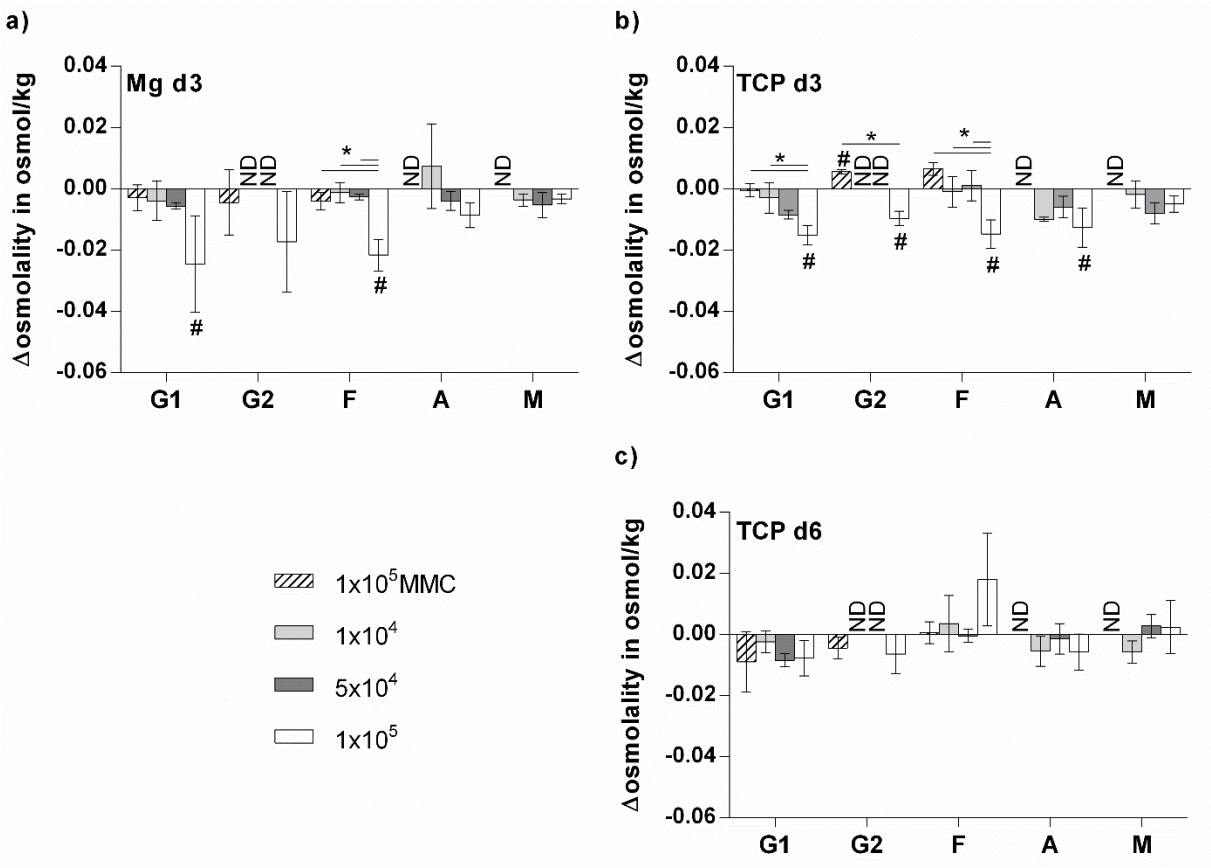

Figure s1 | **Δosmolality development.** Δosmolality for LN229 (G1), A172 (G2), astrocytes (A) and HMC3 (M) cells seeded on **a)** Mg or **b)-c)** on TCP after three or six days of immersion (n = 3). Statistical analysis was conducted employing one-way ANOVA. P-values of 0.05 or lower were considered statistically significant. Number signs indicate significant differences compared to control. ND = not determined.

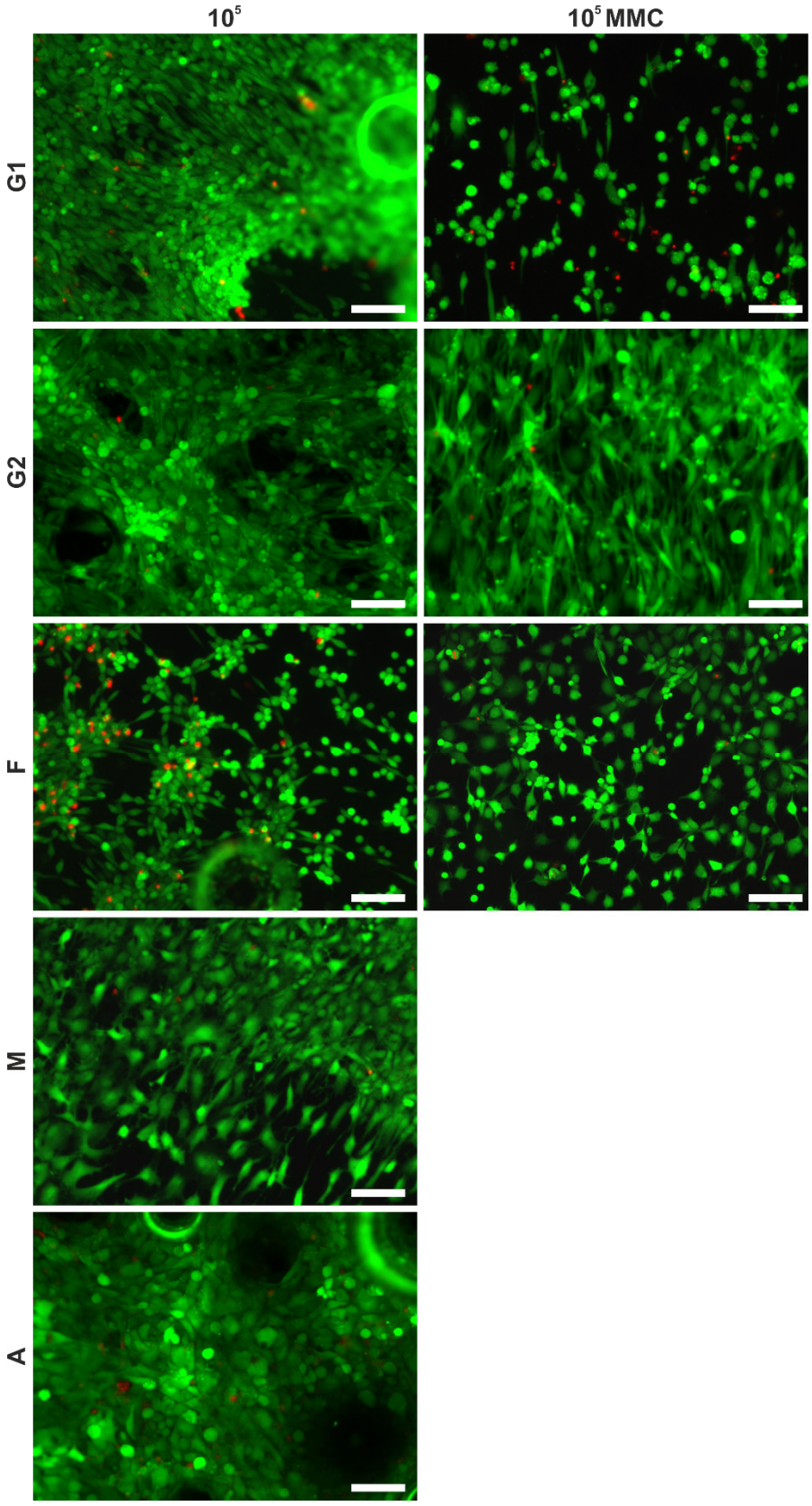

Figure s2 | Supplementary cell viability data on Mg discs. Calcein/ethidium homodimer-1 staining of viable (green) and dead (red) LN229 (G1), A172 (G2), L929 (F), astrocytes (A) and HMC3 (M) cells after six days of culture on Mg discs. Scale bar is 100 µm.

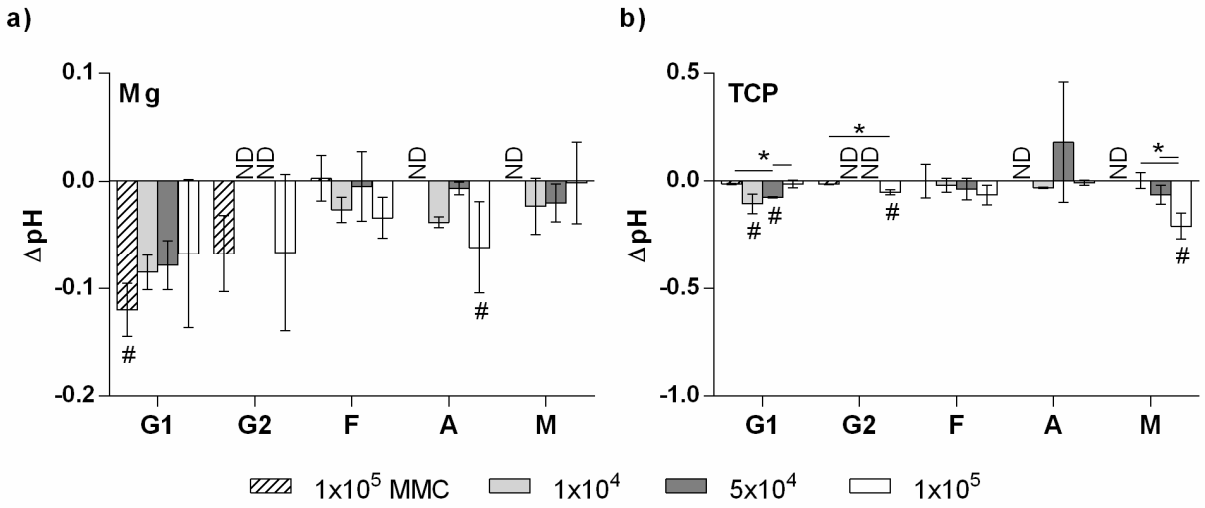

Figure s3 | **Cell-induced impact on bulk pH after three days.** ΔpH for LN229 (G1), A172 (G2), astrocytes (A) and HMC3 (M) cells seeded on **a)** Mg or **b)** on TCP after three days of immersion (n = 3). Statistical analysis was conducted employing one-way ANOVA. P-values of 0.05 or lower were considered statistically significant. Number signs indicate significant differences compared to control. ND = not determined.

2. Abbreviations

AD	Alzheimer’s disease
ADAM	A disintegrin and metalloproteinases
Ag	silver
AlN	aluminum nitride
ATP	adenosine triphosphate
ATR	attenuated total reflection
AuPd	gold palladium
BBB	blood-brain barrier
BCSFB	blood-cerebrospinal fluid barrier
BSA	bovine serum albumin
BSE	back scattered electrons
CA	carbonic anhydrases
Ca	calcium
CCM	cell culture media
Cl	chlorine
CNS	central nervous system
CO_2	carbon dioxide
CrA	chromic acid
CS	chondroitin sulfate
CSF	cerebrospinal fluid
CSPG	chondroitin sulfate proteoglycans
DAPI	4′,6-diamidino-2-phenylindole
DMEM	Dulbecco's Modified Eagle Medium
DNA	deoxyribonucleic acid
DR	degradation rate
ECF	extracellular fluid
ECM	extracellular matrix
EDTA	ethylenediaminetetraacetic acid
EDX	energy dispersive x-ray spectroscopy

ELISA	enzyme-linked immunosorbent assays
FBS	fetal bovine serum
FIB	focused ion beam
FITC	fluorescein isothiocyanate
FTIR	Fourier-transform infrared spectroscopy
GAG	glycosaminoglycans
galNAc	*N*-acetylgalactosamine
GBM	*glioblastoma multiforme*
glcNAc	*N*-acetylglucosamine
Ge	germanium
H_2	hydrogen gas
H_2O_2	hydrogen peroxide
HA	hyaluronic acid
HBSS	Hank's balanced salt solution
HCl	hydrochloric acid
HCO_3^{2-}	hydrogen carbonate ion
HO•	hydroxyl radical
HP	high purity
HRP	horse radish peroxidase
HS	heparan sulfate
HSPG	heparan sulfate proteoglycan
IR	infrared
IRE	internal reflection element
KOH	potassium hydroxide
LDH	lactate dehydrogenase
Li	lithium
MCT	monocarboxylate transporter
Mg	magnesium
$MgCO_3$	magnesium carbonate
$MgCl_2$	magnesium chloride

MgO	magnesium oxide
$Mg(OH)_2$	magnesium hydroxide
MMC	mitomycin C
MMP	metalloproteinases
Na	sodium
NaCl	sodium chloride
NAD^+/NADH	nicotinamide adenine dinucleotide
NaOH	sodium hydroxide
NMDA	*N*-methyl-D-aspartate
O_2	oxygen
O_2^-	superoxide
PBS	phosphate-buffered saline
PEO	plasma electrolytic oxidation
PG	proteoglycans
PO_4^{3-}	phosphate ion
PVD	physical vapor deposition
rH	relative humidity
RNA	ribonucleic acid
ROS	reactive oxygen species
SBA	soybean agglutinin
SD	standard deviation
SE	secondary electron
SEM	scanning electron microscopy
SFB	simulated body fluid
SiC	silicon carbide
SIET	scanning ion-selective electrode technique
TCA	tricarboxylic acid
TCP	tissue culture plastic
Tris	tris(hydroxymethyl)aminomethane
TRITC	tetramethylrhodamine

TRPM	transient receptor potential cation channel subfamily M
UV	ultraviolet
WGA	wheat germ agglutinin
XRD	x-ray diffraction
ZnSe	zinc selenide

List of publications and conference contributions

Publications:

1. **R. Unbehau**, B.J.C. Luthringer-Feyerabend, R. Willumeit-Römer, The impact of brain cell metabolism and extracellular matrix on magnesium degradation, Acta Biomaterialia (2020), doi:10.1016/j.actbio.2020.08.043.

   Teile dieser Veröffentlichung wurden in dieser Doktorarbeit modifiziert und verwendet. Dazu gehören teilweise Material/Methoden (Kapitel 3.3, 3.4, 3.5.1, 3.6.1, 3.6.2 und 3.7.2), Ergebnisse (Kapitel 4.2.1, 4.2.2, 4.3.1, 4.3.2, 4.3.3 und 4.3.5) und Ideen in der Diskussion (Kapitel 5.1, 5.2 und 5.3.1). Die Experimente in dieser Publikation wurden von Reneé Unbehau (R.U.) unter Absprache mit den zuständigen Betreuern konzipiert und durchgeführt. Ideen und Herangehensweisen wurden eigenständig von R.U. entwickelt. Die Erarbeitung der Diskussion entstand durch eigene Gedankengänge von R.U.. Das Manuskript wurde von R.U. eigenständig vorbereitet und geschrieben und nach einer Prüfung durch die Betreuer eingereicht.

2. **R. Unbehau***, L. Jessen*, B.J.C. Luthringer-Feyerabend, C. Zamponi, E. Quandt, R. Willumeit-Römer, Magnetron sputtered freestanding Mg-Ag films: promising materials for novel approaches to the treatment of neurological disorders?, in preparation. *shared first authorship

   Teile dieses zur Veröffentlichung vorbereiteten Manuskriptes wurden in dieser Doktorarbeit modifiziert und verwendet. Dazu gehören teilweise Material/Methoden (Kapitel 3.3, 3.4.1 und 3.4.2), Ergebnisse (Kapitel 4.4) und Ideen in der Diskussion (Kapitel 5.5 und 5.6). Die Experimente in dieser zur Veröffentlichung vorbereiteten Publikation wurden von Reneé Unbehau (R.U.) und Lea Jessen (L.J.) zu gleichen Anteilen (R.U.: Degradationsanalyse und in vitro Analysen und L.J.: Materialherstellung und Mikrostrukturanalyse) unter Absprache mit den zuständigen Betreuern konzipiert und durchgeführt. Ideen und Herangehensweisen wurden eigenständig zu gleichen Anteilen von R.U. und L.J. entwickelt. Die Erstellung der Diskussion entstand durch eigene Gedankengänge von R.U. und L.J.. Das Manuskript wurde von R.U. und L.J. eigenständig vorbereitet und geschrieben und unterliegt derzeit der Prüfung der Betreuer und Co-Autoren.

Other publications related to this thesis:

1. L.I. Fockaert, T. Würger, **R. Unbehau**, B. Boelen, R.H. Meißner, S.V. Lamaka, M.L. Zheludkevich, H.A. Terryn, J.M.C. Mol, ATR-FTIR in Kretschmann configuration integrated with electrochemical cell as in situ interfacial sensitive tool to study corrosion inhibitors for magnesium substrates, Electrochimica Acta 345 (2020) 136166, doi:10.1016/j.electacta.2020.136166.

Conference contributions:

1. **R. Unbehau**, D. Laipple, B.J.C. Luthringer-Feyerabend, R. Willumeit-Römer, Influence of glioblastoma cell lines on magnesium degradation, **Poster and talk**, 10th International Symposium on Biodegradable Metals, August 2018, Oxford, UK. – **Poster award**

2. **R. Unbehau,** D.Laipple, B:J.C. Luthringer-Feyerabend, R. Willumeit-Römer, Influence of glioblastoma multiforme (GBM) cell lines on magnesium (Mg) degradation, **Talk**, 4th InMAT, Juli 2017, Kiel, Germany.

3. V. Kokol, V. Vivod, **R. Unbehau**, T. Vuherer, B.J.C. Luthringer-Feyerabend, The effect of gelatine-based scaffold formulation and structure on *in vitro* mesenchymal stem cells viability and osteogenic differentiation, **Poster**, ESB 2019, September 2019, Dresden, Germany.

4. **R. Unbehau**, D. Laipple, B.J.C. Luthringer-Feyerabend, R. Willumeit-Römer, Influence of extracellular matrix compounds and cell metabolites on magnesium degradation, **Poster and talk**, 11th International Symposium on Biodegradable Metals, August 2019, Alicante, Spain. – **Poster award**

Danksagung

Abschließend möchte ich an dieser Stelle die Möglichkeit nutzen, mich herzlichst bei allen Personen zu bedanken, die mich während meiner Promotionszeit unterstützt haben.
Besonders hervorheben möchte ich dabei meine Doktormutter Prof. Dr. Regine Willumeit-Römer, die mich in den letzten vier Jahren nicht nur hervorragend wissenschaftlich betreut hat, sondern auch weit darüber hinaus meine persönliche Entwicklung nachhaltig gefördert hat.
Des Weiteren gilt mein Dank Prof. Dr. Christine Selhuber-Unkel für die Bereitschaft, das Zweitgutachten zu dieser Arbeit anzufertigen und PD Dr. Kirsten Hattermann-Koch für die wissenschaftliche Zweitbetreuung bis zu ihrer Elternzeit.
Ganz besonders möchte ich mich auch bei Dr. Bérengère Luthringer-Feyerabend für die intensive fachliche und moralische Unterstützung während meiner Promotionszeit bedanken.
Bei Dr. Daniel Laipple, Gert Wiese und Dr. Nico Scharnagl bedanke ich mich für die tatkräftige Unterstützung bei der Anfertigung der FIB-Schnitte und FTIR Analysen. Ein weiterer Dank gilt Prof. Dr. Mikhail Zheludkevich, Dr. Sviatlana Lamaka, Dr. Eduardo Trindade da Silva und Cheng Wang für die immense Hilfe bei den SIET Versuchen. Weiterhin möchte ich mich auch bei Prof. Dr. Arjan Mol und Laura-Lynn Foackaert dafür bedanken, dass sie meinen Gastwissenschaftsaufenthalt an der TU Delft ermöglicht und betreut haben.
Meinen Kollegen am Teilinstitut Metallische Biomaterialien des HZG danke ich für die uneingeschränkte Hilfsbereitschaft und die vielen wertvollen Tipps. Insbesondere gilt mein Dank dabei Monika Luczak, Anke Schuster, Nils Holländer, Dr. Katharina Philipp und Annette Havelberg für die praktische Unterstützung im Labor und die zahlreichen aufmunternden Gespräche.
Ein weiterer Dank geht an meine Kommilitonen/innen aus dem Graduiertenkolleg 2154-„Materials4Brain“ für den wissenschaftlichen Austausch und die Unterstützung trotz der Entfernung zwischen Geesthacht und Kiel. Ganz besonders möchte ich mich hier bei Lea Jessen bedanken, ohne deren unermüdlichen Einsatz beim Herstellen der Magnesiumfilme ein Teil der vorliegenden Arbeit nicht zustande gekommen wäre.
Eine große Stütze waren mir auch meine Familie und Freunde: mein Bruder Falk Unbehau, der für mich so vieles durch seine ruhige und ausgleichende Art relativiert hat, meine enge Freundin Maraike Ostermann, die zu jeder Tages- und Nachtzeit ein offenes Ohr für mich hatte und vor allem auch meine bessere Hälfte Philipp Globig, bei dem ich mich für sein Verständnis, seine unerschütterliche Geduld und seine Zuversicht bedanken möchte.
Mein größter Dank aber gilt meinen Eltern, Elke und Ronald Unbehau, für ihre bedingungslose und liebevolle Unterstützung mit der sie mir meinen bisherigen Lebensweg geebnet und ermöglicht haben.